

The Mitigation of Train-Induced Ground-Borne Vibrations

A Metamaterial based Solution

S.L.T. van Gaal

Delft University of Technology

The Mitigation of Train-Induced Ground-Borne Vibrations

A Metamaterial based Solution

by

S.L.T. van Gaal

to obtain the degree of Master of Science

at the Delft University of Technology,

to be defended publicly on Wednesday May 8, 2024 at 15:30 AM.

Student number: 4743342
Project duration: May 29, 2023 – May 8, 2024
Thesis committee: Dr. ir. K.N. (Karel) van Dalen, TU Delft, Chair
Dr. ir. A. (Apostolos) Tsouvalas, TU Delft
Dr. ir. A.B. (Andrei) Fărăgău, TU Delft, supervisor
Ir. E. (Eliam) Vlijm, Cohere Consultants

An electronic version of this thesis is available at <http://repository.tudelft.nl/>.

Preface

This thesis is the final requirement for my Master's degree in Structural Engineering at the Faculty of Civil Engineering. During my studies, I developed a strong interest in structural dynamics, which led me to choose a thesis topic in this area. My research focuses on reducing train-induced ground-borne vibrations using metamaterials, an innovative approach to a growing problem. This topic is increasingly important as railway transportation expands, bringing challenges like vibrations and noise. Solutions to these problems can greatly benefit society.

I want to thank everyone who has helped me during my thesis. Special thanks to Apostolos Tsouvalas and Karel van Dalen for their valuable insights; Eliam Vlijm and Cohere Consultants for giving me the opportunity to conduct my research at their company and guiding me, which helped me develop my technical skills and understanding of the topic. I also want to thank my supervisor, Andrei Fărăgău, for our many discussions and providing me with direction whenever I felt stuck. Finally, I am grateful to my friends and family for their continuous support.

*S.L.T. van Gaal
Delft, May 2024*

Summary

The objective of this thesis is to study the underlying physics of metamaterials and engineer an effective mitigation strategy for train-induced vibrations, which are increasingly problematic with the expected growth in train transportation. Trains, known for their sustainability due to low carbon emissions, are anticipated to see a doubling in both passenger and freight activity by 2050. The vibrations caused by trains, particularly those from freight trains characterized by low frequencies and high amplitudes, pose challenges to human comfort and the structural integrity of nearby buildings. Traditional mitigation methods, like trenches, often fail to perform adequately against low-frequency vibrations and at small incidence angles. To address these challenges, this thesis proposes a solution based on the principles of metamaterials. Metamaterials are engineered substructures that can be integrated along the propagation path to modify wave propagation properties in ways that are conventionally not possible. By manipulating wave propagation in elastic media, metamaterials create frequency bands where certain waves cannot propagate, making them an effective solution for shielding areas from vibrations.

This study starts by reducing the complexity of the problem to one-dimensional wave propagation problem, focusing on the Euler-Bernoulli beam on a visco-elastic foundation with infinite periodic resonators. This approach contrasts with the more intricate three-dimensional wave propagation models, such as those involving a half-space. This simplification allows for analytical solutions that provide insights into the mathematics governing wave propagation and band gap formation. A Floquet analysis of this infinite periodic system reveals that bandgaps can arise from the local resonance of the metamaterials, centered around the resonators' natural frequency, and from the periodicity of the resonators, where the central frequency of the band gap correlates with the spacing between resonators and the wavelength of the targeted wave. Advancing from the infinite to a finite periodic system introduces complexities that preclude the use of Floquet analysis, necessitating a new approach to characterize the system. This stage aims to understand the behavior of a finite system and link it to the infinite model, providing insights valuable for designing metamaterial-based mitigation measures in early design stages. The findings confirm that the properties of a finite metamaterial region can effectively be inferred from its infinite counterpart, with excellent agreement observed between the analytic and numerical models. This alignment underscores the validity of leveraging infinite system analyses to accurately predict the behavior of finite systems.

Metamaterials often consist of a periodic arrangement of structures known as a unit cell. The metawedge, a promising configuration of metamaterials, features unit cells each with a slightly different natural frequency, arranged to create a gradient of frequencies—hence the term "wedge." This frequency variation allows the metawedge to target a broad spectrum of frequencies. Depending on its configuration, a metawedge can either trap waves inside the wedge through "elastic rainbow trapping" or transform incoming Rayleigh waves into body waves that penetrate deep into the soil, a mechanism known as "wave-mode conversion." However, the one-dimensional model cannot capture the latter phenomena, so the analysis extends to a three-dimensional problem involving a homogeneous elastic half-space with single-degree-of-freedom resonators representing the metamaterials. Analyzed using FEMIX—a plane-strain coupled boundary element and finite element model—this approach allows the behavior of various metawedge configurations to be examined using methodologies similar to those employed in earlier chapters. The goal is to correlate its behavior with the analytical model and to understand the underlying physics. This study reveals that wave-mode conversion results from the inverse metawedge's ability to accelerate waves, while rainbow trapping is a consequence of wave deceleration in the classic configuration. Additionally, this research explores how to optimize a metawedge to make it an effective low-frequency vibration mitigation measure. This investigation has demonstrated that it is feasible to design a metamaterial-based mitigation measure, utilizing a practical design of only 300 kg per resonator, to address frequencies in the 10 to 15 Hz range, with the potential to adjust this range to meet specific requirements.

Contents

Preface	i
Summary	ii
1 Introduction	1
1.1 Problem statement	1
1.1.1 Railway induced vibrations	1
1.1.2 Traditional mitigation measures	2
1.1.3 Metamaterials	3
1.2 Scope and objectives	5
1.3 Overview	7
2 Analytic study of metamaterials on an Euler-Bernoulli beam	8
2.1 Euler-Bernoulli beam on visco-elastic foundation	8
2.1.1 Dispersion relation	9
2.2 Metamaterial model description	10
2.3 Floquet analysis of model with fixed metamaterials	13
2.3.1 Parametric study	16
2.4 Floquet analysis of model with free metamaterials	18
2.4.1 Parametric study	21
2.5 Summary	23
3 Numerical study of metamaterials on an Euler-Bernoulli beam	24
3.1 Adopted numerical model	24
3.2 Verification of the numerical model	25
3.2.1 Steady-State solution to a harmonic point load	26
3.2.2 Transmission and reflection at one fixed metamaterial	28
3.2.3 Transmission and reflection at one free metamaterial	29
3.3 Wave characteristics of the finite periodic system	31
3.3.1 System with fixed metamaterials	32
3.3.2 System with free metamaterials	33
3.4 Behaviour of the inverse and classic metawedge	35
3.5 Summary	40
4 Numerical study of metamaterials on a homogeneous half-space	42
4.1 Adopted numerical model	42
4.1.1 Verification of numerical model	45
4.2 Identification of band gaps	46
4.3 Wave characteristics analysis	56
4.4 Parametric study	61
4.5 Influence of incidence angle	63
4.6 Summary	67
5 Conclusions and recommendations	68
5.1 Conclusion	68
5.2 Recommendations for further research	69
References	71

1

Introduction

As urban populations grow, the demand for habitable space intensifies, prompting a significant expansion of infrastructure. This development is closely linked to the expanding role of train transportation, which faces its own challenges, notably the increasing intensity of vibrations from heavier, more frequent trains. These vibrations not only disrupt the comfort and well-being [25] of residents but also pose a threat to the structural integrity of nearby buildings [29]. Vibrations generated by the interaction between the train, track and soil can propagate to large distances from the track [23]. Especially those generated by freight trains as their vibration signature consists out of high amplitude and low frequencies. The receiver (e.g. buildings) will react to these vibrations and will in itself start to vibrate which can be perceived as unpleasant or in extreme cases cause harm to humans and animals. Particularly when combined with noise pollution these vibrations become more noticeable [11].

Currently, rail transportation stands out as the foremost sustainable mode of mass transit, serving both passengers and freight. Its inherent design minimizes the production of greenhouse gas emissions (specifically, low CO₂ emissions) and air pollutants, all while exhibiting remarkable efficiency in land and energy utilization. The European Union's objective is to achieve climate neutrality by 2050 [19]. Realizing this goal requires the doubling of high-speed rail infrastructure by 2030 and a doubling of rail freight capacity by 2050. Because of the growing train capacity and the undesirable vibrations that come with it the need for a vibration reduction measure is desirable. Ground-borne vibrations can be mitigated either at the source, transmission path or receiver. Since the receiver (e.g. buildings) and the source (train track) are usually pre-existing structures the propagation path seems the most logical place to design mitigation measures. However in recent years new developments have taken place which allows for a design of mitigation measures at the pre-existing train track as well, even without the disruption of rail traffic.

1.1. Problem statement

1.1.1. Railway induced vibrations

Both airborne and ground-borne vibrations are caused by the interaction between the train, track and soil. The primary source of railway noise stems from rolling noise, which is generated by vibrations at the wheel-rail interface [27]. Irregularities on the surfaces of both wheels and rails lead to vertical vibrations within the wheel and rail systems. Ground-borne vibrations are induced by various factors related to the operation of trains and the interaction between trains and the track. The most obvious source of railway vibrations is the movement of trains along the tracks. When a train is in motion, it generates dynamic forces that are transmitted to the track and soil. Which will then propagate to the surrounding structures.

The interaction between the train wheels and the rails is a significant source of vibrations. As the train wheels roll along the tracks, they can create rolling noise and vibrations due to irregularities in the wheel and rail profiles. Furthermore the condition of the track itself can contribute to vibrations. Irregularities such as track geometry defects or transition zones [15] can result in greater dynamic forces on the

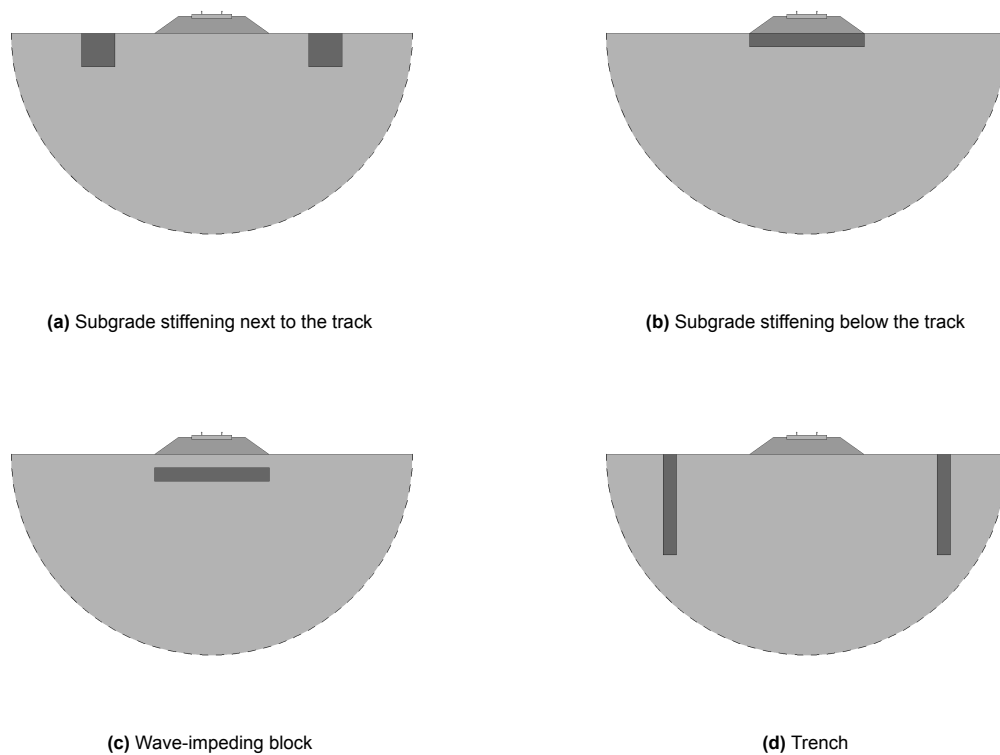


Figure 1.1: Traditional mitigation measures

tracks, leading to more pronounced vibrations. The speed and weight of a train play a role in the intensity of vibrations. Especially freight trains are responsible for significant vibrations. As their heavy load lead to high amplitude and low frequency vibrations. This induces waves that propagate along the surface of the ground. Ground-borne vibrations of this nature are particularly associated with soft soil conditions, where they can travel significant distances, up to approximately 100 meters from the track. These vibrations often feature substantial components at extremely low frequencies, typically below 10 Hz, resulting in the oscillation of floors of nearby buildings [27].

1.1.2. Traditional mitigation measures

Mitigation of ground-borne vibrations can be applied at the source, propagation path or at the receiver. To implement mitigation measures at the source, there are primarily two domains of intervention. Specifically, these interventions entail alterations in the wheel-rail interaction or modifications to the structural properties of the subsoil beneath the railway track. From which the latter is known as subgrade stiffening and is the most effective for low-frequency vibrations [26].

Subgrade stiffening can either be applied next to the train track or below the track, as depicted in Figure s1.1a and 1.1b respectively. Due to the increase of effective stiffness this measure is able to mitigate vibrations. Therefore it is more efficient on softer soils [13], [26]. In [2] and [18] it is found that subgrade stiffening next to the track is more effective then below the track. However, not all studies are in agreement about subgrade stiffening and discrepancy in results might be due to the focus on different frequency spectra. There are mainly two options for subgrade stiffening under the track. It can either be constructed directly at the surface as depicted in Figure 1.1b or at a certain depth as can be seen in Figure 1.1c. The latter option is referred to as a wave impeding block. However as stated in [26] there are no advantages of using a wave impeding block over subgrade stiffening directly at the surface. Subgrade stiffening can however have some challenges as the soil beneath the track cannot easily be modified without removing the existing train track.

A similar challenge arises for the receiver. In most cases the receiver are buildings that are in close proximity to the train track. As these buildings are pre-existing it can be challenging and not cost effective to change the dynamic behaviour of them. Therefore designing mitigation measures at the propagation path seems to be most logical choice. Various mitigation measures can be employed along the transmission path to address ground-borne vibrations effectively. One such approach involves trenches, depicted in Figure 1.1d, where there is a choice between open or filled configurations. Open trenches begin to exhibit efficacy when their depths surpass half the Rayleigh wavelength [17], with their effectiveness largely independent of width. However, practical limitations arise in their construction due to stability concerns and the potential presence of groundwater, restricting their application to relatively shallow depths. To enhance stability, alternative configurations such as sloped or walled trenches can be considered, with minimal impact on their performance.

Alternatively, soft wave barriers represent another viable mitigation strategy, and they can be constructed using materials like rubber chips, gas-filled cushions, or polystyrene panels. The depth of these barriers plays a crucial role in determining their frequency range of effectiveness, with reduced stiffness of the in-fill material and increased barrier width contributing to greater vibration reduction. Additionally stiff wall barriers such as concrete walls, sheet pile walls, and jet grouting, constitute yet another effective mitigation option. Their performance hinges on both barrier impedance and stiffness. For substantial depths, impedance disparities lead to the reflection of incoming Rayleigh waves, while the bending stiffness of the wall prevents wave propagation when wavelengths are considerably smaller than the bending wavelength of the barrier.

A recent study [1] on the effectiveness of the stiff in-filled trench found that the most important parameter is the stiffness difference between the soil and the barrier. It was found that this measure was effective in mitigation the transmitted waves. However it was found that for a large range of incident angles with respect to the outward normal of the trench this measure doesn't influence the propagation of waves at all.

1.1.3. Metamaterials

In the last decade seismic metamaterials [5] have gained a lot of interest in the field of elastodynamics. Metamaterials are able to add non-dispersive properties to a medium, such that certain frequencies are no longer able to propagate when encountering a metamaterial. They often consist out of periodic structures usually called unit cells that repeat periodically in a subwavelength scale [5]. Subsequently, these metamaterials possess the capacity to obstruct, absorb, amplify, alter the trajectory, and reflect waves in manners that surpass the capabilities of conventional materials. [5]

A geophysical experiment [9] reveals that a Rayleigh wave, propagating through soft sedimentary soil at frequencies below 150 Hz, undergoes significant attenuation when encountering a forest. The trees essentially function as sub-wavelength resonators, known as locally resonant elastic metamaterial. This concept can be expanded to seismic metamaterials which can be designed in such a way that band gaps are created that do not allow the propagation of waves for the desired frequencies. In recent years, numerous metamaterial designs have emerged, sharing a common principle: the creation of band gaps centered around their natural frequencies [6], [24]. While these designs exhibit similarities in this fundamental aspect, variations can be found primarily in the origin of their natural frequencies. For instance, metamaterials can take on diverse forms such as barriers, rods, or single-degree-of-freedom (SDOF) oscillators. Some of them are shown in Figure 1.2.

Three primary types of metamaterials can be distinguished [5]. The first category are the Seismic Soil-Metamaterials (SSM) they consist out of structured soils that include fully buried cylindrical voids or rigid inclusions. These inclusions can create band gaps by using the Bragg's effect which is based on the principles of diffraction, where waves encounter an ordered, periodic arrangements of the same order of the surface wavelengths within a lattice. This model is not suited for mitigating surface Rayleigh waves at the geophysical scale, where the characteristic wavelengths span from just a few meters to hundreds of meters [9].

The second category are the Buried Mass-Resonators (BMR). A BMR is a device composed of a mass, a spring, and a damper embedded within the soil. Each resonator can be tuned to the desired natural frequency such that band gaps can be created for the targeted frequencies of interest [24]. Due to

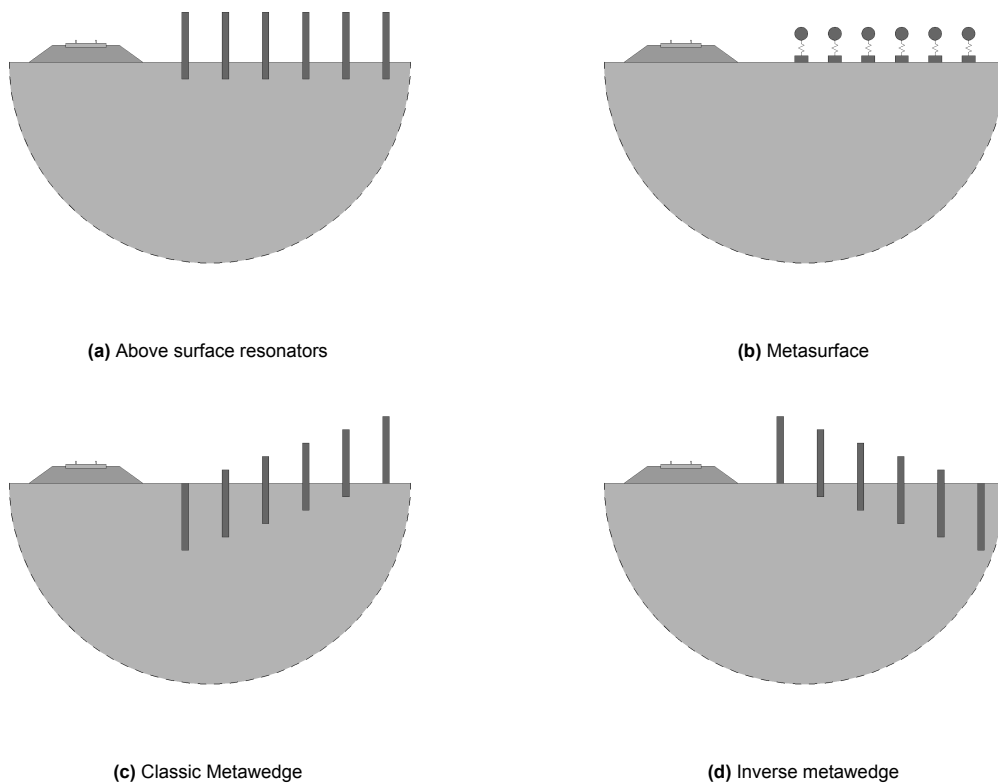


Figure 1.2: Metamaterial configurations

the counter clockwise elliptical motion of the Rayleigh waves both the horizontal and vertical modes of vibration are excited. This creates two surface wave band gaps. The one created by the horizontal natural frequency seems to create a very narrow band gap that is not usable [24]. The band gap created by the vertical natural frequency is usable and they are able to create a band gap for very low frequencies, in the range of train induced vibrations.

The final category are the Above-Surface Resonators (ASR), for instance, these could include the trees within a forest as examined in [9]. In this case the trees act as resonators each with their own natural frequency, this can be modelled as rods on top of an elastic halfspace [10], which can be seen in Figure 1.2a. In this paper the author proposes an analytical model to obtain the dispersion relation. The dispersion curves reveal the upper and lower limits of the band gaps created by the local resonance of the resonators [10].

In a recent publication, a novel ASR design was introduced: the resonant metawedge [8], comprised of spatially graded vertical sub wavelength resonators positioned on an elastic substrate. This paper proposes two designs, the classic metawedge and the inverted metawedge, which can be seen in Figure 1.2c and 1.2d respectively. Essentially these two designs are the same as they consist out of above surface resonators with a linearly varying embedded depth. In the classic metawedge the wavefront approaches the metawedge on the side of the fully embedded resonator while for the inverted metawedge the wavefront approaches it at the side where the resonator is fully exposed above the surface. Their response however is different. In the case of the classic metawedge when the wavefront reaches the metawedge it is expected to slow down until reaching the resonator whose fundamental longitudinal mode matches the input frequency of the signal. This position is dubbed the turning point because the wave trajectory is forced to diverge. At this stage the propagation is characterized by a band gap which, like a rigid barrier, reflects the energy backward. This phenomenon is called the "rainbow effect" [8].

In the case of the inverted metawedge the Rayleigh wave is sped up inside the metawedge until a

point where it reaches the shear wave speed. At this point it can no longer propagate as a surface wave and is converted to a shear wave which propagates down into the soil. This phenomenon is called mode-conversion. This effect is very desirable as the energy of the Rayleigh wave is no longer reflected backwards to the track as was the case with the classic metawedge. This mode-conversion is observed in many papers such as [1], [7], [8] and more. This phenomenon is reproduced using numerical models and physical experiments.

Other solutions for mitigating vibrations exploiting the principles of metamaterials that can be considered are SDOF oscillators placed on top of the soil [6], [20]. From a theoretical standpoint this might be the easiest solution as the dynamics of SDOF systems are straightforward and well understood. Such solutions are usually called metasurfaces and are depicted in Figure 1.2b. When the natural frequencies of all resonators are identical, the configuration is referred to as a uniform metasurface, if the natural frequencies of the resonators vary per row, the configuration is known as a graded metasurface [6]. With both the uniform and graded metasurface they were able to observe the wave-mode conversion yet the underlying physics remain unclear. In [20] a design optimisation strategy was proposed. In the paper the mean power flow of the metasurface was used as objective function to optimize. For a higher mean power flow better vibration attenuation was observed and therefore also stronger conversion of Rayleigh to shear waves. A positive correlation was found between the mass of the resonator and the mean power flow.

Some physical experiments [7], [9] have been conducted. In [7] this was done in a scaled setting, by conducting an experiment in the ultrasonic range. The experiment consists of an aluminium block of rectangular cross-section with an array of resonators on top of the surface. The block is excited by a Ricker pulse and motion of the block is captured by cameras directed at the top and bottom of the block. In the case of the classical wedge they were able to observe the slowing down of the wave inside the metawedge, their wavelength became as short as the spacing between the resonators. At the same time the amplitude was strongly amplified. In the case of the inverted metawedge the wave was not reflected but redirected to the bottom of the block where the motion was picked up by the bottom scan.

1.2. Scope and objectives

This thesis addresses the challenge of engineering an effective mitigation measure for both low frequency vibrations and small incident angles waves induced by trains. The main focus of this thesis lies in the understanding of the mitigation measures and the engineering of a metamaterial solution that not only is effective but also realistic and economically feasible. Among the designs presented in section 1.1.3, the metawedge stands out as particularly promising due to the varying outcomes it offers based on its configuration. The metawedge represents a unique case of above surface resonators, wherein the wedge configuration can be classical, inverse, or uniform. However, referring to it as a "wedge" in the uniform configuration might not be entirely accurate. The fundamental design concept involves the creation of a periodic structure where each unit cell's resonator possesses a distinct natural frequency. The manner in which these resonances vary along the length of the metawedge determines if its classical, inverse or uniform and determines its performance. Understanding the metawedge's behavior and underlying physics is essential, as it forms the basis for designing an efficient mitigation strategy. To guide the thesis towards its goal this objective is divided into two main objectives, as follows.

1. Understanding the underlying physics that drive the mitigation mechanisms of the metawedge

The first objective is to understand the underlying mitigation measures that enables the metawedge to effectively dampen vibrations. Research into metamaterials has identified two primary mechanisms for vibration mitigation: wave-mode conversion and rainbow trapping [8]. Obtaining a deeper understanding of the underlying physics is crucial for the engineering of an effective design. To address this, the complexity of the problem is reduced by examining a simplified scenario. The scenario under consideration involves a Rayleigh wave traveling over the surface of a homogeneous half-space and propagating towards the metawedge. The metawedge is positioned on the surface of the elastic half-space, as depicted in Figure 1.3. This arrangement allows for the division of the metamaterial into unit cells, each defined as a column of soil with a single degree of freedom resonator placed on top of the soil. The interaction between the soil and structure alters the medium's dispersion curve. This design has a couple of advantages, the natural frequency of the resonator can easily be changed while keep-

ing most of the parameters constant. This will allow for maximum flexibility during the design phase where all parameters can be easily monitored.

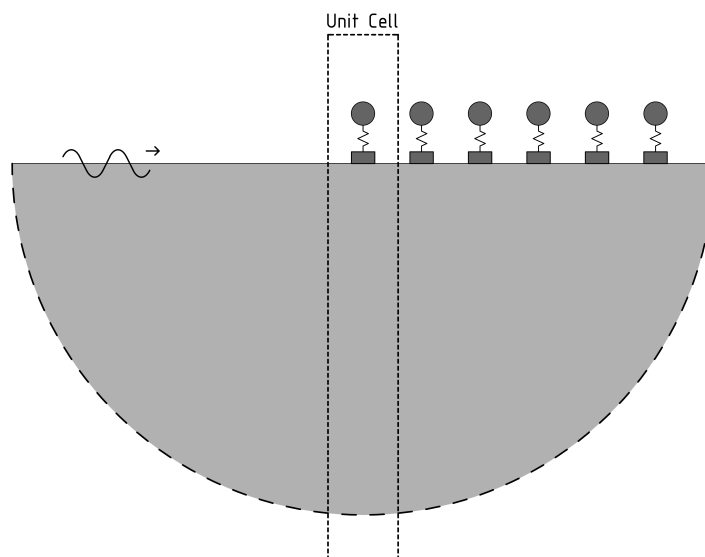


Figure 1.3: Simplified metawedge model

As described in [8] the metawedge forces a wave to speed up or slow down depending on the configuration of the metawedge. To understand this behaviour it is important to look at the dispersive properties of the system. Due to the soil-structure interaction the local dispersive properties of the unit cell will differ from the surrounding soil. Therefore when an incident wave encounters the metawedge it either has to change in frequency or wavenumber and therefore its velocity will change as well. Depending on how the metawedge influences the velocity of the wave two different behaviours are expected. Understanding this phenomenon is crucial for engineering an effective metawedge.

For this investigation the problem is reduced to a beam on a visco-elastic foundation. Single degree of freedom resonators are placed periodically along the beam to simulate the metamaterials. As a wave travels across the beam and encounters a resonator, the dispersive properties of the reflected and transmitted waves can be analyzed. Observing a change in frequency or wavenumber may provide evidence to support the hypothesis. However, this model is limited in capturing wave-mode conversion, as it is restricted to one-dimensional waves that can only propagate along the beam itself. The model can be further adapted to vary the mass or spring stiffness of each resonator. This modification permits a gradual adjustment of the resonators' natural frequencies, enabling the representation of either the classical or inverted metawedge configuration.

After obtaining the results the model can be extended to one that is closer to reality. To do this a model in FEMIX [21] will be created. FEMIX is a 2.5D coupled boundary and finite element model, which is a 3D model where in one direction the geometry is considered homogeneous. This will allow for faster calculation times while still having the benefit of obtaining the results in three directions.

2. Engineer a metamaterial based mitigation measure that exhibits low-frequency and wide band gaps

The second objective addresses the challenge of designing a mitigation strategy for train-induced ground-borne vibrations that perform well for low frequency vibrations and at small incident angles. The exploration of innovative design strategies aims to develop a metamaterial design capable of attenuating a broad spectrum of train-induced ground-borne vibrations. By examining the underlying physics of the metawedge, a better understanding of metamaterials is achieved. This knowledge facilitates the design of a metamaterial optimized to leverage these mechanisms effectively, particularly for train-induced vibrations. Previous metamaterial designs have faced challenges related to size and economic

feasibility. Thus, in the design process of a metamaterial structure, practicality and cost-effectiveness are prioritized. Following the development of a design, its performance evaluation is crucial, achieved through comparison with scenarios where mitigation measures are absent.

1.3. Overview

This thesis is organized to begin with the analysis of simpler problems that allow for analytical approaches. Gradually, the complexity of the issues addressed will increase, leading to the development of a functional design. Along this journey, valuable insights into the mechanisms driving the metawedge's functionality will be uncovered. This structured progression ensures a comprehensive understanding of both foundational principles and advanced applications within the realm of metamaterials, facilitating the transition from theoretical analysis to practical design solutions.

Chapter 2

Chapter 2 begins by addressing the most fundamental problem: the analysis of the infinite periodic system. This configuration includes an Euler-Bernoulli beam placed on a visco-elastic foundation, with resonators that repeat in a periodic fashion indefinitely. Two scenarios are analysed: one where the resonators degrees of freedom are linked to the beam, and another where the resonators possess their own degrees of freedom, a schematic illustration is provided in chapter 2.2. While an infinite periodic system is an abstraction, far removed from practical reality, its analysis yields significant insights into the dynamics of metamaterials. The periodic nature of the system facilitates the application of Floquet analysis, offering a deeper understanding of the wave propagation characteristics of the beam. This theoretical exploration is crucial for understanding the principles that govern the behavior of periodic structures even if they do not repeat indefinitely.

Chapter 3

The primary limitation identified in Chapter 2 concerns the application of an infinite periodic system. In this subsequent chapter, the focus will shift towards the examination of a finite periodic system. The objective is to ascertain whether a finite periodic system retains similar properties to its infinite counterpart. As this problem is no longer purely periodic a Floquet analysis is no longer possible, therefore a different strategy is needed. This problem will be analysed using a numerical model. The propagation of waves within the computational domain is modelled using the finite element method, with non-reflective boundaries incorporated to emulate the effect of an infinitely extending beam. This system will be solved through the Newmark-Beta method. The computational domain will be segmented, creating distinct areas where metamaterials are either present or absent. Utilizing a wavenumber transform across these areas aims to extract the wavenumbers of the excited waves, thereby also shed light on the dispersive characteristics of the system. These findings will subsequently be compared with the outcomes presented in chapter 2.

Chapter 4

Transitioning from the examination of one-dimensional (1D) wave propagation problems, this chapter introduces a two-dimensional (2D) model. This model is composed of a 2D half-space onto which single degree of freedom resonators are mounted atop the substrate. Functionally, this setup approximates a three-dimensional (3D) model subjected to a line load, leading to the anticipation of wave propagation directed exclusively towards the mitigation measure at a zero incidence angle. Consequently, this model aligns more closely with practical applications intended for the assessment of mitigation strategies. Using insights acquired from preceding chapters, a mitigation approach employing single degree of freedom resonators will be devised. Subsequently, the analysis progresses to a full three-dimensional wave propagation model, which more accurately reflects the various incidence angles generated by trains, enabling the evaluation of the metawedge's performance against various incidence angles— a scenario where traditional measures like trenches typically show limitations. The objectives of this chapter include the development of a mitigation measure and the understanding of its underlying mechanisms.

2

Analytic study of metamaterials on an Euler-Bernoulli beam

To engineer an efficient mitigation measure it is of most importance to understand its underlying mechanisms. In recent times a new, at least for ground-borne vibrations, and relatively unexplored mitigation measure has gained a lot of interest. This mitigation measure is based on the principle of metamaterials, which are inclusions to a structure or soil that will change its properties in such a way that it conventionally would not have. In recent papers it is shown that metamaterials can be an effective solution [5], [6], [8], [20]. However a practical solution for low frequency waves has not been presented. To investigate this the problem will be reduced to the most fundamental case. Metamaterials can induce bandgaps, these are frequency bands in which propagation is not possible. Such band gaps can be created using two phenomena: Bragg scattering and local resonance. Bragg scattering occurs when the wavelength of the excited wave is in the same order of as the periodicity. Local resonance on the other hand is as the name suggest based upon the natural frequency of the metamaterials, and they work in a similar matter as tuned mass dampers. To investigate these mechanisms in its purest form a one-dimensional wave propagation problem is solved. The model consists of an infinitely long Euler-Bernoulli beam on visco-elastic foundation which mimics the behaviour of the soil, with periodic mass-spring-dashpots attached to it. These mass-spring-dashpot systems represent the metamaterials, as they can be placed in a periodic manner and its natural frequency is easily tuned. The aim of this chapter is to derive the propagation characteristics of the model and find out which parameters influence it.

2.1. Euler-Bernoulli beam on visco-elastic foundation

The study begins by simplifying the complex phenomenon of three-dimensional wave propagation to a one-dimensional model using the Euler-Bernoulli beam theory. The aim here is to keep the model as straightforward as possible to better understand metamaterials without the extra complexity that a three-dimensional model would bring. It offers a simpler approach that is more suitable for the kind of detailed investigation into metamaterials that this study intends to carry out. The selection of a beam model, over other one-dimensional models like taut strings, is particularly well-suited to this study's goals. The study aims to mimic the behavior of Rayleigh waves, which are surface waves that travel through the soil. The beam model is chosen because it allows for an examination of transverse displacement with respect to the direction of wave propagation, which is a major component of Rayleigh waves. Introducing a visco-elastic foundation to the model brings in an element of damping, capturing the soil's behavior more accurately than a purely elastic model could. This addition makes the model a better reflection of real soil conditions, despite making it slightly more complex. However, the Euler-Bernoulli beam theory still allows for relatively simple mathematical expressions, enabling the derivation of analytical solutions that are crucial for understanding the basic effects of metamaterials on wave propagation.

While more complex models like the Timoshenko beam theory could potentially offer more accurate results, they also introduce more complexity, which isn't necessary for the foundational understanding

of metamaterials. The parameters of the visco-elastic model can be tied back to real soil measurements, making it a practical tool for applying theoretical findings to real-world situations. Nevertheless, it is important to acknowledge the limitations of the Euler-Bernoulli beam theory. It assumes that the beam's cross-sections remain plane and perpendicular to the beam's axis after deformation, ignoring the effects of shear deformation. This approximation works well for small deformations and frequencies up to 500 Hz [27], but it might not provide accurate results for larger deformations or higher frequencies, as noted in research focused on railway vibration control. This simplification means the theory may not always produce precise results, especially for conditions beyond its ideal scope of application.

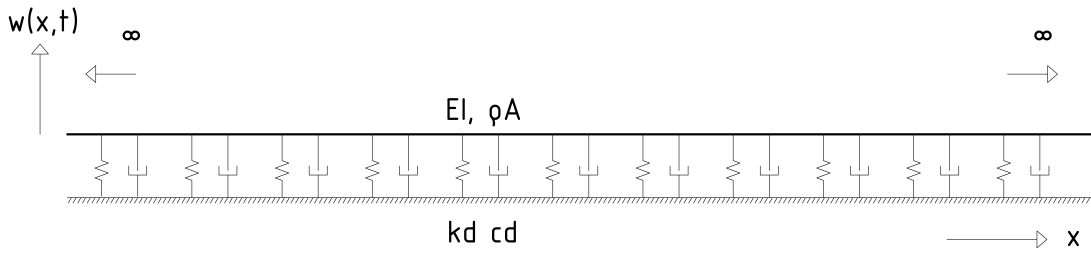


Figure 2.1: Euler-Bernoulli beam on visco-elastic foundation

2.1.1. Dispersion relation

As a first step the homogeneous equation of motion for the Euler-Bernoulli beam resting on a visco-elastic foundation is considered, as delineated in Equation 2.1. This examination is pivotal since our interest lies in the wave propagation characteristics inherent to the beam system. To initiate this analysis, the complex representation of a harmonic wave is introduced in Equation 2.2. Integrating this representation into the homogeneous equation of motion enables the derivation of the system's dispersion relation. The dispersion curve, thus obtained, serves as a graphical tool that maps the relationship between the frequency and wavenumber of waves that can propagate over the beam. This curve is indispensable for unraveling the intricate dependency of phase and group velocities on frequency—a phenomenon known as dispersion. Understanding dispersion is crucial for grasping the fundamental behaviors of wave propagation, providing insights that are essential for the subsequent investigation of metamaterials and their impact on wave dynamics within the system.

$$\rho A \frac{\partial^2 w(x,t)}{\partial t^2} + EI \frac{\partial^4 w(x,t)}{\partial x^4} + c_d \frac{\partial w(x,t)}{\partial t} + k_d w(x,t) = 0 \quad (2.1)$$

$$w(x,t) = \tilde{A} \exp(i(\omega t - \gamma x)) \quad (2.2)$$

In equation 2.1 ρ is the density of the beam per meter, A the area of the cross-section, EI the bending stiffness of the beam, c_d the distributed damping and k_d the distributed spring stiffness. The combination of these parameters will mimic the reaction of the soil. The metamaterials will later be introduced by adding resonators in a periodic manner. After substitution, the dispersion relationship of the beam is derived, expressing the wavenumber in terms of frequency as:

$$\gamma^4 = \frac{\rho A}{EI} \left(\omega^2 - i\omega \frac{c_d}{\rho A} - \omega_0^2 \right) \quad (2.3)$$

The dispersion curve offers insightful details about the dynamics of the system under study. It reveals that for any given frequency, four distinct wavenumbers are excited, corresponding to the four roots of Equation 2.3. This indicates the presence of four potential wave modes within the system: two waves with the capacity to propagate towards the left and two to propagate towards the right. Of each pair, one wave is identified as evanescent, characterized by its non-propagating nature, while the other assumes the form of a sinusoidal wave, capable of propagating energy. The nature of these waves is distinguished by examining the complex-valued wavenumbers. The sign of both the real and imaginary components of these wavenumbers unveils critical attributes of each wave, including its direction of propagation and behavior over distance. Specifically, the direction is inferred from the sign of the imaginary part: a positive sign indicates leftward propagation, while a negative sign suggests rightward movement. The relationship between the real and imaginary parts further classifies the wave as either exponentially growing or decaying, or as an exponentially modulated sinusoidal wave, depending on whether these signs are identical or opposite, respectively.

The dispersion curve can be conceptually divided based on the cut-off frequency, yielding two distinct regions: above and below this threshold. Frequencies below the cut-off are characterized by significant wave attenuation, creating what is effectively a band gap, a range where wave propagation is severely restricted. Conversely, excitation frequencies above this threshold result in wavenumbers with minor imaginary components, predominately leading to exponentially decaying sinusoidal waves moving away from the source. In this context, the cut-off frequency, approximately calculated as $\omega_0 = \sqrt{\frac{k_d}{\rho A}} \approx 557$ rad/s, marks a critical point in the system's response to external excitation's. This foundational understanding of the dispersion characteristics without metamaterials sets the stage for comparative analyses. By integrating metamaterials into the system, one can observe shifts in the dispersion curve, enabling a deeper comprehension of how these materials influence wave propagation, attenuation, and the emergence of bandgaps, thereby guiding the design and optimization of wave mitigation strategies.

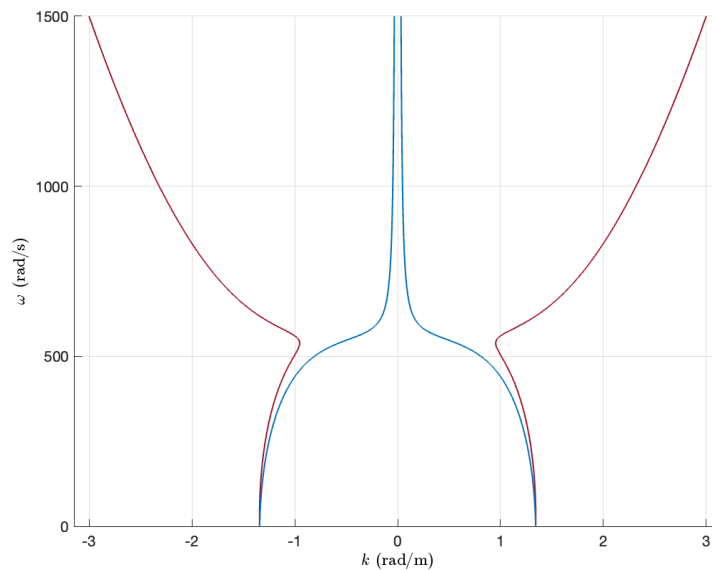


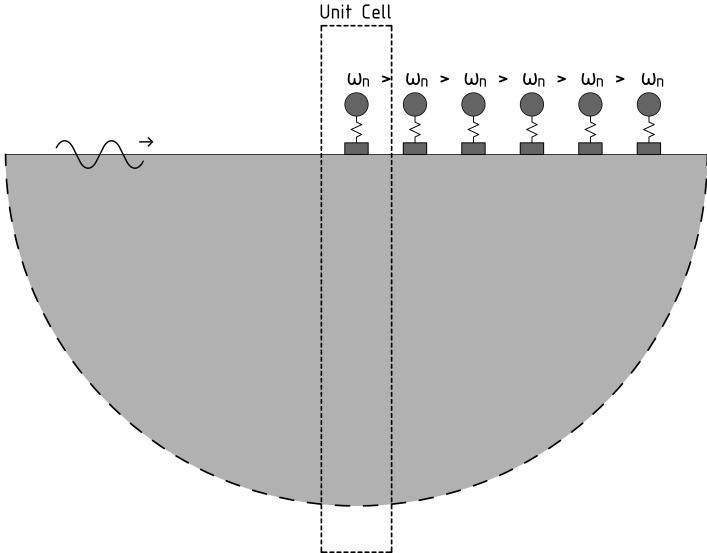
Figure 2.2: Dispersion curve of the Euler-Bernoulli beam on visco-elastic foundation, in red the real part of the wavenumbers and in blue the imaginary part

2.2. Metamaterial model description

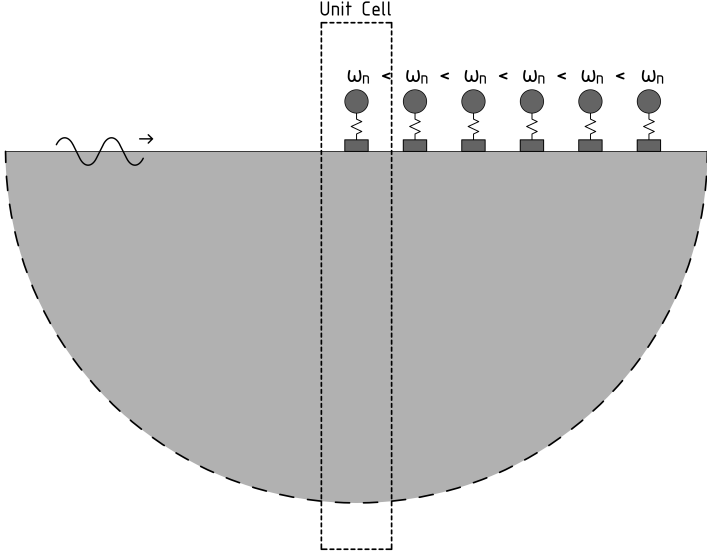
With the introduction of metamaterials, this thesis studies the fundamental physics of these structures and to develop a practical design. Among the various configurations of above surface resonators, a particular structure known as the "metawedge" [8] shows promise. A metawedge is a periodic assembly composed of unit cells, each with a natural frequency slightly different from its neighbors. To conceptu-

alize, one might imagine a metawedge as akin to a forest [9] where each consecutive row of trees has a different height, affecting its natural frequency due to the longitudinal mode's dependence on height. This conceptual forest would form a wedge shape when viewed from the side, giving rise to the term "metawedge". Depending on the direction of the incident wave—either starting from the shortest tree (highest natural frequency) and progressing to the tallest (lowest natural frequency) or vice versa—the metawedge is classified as either a classic or an inverse metawedge, respectively.

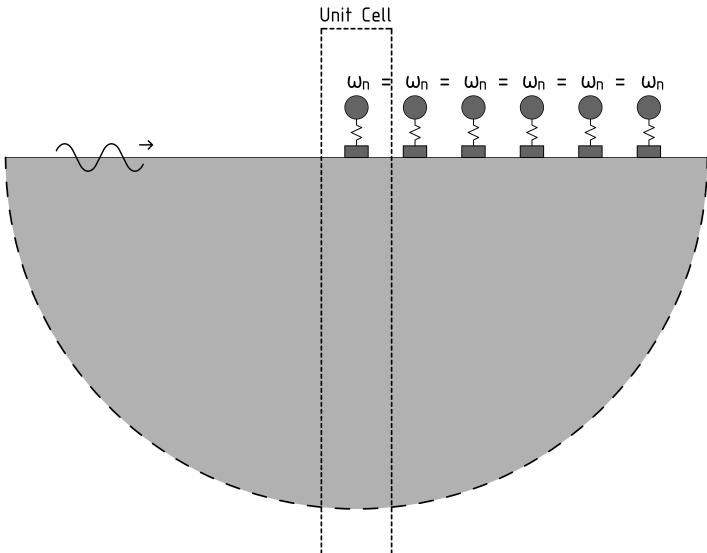
In this thesis, the focus will be on metamaterials constructed from single-degree of freedom oscillators. These oscillators, consisting of a mass, a spring (and potentially a dashpot), have tunable natural frequencies determined by their mass and spring stiffness. Unlike the conceptual forest, adjusting these parameters does not alter the physical height of the resonator, so the wedge analogy applies more to the variation in natural frequencies rather than any physical inclination. This chapter will concentrate on the "uniform metawedge", where all resonators share identical parameters and are evenly spaced. This simplification is necessary for the employed analytical model, which assumes infinite periodicity, making it incompatible with resonators of varying parameters. To explore the phenomena of local resonance and Bragg scattering, two distinct models are proposed. The first model adds local mass-spring-dash pots to the beam itself, depicted in figure 2.3a, effectively increasing the beam's stiffness without introducing local resonance. The second model introduces the metamaterials as resonators coupled to the beam, as shown in figure 2.3b, where both local resonance and Bragg scattering are expected to create bandgaps. This distinction between models facilitates a focused investigation into the specific mechanisms by which metamaterials can influence wave propagation.



(a) Classic metawedge

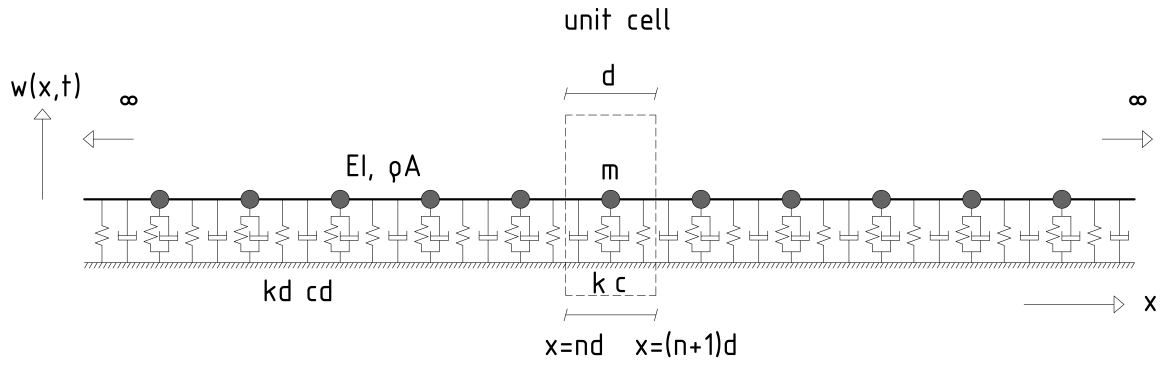


(b) Inverse metawedge

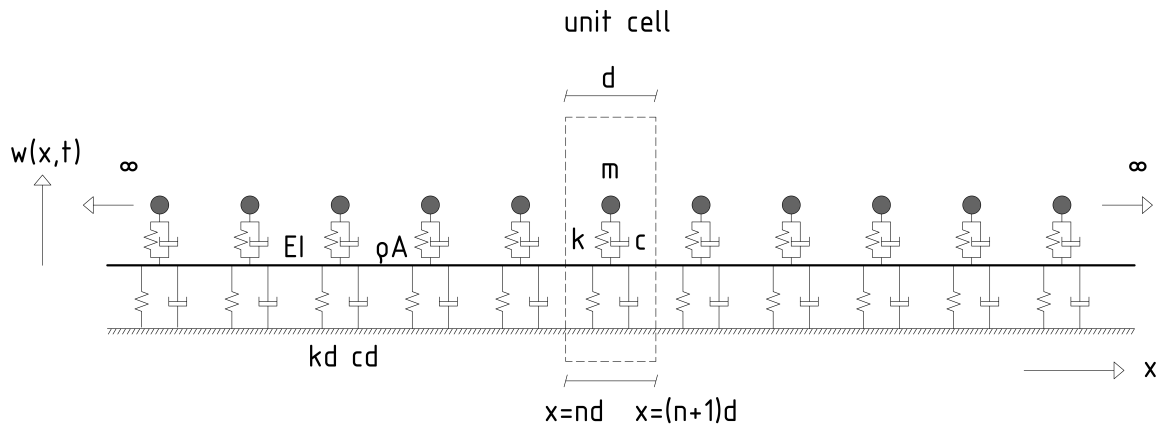


(c) Uniform metawedge

Figure 2.4: Different configurations of the metawedge



(a) Euler-Bernoulli beam with infinitely repeating periodic linked mass spring-dash-pots



(b) Euler-Bernoulli beam with infinitely repeating periodic single degree of freedom resonators

Figure 2.3: Euler-Bernoulli beam with metamaterial inclusions

2.3. Floquet analysis of model with fixed metamaterials

To conduct an analysis of the infinitely periodic system, a Floquet analysis will be employed, adhering to the methodology outlined in the study by Faragau et al. [15]. Although the original paper applied Floquet analysis to a string system with periodic supports, this study modifies the model by replacing the string with a beam positioned on a visco-elastic foundation. Despite this modification, the approach remains unchanged. The model under consideration consists of an infinite beam, which is supported by a series of distributed springs and dashpots. Discrete mass-spring-dashpot elements, which are arranged periodically along the beam, simulate the metamaterials. These periodic arrangements of mass-spring-dashpots define what is referred to as a unit cell within the model. Each unit cell is identified by its position along the beam, specified as $x \in [nd, (n+1)d]$, where n represents the cell number and d denotes the distance between each set of discrete supports. The mass-spring-dashpot element, serving as the focal point of each cell, is located precisely at the midpoint of the cell, defined by $x = \bar{n}d$ with $\bar{n} = n + \frac{1}{2}$. The equation of motion for this system encapsulates the dynamics of the beam, taking into account the distributed support provided by the springs and dashpots, as well as the localized support from the discrete mass-spring-dashpot elements.

$$\rho A \frac{\partial^2 w(x, t)}{\partial t^2} + EI \frac{\partial^4 w(x, t)}{\partial x^4} + c_d \frac{\partial w(x, t)}{\partial t} + k_d w(x, t) + \sum_{n=-\infty}^{\infty} \left(\frac{\partial^2}{\partial t^2} m + \frac{\partial}{\partial t} c + k \right) w(x, t) \delta(x - \bar{n}d) = 0 \quad (2.4)$$

The objective of this study is to develop an equation that connects the state variables (displacement, slope, moment, and shear force) at the edges of each cell within the system. This is accomplished initially by employing a forward Fourier transform over time, leading to Equation 2.5. By focusing the analysis on a generic cell, it can be conceptually divided into two distinct zones: one to the left of the support, represented by \tilde{w}_1 , and another to the right, denoted as \tilde{w}_2 . The solutions for these zones are presented in Equations 2.6 and 2.7, respectively, where γ symbolizes the wavenumber specific to the Euler-Bernoulli beam on a visco-elastic foundation. The unknowns D1-D4 can be expressed in the unknowns C1-C4 by using the interface conditions at the midpoint of the cell, $x = (n + \frac{1}{2})d$, within the Fourier domain. These conditions are detailed in Equations 2.9 through 2.12. The interface conditions can be derived by using the displacement, slope and moment continuity together with the dynamic shear force equilibrium.

$$EI \tilde{w}''''(x, \omega) + \left(-\omega^2 \rho A + i\omega c d + k d + \sum_{n=-\infty}^{\infty} (-\omega^2 m + i\omega c + k) \delta(x - \bar{n}d) \right) \tilde{w}(x, \omega) = 0 \quad (2.5)$$

$$\tilde{w}_1(x, \omega) = C_1 e^{-i\gamma x} + C_2 e^{i\gamma x} + C_3 e^{\gamma x} + C_4 e^{-\gamma x}, \quad nd \leq x \leq \left(n + \frac{1}{2}\right)d \quad (2.6)$$

$$\tilde{w}_2(x, \omega) = D_1 e^{-i\gamma x} + D_2 e^{i\gamma x} + D_3 e^{\gamma x} + D_4 e^{-\gamma x}, \quad \left(n + \frac{1}{2}\right)d \leq x \leq (n+1)d \quad (2.7)$$

$$\gamma = \left(\frac{\rho A}{EI} \left(\omega^2 - i\omega \frac{cd}{\rho A} - \omega_0^2 \right) \right)^{1/4} \quad (2.8)$$

$$\tilde{w}_1 = \tilde{w}_2 \quad (2.9)$$

$$\tilde{w}'_1 = \tilde{w}'_2 \quad (2.10)$$

$$\tilde{w}''_1 = \tilde{w}''_2 \quad (2.11)$$

$$EI \frac{\partial^3 \tilde{w}_1}{\partial x^3} = (-\omega^2 m + i\omega c + k) \tilde{w}_1 + EI \frac{\partial^3 \tilde{w}_2}{\partial x^3} \quad (2.12)$$

The terms C1-C4 can be expressed in terms of the state at $x = nd$, i.e. the displacement, slope, moment and shear force.

$$\tilde{w}_1(x = nd) = W \quad (2.13)$$

$$\tilde{w}'_1(x = nd) = \theta \quad (2.14)$$

$$EI \tilde{w}''_1(x = nd) = M \quad (2.15)$$

$$EI \tilde{w}'''_1(x = nd) = V \quad (2.16)$$

What results from the analysis is a 4x4 matrix that effectively connects the state variables at the beginning of a cell to those at the right boundary. This matrix encapsulates the relationship between displacement, slope, moment, and shear force across the cell, offering a comprehensive mathematical model for predicting how these variables change from one end of the cell to the other.

$$\tilde{\mathbf{w}}_n = \mathbf{F}^n \tilde{\mathbf{w}}_0 \quad (2.17)$$

Where \mathbf{F} is the Floquet matrix. To reveal the propagation characteristics of the system, an eigenvalue and eigenvector analysis can be performed on \mathbf{F} . The eigenvalues (α) and eigenvectors (\mathbf{u}) of the Floquet matrix \mathbf{F} can be found numerically using Matlab. From which the Floquet wavenumbers can be expressed as:

$$K^F = i \ln(\alpha) / d \quad (2.18)$$

Since the Floquet matrix is frequency dependent, it is necessary to calculate the wavenumbers for all frequencies, which can then be plotted to illustrate the dispersion curve. This is done using the following parameters. The parameters are chosen in such a way that they mimic the response of the soil and are taken from [14]. However, it should be noted that for the intended results, the exact values of the parameters are not of high importance.

Table 2.1: Model parameters

Parameter	Symbol	Value	Unit
Mass per unit length	ρA	268.3333	kg/m
Bending stiffness	EI	6.42e6	Nmm^2
Distributed spring stiffness	k_d	8.3333e+07	N/m^2
Damping ratio	ζ	5e-2	—
Metamaterial Mass	m	100	kg
Metamaterial spring stiffness	k	4.9e7	N/m
Metamaterial damping ratio	c	2.5e-2	—
Metamaterial spacing	d	1	m

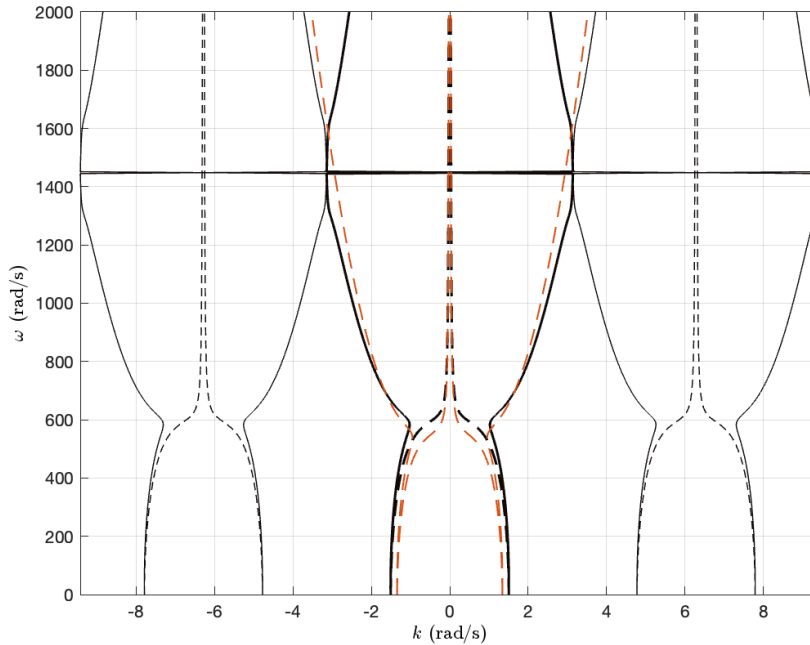


Figure 2.5: Dispersion curve of the Euler-Bernoulli beam on visco-elastic foundation in red, dispersion curve of beam with linked metamaterials in black

In the dispersion curve presented in Figure 2.5, the homogeneous case is depicted in red, while the dispersion curve for the beam integrated with metamaterials is shown in black. The first notable observation is the periodic nature of the curves, which are segmented into zones known as Brillouin zones [4], where the first zone is characterised by $[-\frac{\pi}{d}, \frac{\pi}{d}]$. The system's response comprises of a superposition of an infinite amount of wavenumbers. Yet, it is the branches closest to the curve corresponding to the beam without metamaterials that contain most of the energy. A critical feature observed in Figure 2.5 is the presence of a stop band, or band gap, ranging from a lower bound of approximately $\omega \approx 1350$ rad/s to an upper bound of $\omega \approx 1600$ rad/s. This band gap occurs at frequencies where the dispersion curve for the system with metamaterials intersects a wavenumber that aligns with the distance defined by the spacing between the resonators and the wavelength of the excited wave, as illustrated by the equation:

$$\lambda = \frac{2\pi}{\gamma} = \frac{2\pi}{\frac{\pi}{d}} = 2d \quad (2.19)$$

This relationship suggests that band gaps are expected at each integer multiple of half the wavelength, indicating a periodic pattern in the system's wave propagation characteristics influenced by the spacing of the metamaterial resonators. Moreover, the upper boundary of the band gap correlates with a frequency at which the homogeneous system, without metamaterials, has a wavelength proportional to the distance between resonators. This observation highlights a critical interaction between the wave's physical characteristics and the structural periodicity of the metamaterials. These phenomena, including the formation of band gaps and their relationship with the system's structural parameters, will undergo a detailed exploration in Chapter 2.4.1, aiming to further unravel the complex dynamics introduced by the integration of metamaterials into wave propagation systems.

2.3.1. Parametric study

The analytical derivation of the dispersion curves has elucidated the conditions under which band gaps occur within the context of a model integrating linked mass-spring-dashpots. Notably, a band gap is observed when the dispersion curve for the model with metamaterials intersects with wavenumbers that are integer multiples of the spatial spacing between the metamaterial elements. This phenomenon delineates the presence of a frequency range within which wave propagation is significantly attenuated or entirely blocked. The band gap's boundaries are further characterized by two critical points: the upper limit is defined by the point at which the beam without metamaterials encounters a wavenumber corresponding to an integer multiple of half the wavelength, and the lower limit is marked by a similar intersection for the beam with metamaterials. Given these insights, the forthcoming investigation will focus on understanding how various parameters influence the formation and characteristics of these bandgaps. Specifically, the analysis will concentrate on the mass and spring stiffness of the discrete supports. Additionally, the spacing between these discrete supports is of paramount interest, as it plays a crucial role in Bragg scattering processes that contribute to the development of bandgaps.

This focused investigation aims to unravel the intricate relationship between the structural attributes of the metamaterials and the emergent wave propagation behaviors. By systematically varying the mass, spring stiffness, and spacing of the discrete supports, the study seeks to identify how these parameters influence the location, width, and effectiveness of band gaps within the engineered system. The investigation into the influence of mass on the dispersion characteristics and band gap formation begins by exploring the effects of adjusting the mass of the discrete supports within the system. Specifically, the mass is modified to be twice as large (200 kg) and half as small (50 kg) as the baseline values listed in Table 2.1, while maintaining all other parameters constant. This approach allows for a focused examination of mass's role in wave propagation dynamics.

Figure 2.6 (a) illustrates the outcome of increasing the mass to 200 kg, revealing a notable expansion of the band gap. This enlargement is attributed to the downward shift of the band gap's lower boundary. The addition of mass alters the dispersion curve, causing it to lower, which in turn reduces the slope of the dispersion curve $\frac{\partial\omega}{\partial k}$. Such a change signifies a decrease in the group velocity of the waves, implying that waves within this modified system propagate more slowly compared to the baseline model. In Figure 2.6 (b), reducing the mass to 50kg results in a narrower band gap, confirming our hypothesis. As the mass decreases towards zero, the dispersion curve approaches that of the system without metamaterials, effectively shrinking the band gap. This change illustrates how diminishing mass leads

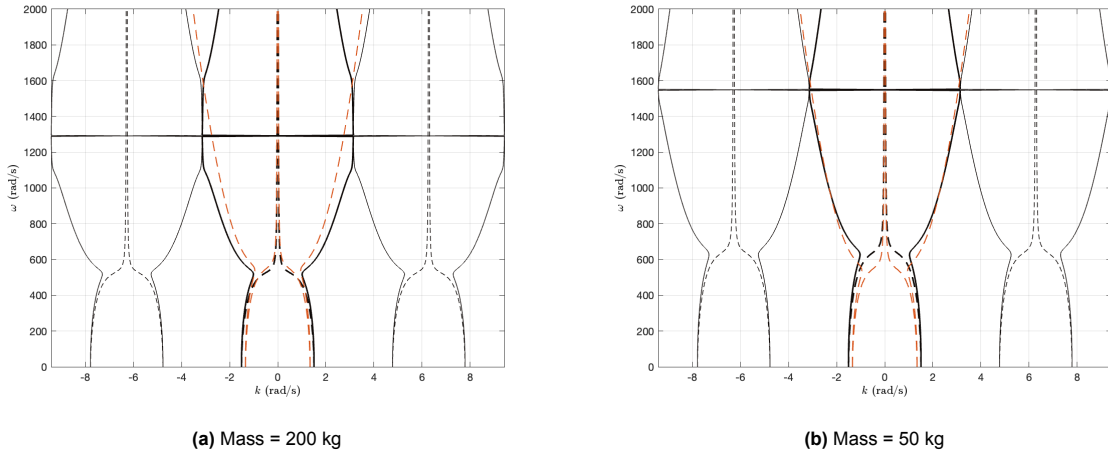


Figure 2.6: Influence of mass on the dispersion curve

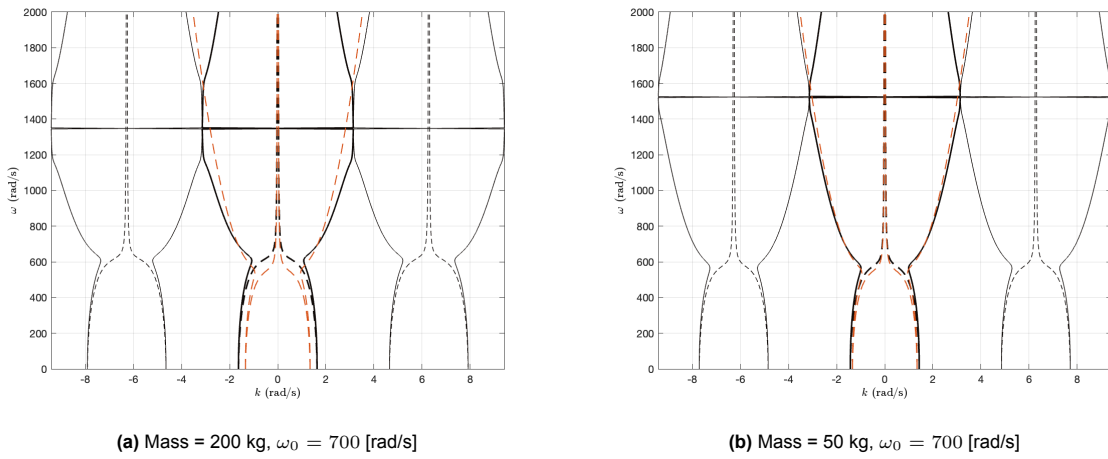


Figure 2.7: Influence of mass and spring stiffness on the dispersion curve

to parameters aligning more closely with those of the original beam, thus impacting the size of the band gap. As the mass decreases, both the lower and upper bounds of the band gap converge, further narrowing the band gap.

While adjusting the mass of the resonators, it inadvertently also affects their natural frequency ¹. In an attempt to isolate the impact of mass changes on the dispersion characteristics without altering the natural frequency, adjustments were made to the stiffness of the discrete supports, as depicted in Figure 2.7. These modifications aim to compensate for the mass changes, keeping the natural frequency constant. The observed differences between Figures 2.7 and 2.6 are minimal, suggesting that neither the stiffness nor the natural frequency significantly influences the formation of the band gap. This conclusion is reinforced by Figure 2.8, where variations in the stiffness of the discrete supports do not alter the width or location of the band gap, as initially observed in Figure 2.5. However, it is important to note that while the stiffness does not impact the Bragg band gap directly, it does influence the cut-off frequency, which can be considered a form of band gap. Therefore, the stiffness of the springs plays a role in shaping this specific band gap, but it does not affect the formation of the Bragg band gap.

The examination of resonator spacing confirms its critical role in dictating the location of the band gap, as demonstrated in Figure 2.9. The analysis aligns with theoretical predictions, showing the band gap's

¹The term "natural frequency" here may be misleading as the added masses do not possess independent degrees of freedom. Instead, this term is employed to denote a parameter that remains constant throughout the analysis.

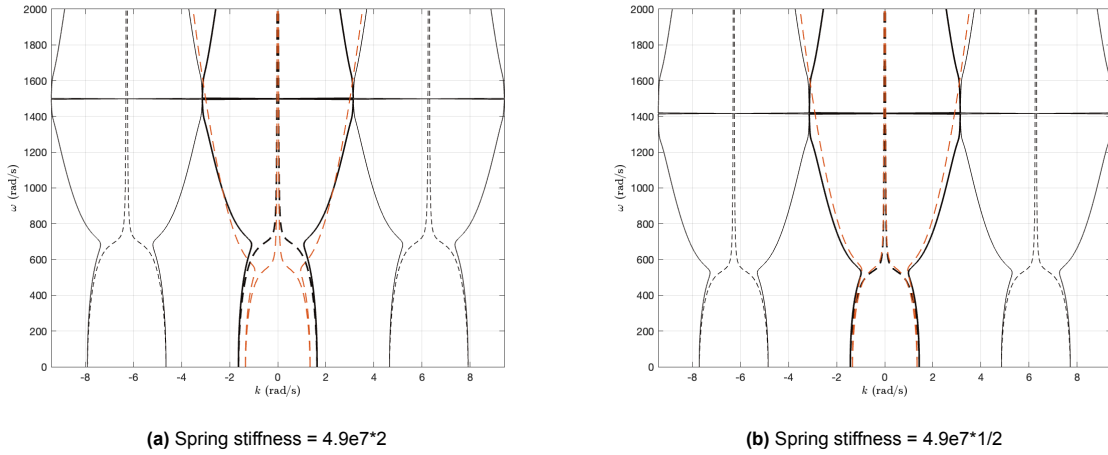


Figure 2.8: Influence of spring stiffness on the dispersion curve

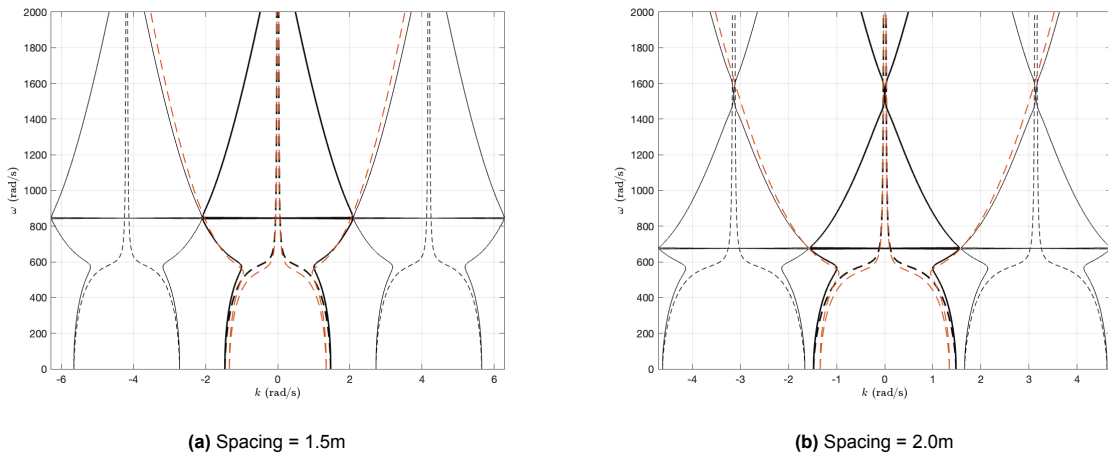


Figure 2.9: Influence of spacing on the dispersion curve

position at $k = 2.1$ [rad/s], which corresponds to the calculated value based on the spacing between supports. This finding is further corroborated in scenarios with different spacing's, where the expected locations of band gaps accurately match theoretical calculations based on the system's geometry. The location of these band gaps can be calculated using $k = \frac{n\pi}{d}$, with $n = 1, 2, 3, \dots$. Moreover, in figure (b) the width of the first band gap at $k = 1.57$ is observed to be relatively narrow, suggesting that the dispersion curve closely resembles that of the beam system without metamaterials at this frequency. In contrast, the band gap at $k = 3.14$ is broader, indicating a more significant alteration in wave propagation characteristics due to the presence of metamaterials. These results underscore that while resonator spacing is instrumental in determining the band gap's location, the mass of the resonators plays a crucial role in defining its width. This distinction provides valuable insights for designing metamaterial systems, emphasizing the importance of carefully considering both resonator spacing and mass to achieve desired wave propagation behaviors, particularly in the engineering of effective band gap-based wave mitigation strategies.

2.4. Floquet analysis of model with free metamaterials

Shifting focus to the scenario where each metamaterial possesses its own degree of freedom, this investigation anticipates the emergence of band gaps resulting not only from Bragg scattering, as observed in the previous model, but also from local resonance effects. The methodology employed will mirror that of Section 2.3, with pivotal distinctions being the incorporation of additional degrees of freedom, detailed in Equation 2.21, alongside modifications to the interface conditions, as specified in Equation

2.31. Each unit cell is identified by its position along the beam, specified as $x \in [nd, (n+1)d]$, where n represents the cell number and d denotes the distance between each set of discrete supports. Where the resonators, serve as the focal point of each cell and is located precisely at the midpoint of the cell, defined by $x = \bar{n}d$ with $\bar{n} = n + \frac{1}{2}$, as depicted in Figure 2.3b.

$$\rho A \frac{\partial^2 w(x, t)}{\partial t^2} + EI \frac{\partial^4 w(x, t)}{\partial x^4} + c_d \frac{\partial w(x, t)}{\partial t} + k_d w(x, t) + \sum_{n=-\infty}^{\infty} \left(\frac{\partial}{\partial t} c + k \right) (w(x = \bar{n}d, t) - w_{R,n}(t)) \delta(x - \bar{n}d) = 0 \quad (2.20)$$

$$m \frac{\partial^2}{\partial t^2} w_{R,n}(t) + c \frac{\partial}{\partial t} w_{R,n}(t) + k w_{R,n}(t) = c \frac{\partial}{\partial t} w(x = \bar{n}d, t) + k w(x = \bar{n}d, t), \quad \forall n \in \mathbb{Z} \quad (2.21)$$

A forward Fourier transform is applied to both equations of motion which results in:

$$EI \tilde{w}''''(x, \omega) + (-\omega^2 \rho A + i\omega c d + k d) \tilde{w}(x, \omega) + \sum_{n=-\infty}^{\infty} (i\omega c + k) (\tilde{w}(x = \bar{n}d, \omega) - \tilde{w}_{R,n}(\omega)) \delta(x - \bar{n}d) = 0 \quad (2.22)$$

$$-\omega^2 m \tilde{w}_{R,n}(\omega) + i\omega c \tilde{w}_{R,n}(\omega) + k \tilde{w}_{R,n}(\omega) = i\omega c \tilde{w}(x = \bar{n}d, \omega) + k \tilde{w}(x = \bar{n}d, \omega), \quad \forall n \in \mathbb{Z} \quad (2.23)$$

By focusing the analysis on a generic cell, it can be conceptually divided into two distinct zones: one to the left of the resonator, represented by \tilde{w}_1 , and another to the right, denoted as \tilde{w}_2 .

$$\tilde{w}_1(x, \omega) = C_1 e^{-i\gamma x} + C_2 e^{i\gamma x} + C_3 e^{\gamma x} + C_4 e^{-\gamma x}, \quad nd \leq x \leq \left(n + \frac{1}{2}\right) d \quad (2.24)$$

$$\tilde{w}_2(x, \omega) = D_1 e^{-i\gamma x} + D_2 e^{i\gamma x} + D_3 e^{\gamma x} + D_4 e^{-\gamma x}, \quad \left(n + \frac{1}{2}\right) d \leq x \leq (n+1)d \quad (2.25)$$

$$\tilde{w}_{R,1}(\omega) = A_1 e^{i\omega t} \quad (2.26)$$

$$\gamma = \left(\frac{\rho A}{EI} \left(\omega^2 - i\omega \frac{cd}{\rho A} - \omega_0^2 \right) \right)^{1/4} \quad (2.27)$$

The unknowns D1-D4 can be expressed in the unknowns C1-C4 by using the interface conditions at the midpoint of the cell, $x = \left(n + \frac{1}{2}\right) d$, within the Fourier domain.

$$\tilde{w}_1 = \tilde{w}_2 \quad (2.28)$$

$$\tilde{w}'_1 = \tilde{w}'_2 \quad (2.29)$$

$$\tilde{w}''_1 = \tilde{w}''_2 \quad (2.30)$$

$$EI \frac{\partial^3 \tilde{w}_1}{\partial x^3} = (i\omega c + k)(\tilde{w}_1 - \tilde{w}_{R,1}) + EI \frac{\partial^3 \tilde{w}_2}{\partial x^3} \quad (2.31)$$

The terms C1-C4 can be expressed in terms of the state at $x = nd$ i.e. the displacement, slope, moment and shear force.

$$\tilde{w}_1(x = nd) = W \quad (2.32)$$

$$\tilde{w}'_1(x = nd) = \theta \quad (2.33)$$

$$EI\tilde{w}''_1(x = nd) = M \quad (2.34)$$

$$EI\tilde{w}'''_1(x = nd) = V \quad (2.35)$$

What results from the analysis is a 4x4 matrix that effectively connects the state variables at the beginning of a cell to those at the right boundary. This matrix encapsulates the relationship between displacement, slope, moment, and shear force across the cell, offering a comprehensive mathematical model for predicting how these variables change from one end of the cell to the other.

$$\tilde{\mathbf{w}}_n = \mathbf{F}^n \tilde{\mathbf{w}}_0 \quad (2.36)$$

The same parameters are used as in the case of the linked degrees of freedom and can be found in Table 2.1.

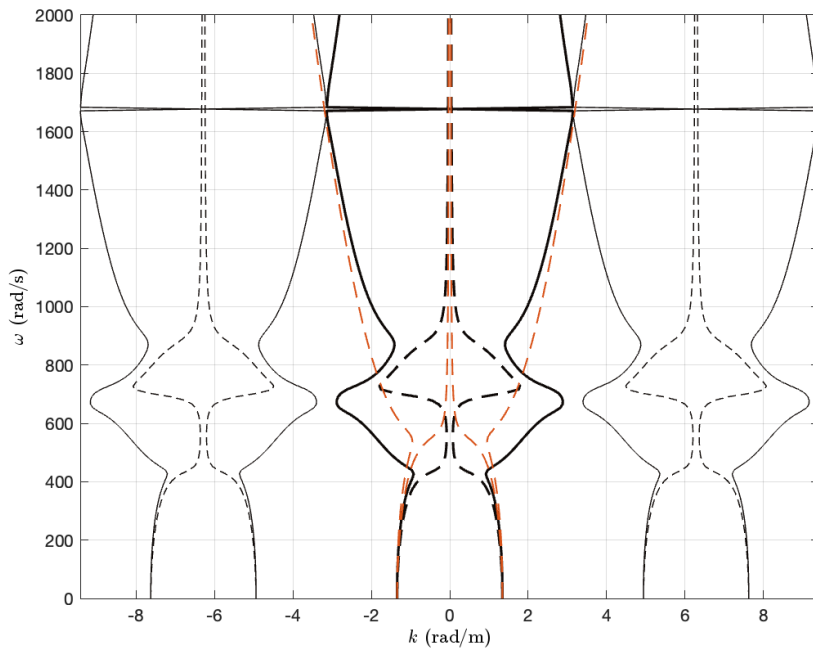


Figure 2.10: Dispersion curve of the Euler-Bernoulli beam on visco-elastic foundation in red, dispersion curve of beam with metamaterials in black

The dispersion curve derived for this model, which includes metamaterials with additional degrees of freedom, presents a significant difference compared to the findings in Section 2.3. A distinct band gap is now observable around the natural frequency of the resonators, identified as $\omega_o = \sqrt{\frac{k}{m}} \approx 700$ rad/s. This frequency range is marked by an increase in the imaginary part of wavenumbers (black dashed curve), suggesting the excitation of evanescent waves and, consequently, substantial wave attenuation within this band. Interestingly, the band gap primarily extends over frequencies exceeding the resonator's calculated natural frequency. This deviation from the expected $\sqrt{k/m}$ formula underscores the complexities of a coupled system, where the natural frequency is influenced by additional parameters beyond the simple mass-spring model. Nevertheless, the approximation $\sqrt{k/m}$ remains a useful indicator for preliminary design considerations, providing a near-approximation of the band gap's location.

The observation that the wavelengths of waves with frequencies near the band gap are not integer multiples of the spacing between resonators suggests that the band gap arises from local resonance, rather than Bragg scattering. This is in stark contrast to the observations in Figure 2.5, where clear band gaps were noted when wavelengths reached integer multiples of the spacing. At $k = \frac{\pi}{d} \approx 3.14$, the dispersion curves for systems with and without metamaterials closely align, indicating the diminished efficacy of this band gap as a mitigation measure. Such a scenario suggests that the resonators do not significantly influence the dispersion curve of the beam outside a frequency range centered around the resonator's natural frequency. This outcome hints at an analogy with a single degree of freedom system subjected to base excitation, where significant movement of the mass is not expected if the excitation frequency greatly exceeds the natural frequency of the resonator. Similarly, the addition of degrees of freedom in the beam system through metamaterials leads to localized effects around the natural frequencies of the resonators, limiting the impact on the overall dispersion characteristics of the beam. This insight underscores the nuanced influence of metamaterials on wave propagation and attenuation, emphasizing the role of local resonance in shaping the dynamic response of engineered systems. The shape of the dispersion curve does remind of a Fano resonance, which is the result of an interference between a narrow discrete resonance (like the resonance of the discrete supports) and a broad wave mode background. The constructive and destructive interference between these pathways leads to the characteristic asymmetric profile [22].

2.4.1. Parametric study

In the subsequent parametric study focusing on the influence of various parameters on the band gap, the natural frequency of the resonator emerges as a primary factor, influenced by either mass or stiffness. This study posits that the spacing between resonators plays a secondary role in this context. The investigation starts with examining the impact of mass changes on the band gap, with findings presented in Figure 2.11. These Figures illustrate a noticeable shift in the band gap's peak, correlating with changes in mass. For Figure 2.11(a), the peak of the band gap is expected around 495 rad/s, while for Figure 2.11(b), it shifts to around 990 rad/s, in line with the approximation of the natural frequency using $\sqrt{k/m}$. The observations from Figure 2.11 align closely with these calculations, indicating a significant influence of mass on the band gap's characteristics.

However, assessing the band gap's effectiveness is more complex. Although variations in the imaginary part of the wavenumbers suggest changes in attenuation potential, quantifying this effect requires a more detailed analysis, which is set aside for exploration in a subsequent chapter. To fully understand the impact of mass on the band gap, it is essential to consider its influence on the natural frequency of the resonator. Merely altering the mass without accounting for changes in natural frequency could lead to incomplete conclusions. Therefore, Figure 2.12 introduces an analysis where the mass is varied while simultaneously adjusting the spring stiffness to maintain a constant natural frequency. This approach ensures that any observed changes can be attributed more directly to the mass itself rather than its indirect effect on the system's resonant properties.

The outcomes from this methodological indicate that the band gap's location remains unchanged, suggesting that the natural frequency is indeed a critical factor in determining the band gap's position. However, an increase in the imaginary part of the wavenumbers was noted, implying potential changes in wave attenuation characteristics, though the precise implications of this increase are challenging to ascertain from the data provided. These observations are further supported by the analysis in Figure 2.13, where adjustments to the natural frequency are achieved through variations in spring stiffness, keeping the mass constant. The similarities between the results obtained in this scenario and those observed when directly changing the mass (as shown in Figure 2.11) reinforce the hypothesis that the natural frequency plays a pivotal role in defining the band gap's characteristics.

The examination of spacing's influence, as presented in Figure 2.14, corroborates the significance of resonator spacing on the band gap's location, particularly due to Bragg scattering mechanisms. Nonetheless, the resulting band gap is characterized by its narrow width. This narrowness arises because the resonators' addition marginally affects the dispersion curve, primarily outside the frequency range near their natural frequency. Consequently, the proximity of the band gap's upper and lower bounds diminishes its practical utility. This analysis underscores that, in scenarios where band gaps are primarily induced by local resonance, the metamaterials' natural frequency emerges as the paramount

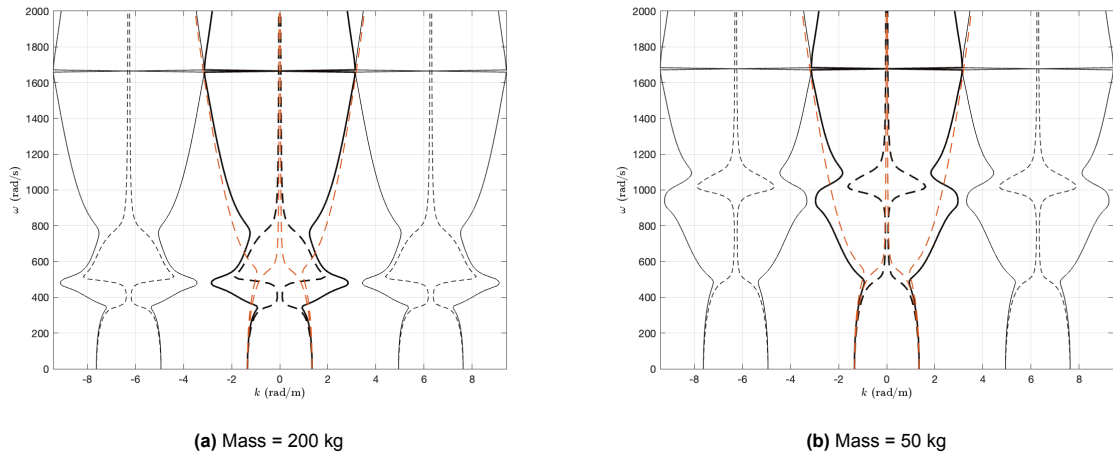


Figure 2.11: Influence of mass on the dispersion curve

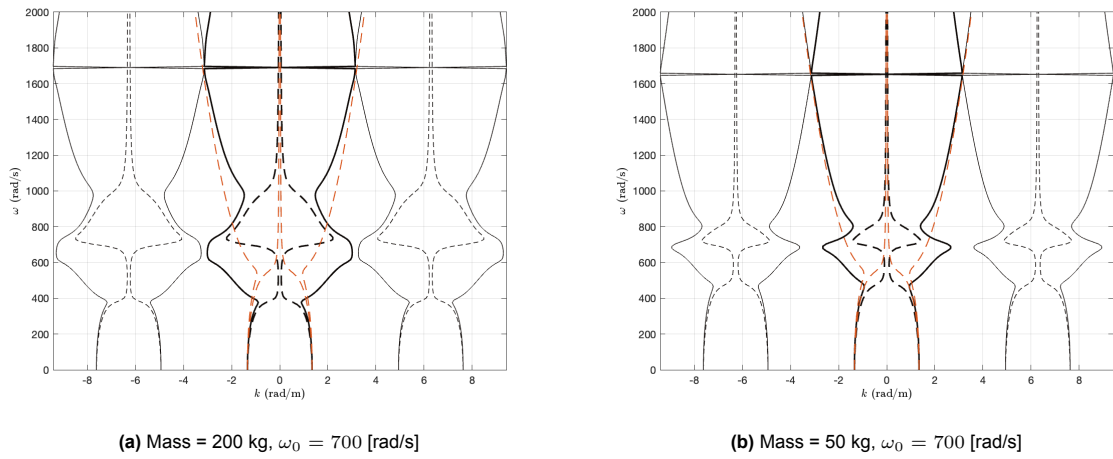


Figure 2.12: Influence of mass and spring stiffness on the dispersion curve

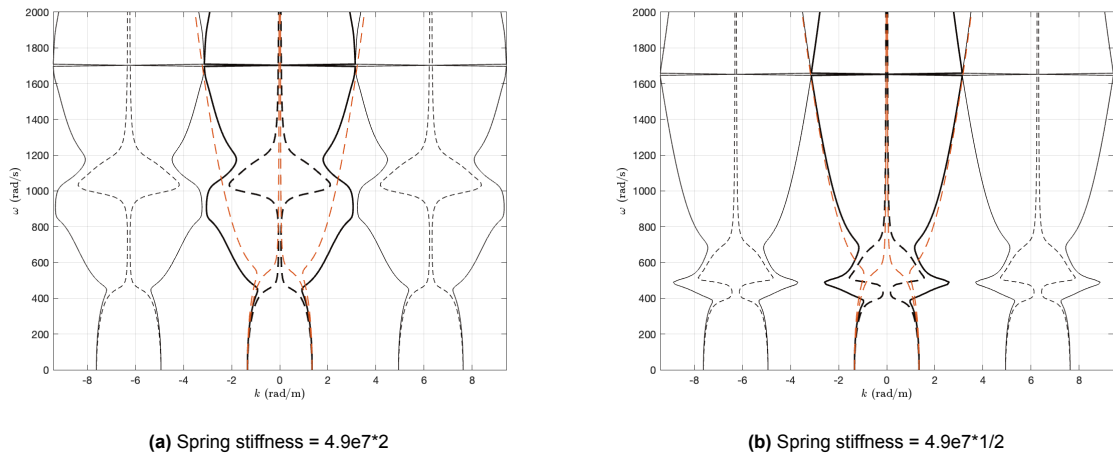


Figure 2.13: Influence of spring stiffness on the dispersion curve

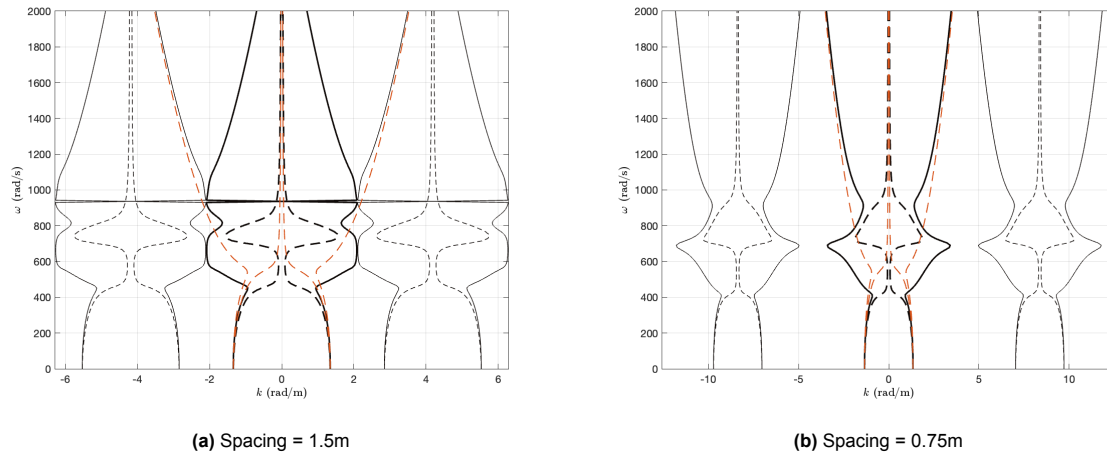


Figure 2.14: Influence of resonator spacing on the dispersion curve

factor in band gap formation and characteristics. Moreover, while the mass appears to play a role in modifying the attenuation level, drawing definitive conclusions about its impact requires further exploration. This aspect of mass's influence on wave attenuation, along with other nuanced effects of parameter variations on the band gap dynamics, is earmarked for detailed discussion in subsequent sections of the study.

2.5. Summary

The comprehensive investigation into the effects of fixed and free metamaterials on the dispersion characteristics of beams integrated with metamaterials has yielded insightful observations and nuanced understandings of wave propagation and attenuation mechanisms. This exploration, structured around the analytical derivation of dispersion curves and parametric studies, focused on elucidating the roles of mass, stiffness, and metamaterial spacing in shaping the band gaps essential for effective wave control. For systems with fixed metamaterials, the analysis revealed the significance of metamaterial spacing in defining the location of Bragg scattering-induced bandgaps. It was observed that adjustments to the mass and stiffness of resonators, while influencing the natural frequency, did not significantly alter the band gap's location but had implications for its width and the overall wave attenuation capacity. This highlighted the intricate balance between material properties and geometric configuration in determining the system's dynamic response.

Transitioning to systems with free degrees of freedom, the study emphasized the dominant influence of the natural frequency of resonators on the formation and characteristics of bandgaps, primarily those generated through local resonance. In this context, the spacing between resonators, while still relevant, played a less critical role in the band gap's formation compared to the fixed degrees of freedom scenario. Notably, the investigation into mass and stiffness adjustments, particularly when conducted in a manner that preserved the natural frequency, underscored the complexity of their contributions to the system's dispersion properties.

Across both fixed and free metamaterial systems, the paramount importance of the natural frequency and metamaterial spacing in band gap formation and the potential influence of mass on attenuation levels were consistently highlighted. These findings not only contribute to a deeper understanding of metamaterial-based wave manipulation strategies but also inform the design and optimization of such systems for practical applications. In conclusion, the study has advanced the understanding of how metamaterials can be strategically utilized to manipulate wave behavior in beams, offering innovative approaches to vibration mitigation and wave control in engineering applications. The findings highlight the necessity of a comprehensive analysis that accounts for the complex interactions within coupled systems, paving the way for the development of more effective metamaterial designs.

3

Numerical study of metamaterials on an Euler-Bernoulli beam

Moving from the exploration of an infinite periodic system discussed in Chapter 2, the next chapter will focus on analyzing a finite periodic system. The key question is whether the finite system retains the properties observed in its infinite counterpart. Given the departure from pure periodicity, an alternative approach is employed, where the system is analysed using a numerical model.

3.1. Adopted numerical model

Addressing the limitation of an infinite periodic system identified in Chapter 2, this chapter advances the discussion to a finite periodic system, exploring its behavior and properties in comparison to its infinite counterpart. A numerical model is proposed to study the effects of the finite model and to facilitate quick adjustments to the configuration of the metamaterials. This model employs the finite element method (FEM) to simulate wave propagation within a computational domain. FEM discretizes the continuous differential equation of motion, transforming the problem into a solvable discrete system. The method begins with the strong form of the elastodynamics equation, as shown in Equation 3.1, where ρ represents density and \ddot{u} the acceleration vector.

$$\rho \ddot{u} = \nabla \cdot \sigma + b \quad (3.1)$$

The journey from the strong form of the equation of motion to a solvable model involves deriving the weak form, followed by applying the Galerkin method to achieve a semi-discretized form. This semi-discretized form, still time-dependent, lays the groundwork for further discretization through time-stepping algorithms, categorized into explicit and implicit schemes.

$$M\ddot{a} + C\dot{a} + Ka = f \quad (3.2)$$

The Newmark-Beta method, a widely recognized time integration scheme in solid and structural mechanics, is employed for its stability and accuracy. By setting specific parameters, β and γ , the method ensures unconditional stability and second-order accuracy for the chosen configuration. This setup facilitates the discrete equation's formulation, which is then amenable to solution by linear system solvers. The Newmark algorithm gives \mathbf{a}_{n+1} and $\dot{\mathbf{a}}_{n+1}$ as:

$$\mathbf{a}_{n+1} = \mathbf{a}_n + \Delta t \dot{\mathbf{a}}_n + \frac{\Delta t^2}{2} ((1 - 2\beta)\ddot{\mathbf{a}}_n + 2\beta\ddot{\mathbf{a}}_{n+1}) \quad (3.3)$$

$$\dot{\mathbf{a}}_{n+1} = \dot{\mathbf{a}}_n + \Delta t ((1 - \gamma)\ddot{\mathbf{a}}_n + \gamma\ddot{\mathbf{a}}_{n+1}) \quad (3.4)$$

Where β and γ are parameters which define the nature and properties of the algorithm. The Newmark method is unconditionally stable for:

$$2\beta \geq \gamma \geq \frac{1}{2} \quad (3.5)$$

In this chapter the following parameters are chosen: $\beta = \frac{1}{4}$ and $\gamma = \frac{1}{2}$ for which the system is unconditionally stable and second-order accurate. Using the Newmark-Beta method the following equation can be discretized:

$$M\ddot{\mathbf{a}}_n + C\dot{\mathbf{a}}_n + K\mathbf{a}_n = \mathbf{f}_n \quad (3.6)$$

Which eventually can be written in a short form notation as:

$$\hat{K}\mathbf{a}_{n+1} = \hat{\mathbf{f}}_{n+1} \quad (3.7)$$

Which thereafter can be solved using a solver for linear systems. To account for the infinite nature of the beam outside the computation domain of the finite elements, boundary elements will be used. These boundary elements can be formulated in such a way that they function as non-reflective boundaries, mimicking the infinite nature of the beam. This system is schematically shown in Figure 3.1, in this Figure the computational domain is divided into three regions. The regions can be distinguished by whether or not metamaterials are present in them. These regions will later be used to assess the propagation characteristics.

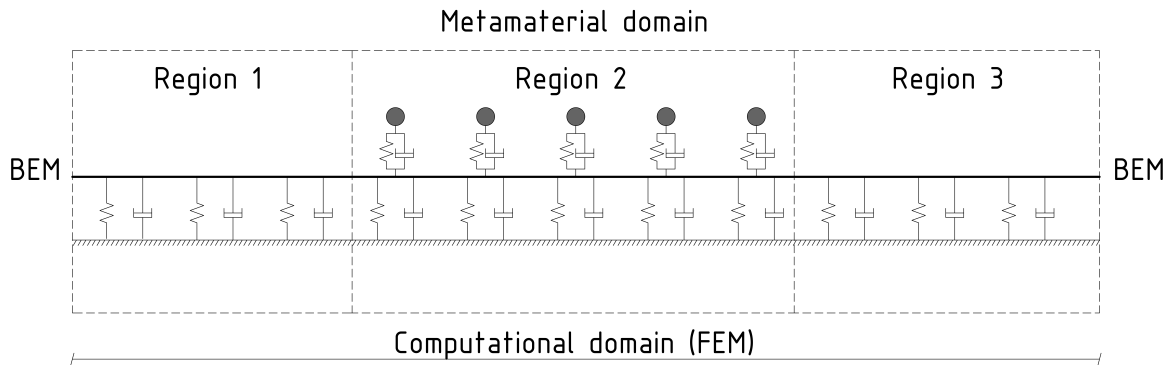


Figure 3.1: Adopted numerical model

3.2. Verification of the numerical model

To validate the numerical model, it will be benchmarked against two known cases: the Euler-Bernoulli beam theory on a visco-elastic foundation under a harmonic point load, and analytic expressions for wave transmission and reflection upon encountering a single unit cell of metamaterials, for both fixed and free cases. This approach ensures the model's accuracy in simulating both basic beam behavior and the specific effects of metamaterials.

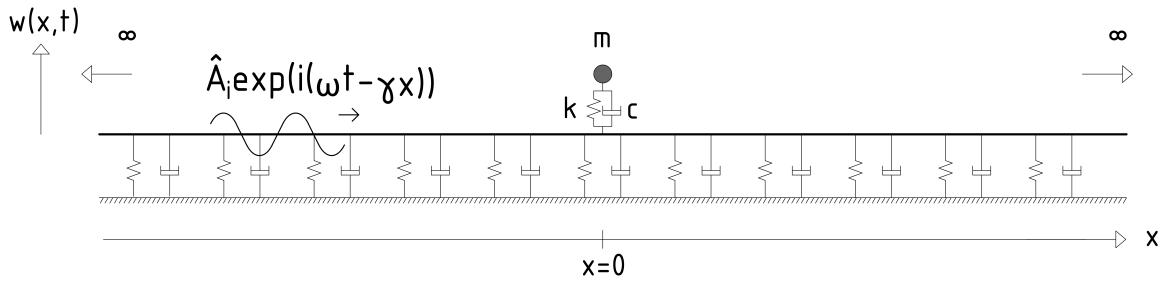


Figure 3.2: Euler-Bernoulli beam on visco-elastic foundation

3.2.1. Steady-State solution to a harmonic point load

To solve this problem the results of the homogeneous EoM from Chapter 2.1 can be used. The problem can be split up in two domains, one domain to the left of the force and one domain to the right of the force. The harmonic point load can be taken into account in the interface condition. w^+ is used to represent the domain to the right of the force and w^- represents the domain left of the force.

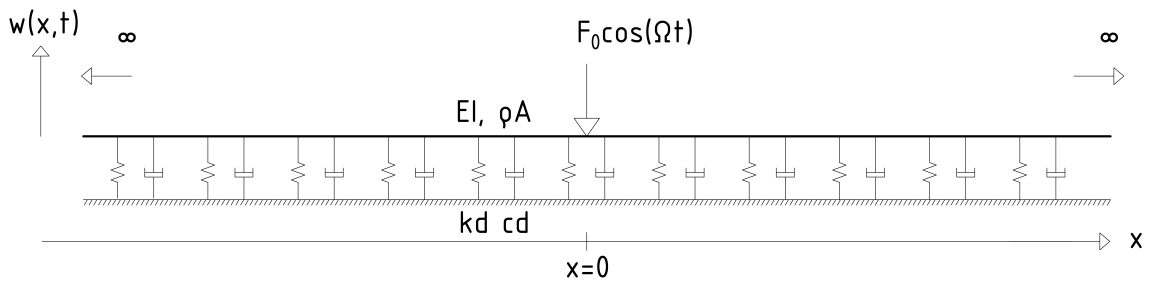


Figure 3.3: Euler-Bernoulli beam on visco-elastic foundation with harmonic excitation

$$\rho A \frac{\partial^2 w^+(x,t)}{\partial t^2} + EI \frac{\partial^4 w^+(x,t)}{\partial x^4} + c_d \frac{\partial w^+(x,t)}{\partial t} + k_d w^+(x,t) = \quad (3.8)$$

$$\rho A \frac{\partial^2 w^-(x,t)}{\partial t^2} + EI \frac{\partial^4 w^-(x,t)}{\partial x^4} + c_d \frac{\partial w^-(x,t)}{\partial t} + k_d w^-(x,t) = \quad (3.9)$$

The interface conditions at the location of the harmonic force, which is chosen at $x = 0$ for convenience, they expressions are as follows:

$$w^+(0, t) = w^-(0, t) \quad (3.10)$$

$$\frac{\partial w^+(0, t)}{\partial x} = \frac{\partial w^-(0, t)}{\partial x} \quad (3.11)$$

$$\frac{\partial^2 w^+(0, t)}{\partial x^2} = \frac{\partial^2 w^-(0, t)}{\partial x^2} \quad (3.12)$$

$$EI \left(\frac{\partial^3 w^+(0, t)}{\partial x^3} - \frac{\partial^3 w^-(0, t)}{\partial x^3} \right) = F_0 \cos(\Omega t) \quad (3.13)$$

The general solution facilitates the determination of the steady-state response. Utilizing symmetry, the solution can be expressed solely in terms of w^+ , thereby requiring only the consideration of wavenumbers that approach zero as x extends towards infinity.

$$\gamma^{(1)} = +\sqrt[4]{\frac{\rho A}{EI}\Omega^2 - i\frac{c_d}{EI}\Omega - \frac{k_d}{EI}} \quad (3.14)$$

$$\gamma^{(4)} = -i\sqrt[4]{\frac{\rho A}{EI}\Omega^2 - i\frac{c_d}{EI}\Omega - \frac{k_d}{EI}} \quad (3.15)$$

$$w(x, t) = \exp(i\Omega t) \left(\tilde{A}_1 \exp(-i\gamma^{(1)}x) + \tilde{A}_4 \exp(-i\gamma^{(4)}x) \right) \quad (3.16)$$

After substituting the general solution in the boundary conditions the unknown coefficients \tilde{A}_1 and \tilde{A}_4 are found.

$$\tilde{A}_1 = \frac{iF_0}{2EI\gamma^{(1)}((\gamma^{(4)})^2 - (\gamma^{(1)})^2)} \quad (3.17)$$

$$\tilde{A}_4 = \frac{-iF_0}{2EI\gamma^{(4)}((\gamma^{(1)})^2 - (\gamma^{(4)})^2)} \quad (3.18)$$

The analytical solution is compared with the numerical results, as shown in Figure 3.4. Although a slight variation in the wavelength of the numerical solution is observed, it can generally be concluded that there is very good agreement with the analytical case. The minor differences can be attributed to the fact that the analytical solution represents the steady-state solution, whereas the numerical results include transient effects.

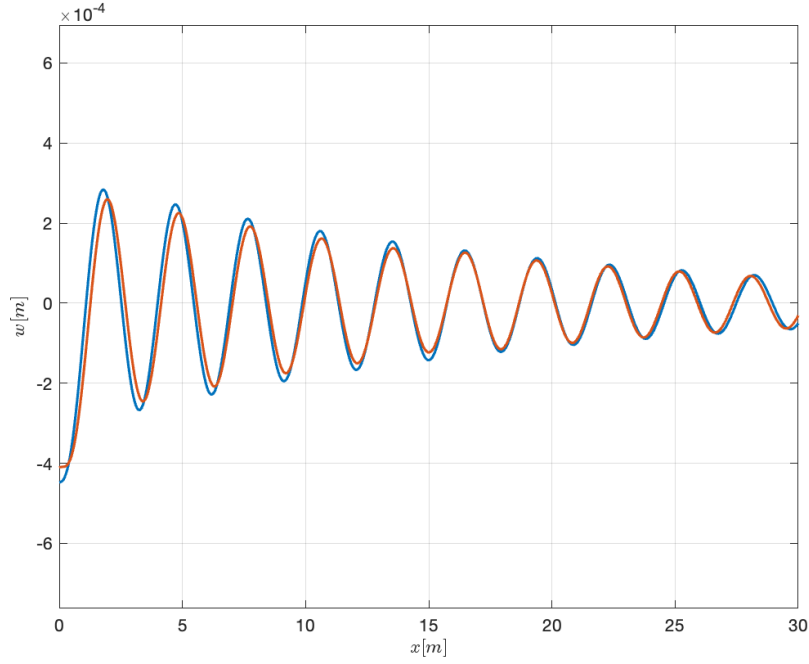


Figure 3.4: Euler-Bernoulli beam on visco-elastic foundation with harmonic excitation, analytic expression in blue, numerical expression in orange

3.2.2. Transmission and reflection at one fixed metamaterial

To verify the implementation of metamaterials, a comparative analysis between numerical results and analytical outcomes of a limit case will be conducted. This limit case considers a scenario with only one resonator, wherein the analytical solution can be easily derived. Analyzing such a case offers insights into the fundamental characteristics of metamaterials. Two scenarios will be examined: the "fixed" case, where the mass-spring-dashpots are directly connected to the beam, and the "free" case, where the additional mass is attached to the beam via a spring and dashpot mechanism, as depicted in Figure 3.2.

$$\rho A \frac{\partial^2 w_1(x, t)}{\partial t^2} + EI \frac{\partial^4 w_1(x, t)}{\partial x^4} + c_d \frac{\partial w_1(x, t)}{\partial t} + k_d w_1(x, t) = 0 \quad (3.19)$$

$$\rho A \frac{\partial^2 w_2(x, t)}{\partial t^2} + EI \frac{\partial^4 w_2(x, t)}{\partial x^4} + c_d \frac{\partial w_2(x, t)}{\partial t} + k_d w_2(x, t) = 0 \quad (3.20)$$

The interface conditions at the location of the metamaterial ($x = x_1$) can be defined as:

$$w_1(x_1, t) = w_2(x_1, t) \quad (3.21)$$

$$\frac{\partial w_1(x_1, t)}{\partial x} = \frac{\partial w_2(x_1, t)}{\partial x} \quad (3.22)$$

$$\frac{\partial^2 w_1(x_1, t)}{\partial x^2} = \frac{\partial^2 w_2(x_1, t)}{\partial x^2} \quad (3.23)$$

$$EI \frac{\partial^3 w_2(x_1, t)}{\partial x^3} - EI \frac{\partial^3 w_1(x_1, t)}{\partial x^3} + m \frac{\partial^2 w_2(x_1, t)}{\partial t^2} + c w_2(x_1, t) + k w_2(x, t) = 0 \quad (3.24)$$

The general solution to the equations of motion are as follows:

$$w_1(x, t) = \exp(i\Omega t) \left(\tilde{A}_1 \exp(-i\gamma^{(1)}x) + \tilde{A}_4 \exp(-i\gamma^{(4)}x) + \tilde{A}_{r1} \exp(i\gamma^{(1)}x) + \tilde{A}_{r4} \exp(i\gamma^{(4)}x) \right) \quad (3.25)$$

$$w_2(x, t) = \exp(i\Omega t) \left(\tilde{A}_{t1} \exp(-i\gamma^{(1)}x) + \tilde{A}_{t4} \exp(-i\gamma^{(4)}x) \right) \quad (3.26)$$

Substituting the general solutions into the boundary conditions enables the determination of unknowns \tilde{A}_{r1} , \tilde{A}_{r4} , \tilde{A}_{t1} , and \tilde{A}_{t4} . This allows for the formulation of a solvable system, which can be efficiently tackled using symbolic mathematics software like Maple. The analytical results derived can then be visualized and directly compared with those obtained from the numerical model, as in Figure 3.5. In this figure, the analytic expression is depicted in blue, while the numerical expression is shown in orange.

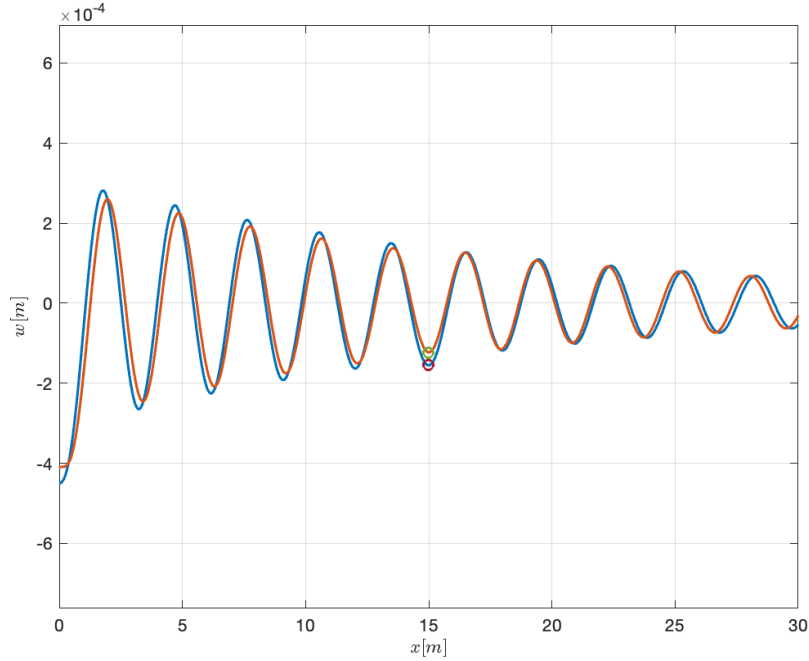


Figure 3.5: Transmission and reflection with one fixed interface, analytic expression in blue, numerical expression in orange

The comparison demonstrates a good agreement between the analytical and numerical approaches, validating the model's accuracy and the effectiveness of the solution strategy. The amplitude response functions, detailed in Figure 3.6, reveal that the inclusion of a local mass-spring-dashpot system introduces some reflection, leading to a noticeable decrease in amplitude beyond the resonator location. Notably, the absence of a clear band gap is consistent with the expectations for this configuration. Given that local resonance is prevented in this scenario and Bragg scattering is contingent upon the presence of multiple resonators, the observation aligns with theoretical predictions.

3.2.3. Transmission and reflection at one free metamaterial

In transitioning from the "Fixed" case to the model where the masses have their own degrees of freedom (DoF) and are not linked to the beam, a similar analytical procedure can be applied with key modifications. Specifically, the introduction of a separate equation of motion for the single degree of freedom (SDoF) resonator becomes necessary to accurately model its dynamics when decoupled from the beam's motion.

$$\rho A \frac{\partial^2 w_1(x, t)}{\partial t^2} + EI \frac{\partial^4 w_1(x, t)}{\partial x^4} + c_d \frac{\partial w_1(x, t)}{\partial t} + k_d w_1(x, t) = 0 \quad (3.27)$$

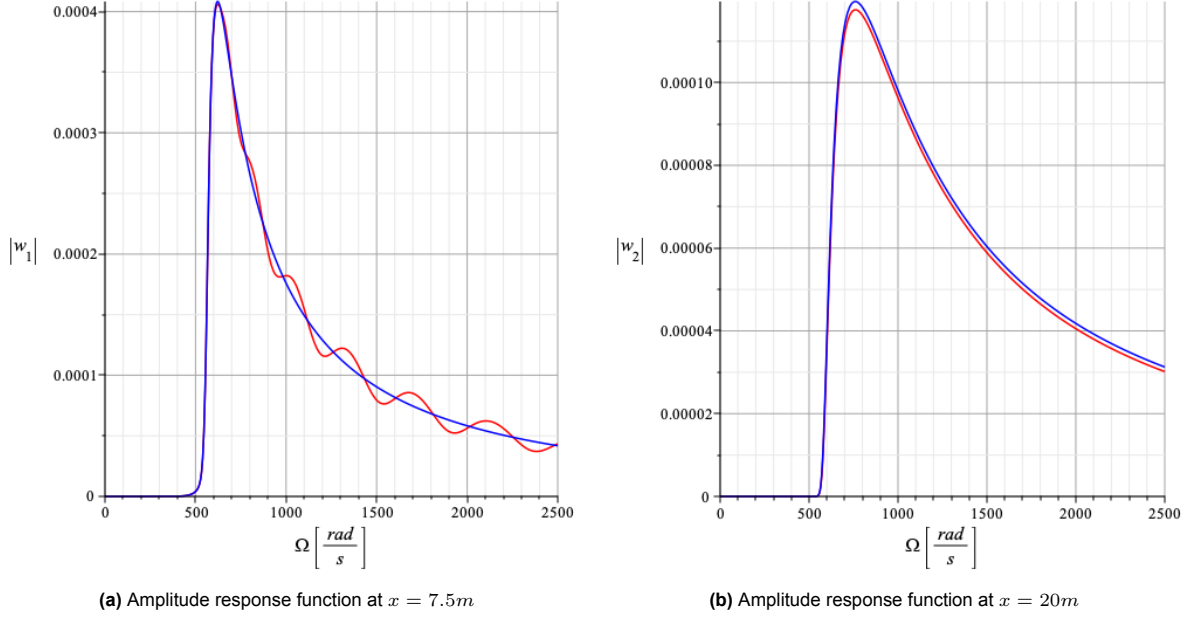


Figure 3.6: Amplitude response functions, in blue the homogeneous case, in red with the inclusion of one local mass-spring-dashpot

$$\rho A \frac{\partial^2 w_2(x, t)}{\partial t^2} + EI \frac{\partial^4 w_2(x, t)}{\partial x^4} + c_d \frac{\partial w_2(x, t)}{\partial t} + k_d w_2(x, t) = 0 \quad (3.28)$$

$$m \ddot{w}_3 + c \dot{w}_3 + k w_3 = c \dot{w}_1(x = x_1, t) + k w_1(x = x_1, t) \quad (3.29)$$

Subsequently, the interface conditions at $x = x_1$ can be defined. It is important to note that Equation 3.33 differs from the fixed case.

$$w_1(x_1, t) = w_2(x_1, t) \quad (3.30)$$

$$\frac{\partial w_1(x_1, t)}{\partial x} = \frac{\partial w_2(x_1, t)}{\partial x} \quad (3.31)$$

$$\frac{\partial^2 w_1(x_1, t)}{\partial x^2} = \frac{\partial^2 w_2(x_1, t)}{\partial x^2} \quad (3.32)$$

$$EI \left(\frac{\partial^3 w_2(x_1, t)}{\partial x^3} - \frac{\partial^3 w_1(x_1, t)}{\partial x^3} \right) + c (\dot{w}_1(x_1, t) - \dot{w}_3(t)) + k (w_1(x_1, t) - w_3(t)) = 0 \quad (3.33)$$

The general solutions to above equations of motion are:

$$w_1(x, t) = \exp(i\Omega t) \left(\tilde{A}_1 \exp(-i\gamma^{(1)} x) + \tilde{A}_4 \exp(-i\gamma^{(4)} x) + \tilde{A}_{r1} \exp(i\gamma^{(1)} x) + \tilde{A}_{r4} \exp(i\gamma^{(4)} x) \right) \quad (3.34)$$

$$w_2(x, t) = \exp(i\Omega t) \left(\tilde{A}_{t1} \exp(-i\gamma^{(1)} x) + \tilde{A}_{t4} \exp(-i\gamma^{(4)} x) \right) \quad (3.35)$$

$$w_3(t) = \tilde{A}_5 \exp(i\Omega t) \quad (3.36)$$

Solving for the unknowns \tilde{A}_{r1} , \tilde{A}_{r4} , \tilde{A}_{t1} , \tilde{A}_{t4} , and \tilde{A}_5 with symbolic software like Maple enables the analytical exploration of the case with one free metamaterial. This analytical solution provides a basis for understanding the interaction between the beam and an isolated resonator. The results of this analysis,

are visualized in Figure 3.7, with analytic expressions depicted in blue and numerical expressions in orange. Again an excellent agreement between numerical and analytical results can be observed.

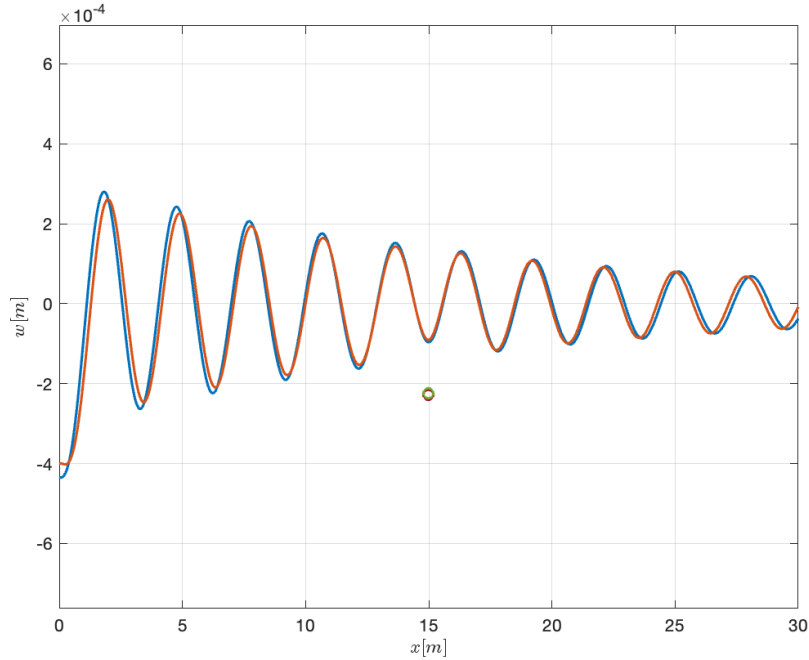


Figure 3.7: Transmission and reflection at one free interface, analytic expression in blue, numerical expression in orange

The analysis of amplitude response functions, as depicted in Figure 3.8, reveals that the integration of a local mass-spring-dashpot system functions analogously to a tuned mass damper. This is evidenced by an amplitude increase near the system's natural frequency and a subsequent reduction in the beam's displacement beyond the resonator for frequencies proximate to the resonator's natural frequency. Observing the displacement on the beam's side preceding the resonator indicates that certain frequencies result in amplification, while others lead to a reduction in displacement. The peak observed in the frequency response function of the resonator is pivotal, marking the natural frequency of the coupled beam-resonator system. Notably, this frequency is slightly higher than that predicted by treating the system as a decoupled single degree of freedom (SDoF) system, where the natural frequency is estimated using $\sqrt{k/m}$. This shift in the natural frequency, aligning with observations made in Chapter 2.4, underscores the impact of coupling between the beam and the resonator on the system's dynamic behavior.

3.3. Wave characteristics of the finite periodic system

With the numerical model now validated, the next objective is to explore whether finite periodic meta-material systems exhibit behaviors akin to their infinite periodic counterparts. This investigation centers on analyzing the dispersive properties of the system, which are pivotal in determining the similarities between the finite and infinite configurations. The computational model is structured into three distinct regions, as illustrated in Figure 3.1, to facilitate this analysis. The extraction of dispersive properties involves identifying the wavenumbers present within the solution for each region. This is achieved through the application of a wavenumber transform, analogous to a Fourier transform. However, instead of multiplying the solution with $\exp(-i\omega t)$, the wavenumber transform utilizes $\exp(+ikx)$, with the remainder of the procedure mirroring that of a traditional Fourier analysis. This method enables the identification of wavenumbers that dominate the steady-state response of the system. By applying the wavenumber transform across a range of excitation frequencies, the dispersion curves for each of the three designated regions within the computational model can be retrieved. The parameters used in this study are presented in Table 3.1.

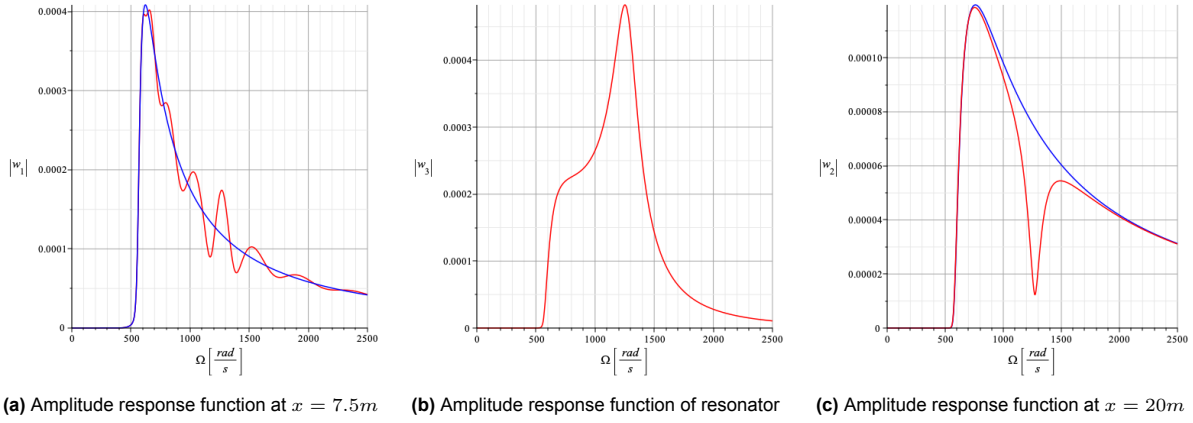


Figure 3.8: Amplitude response functions, in blue the homogeneous case, in red with the inclusion of one resonator

Table 3.1: Model parameters

Parameter	Symbol	Value	Unit
Length region 1	L_1	10	m
Length region 2	L_2	10	m
Length region 3	L_3	10	m
Mass per unit length	ρA	268.3333	kg/m
Bending stiffness	EI	6.42e6	Nmm^2
Distributed spring stiffness	k_d	8.3333e+07	N/m^2
Distributed damping ratio	ζ	5e-2	—
Metamaterial Mass	m	100	kg
Metamaterial spring stiffness	k	4.9e7	N/m
Metamaterial damping ratio	ζ	2.5e-2	—
Metamaterial spacing	d	1	m

3.3.1. System with fixed metamaterials

The dispersive characteristics of a finite periodic system with fixed metamaterials, were analyzed using the wavenumber transform. This analytical approach facilitated a comparative study between the finite system's dispersive behavior and that of its infinite periodic counterpart. The results of this analysis are depicted in Figure 3.9, where the dispersive characteristics for each region within the computational model are highlighted. The dispersion curve of region 1, presented in blue, closely aligns with the dispersion curve observed in the homogeneous case, indicating that the wave behavior is similar to the one of the beam without metamaterials. The curve for the region embedded with metamaterials is shown in green. While there are slight deviations from the dispersion curve obtained via Floquet analysis the overall correlation is strong, affirming the model's validity in capturing essential dispersion properties. region 3's dispersion curve, illustrated in orange, exhibits significant overlap with that of region 1, reinforcing the notion that areas outside the metamaterial domain exhibit similar wave propagation characteristics to the homogeneous medium. Any minor discrepancies observed when compared to the homogeneous case can be attributed to transient effects, as previously noted in the comparison of analytical and numerical results in Figure 3.7, where slight variations in wavelength were detected.

The comparison of responses between configurations with and without metamaterials facilitates the calculation of the amplitude ratio, depicted in Figure 3.10. An amplitude ratio of one indicates no reduction in wave amplitude, whereas a ratio of zero signifies total attenuation. This Figure reveals the presence of a band gap within the frequency range of 1200 rad/s to 1600 rad/s, where wave propagation is significantly reduced. The upper boundary of this band gap aligns with that observed in the infinite periodic system analysis, aligning with expectations since it is determined by the characteristics of the homogeneous beam. Conversely, the lower boundary of the band gap exhibits a downward shift. This adjustment is attributed to the corresponding shift in the dispersion curve for the beam integrated with metamaterials, resulting in the relevant wavenumber—and consequently, the band gap—being

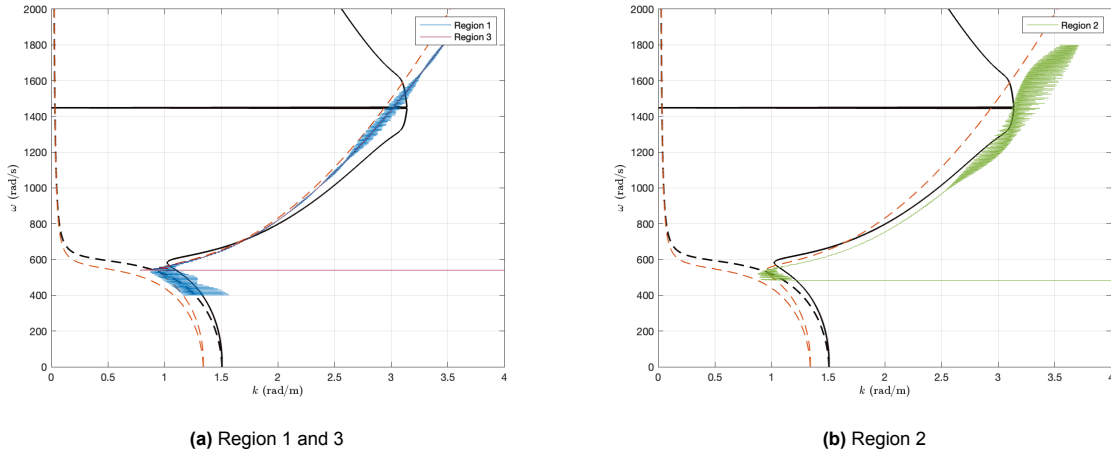


Figure 3.9: Numerically retrieved wavenumbers

identified at a lower frequency. Additionally, a secondary band gap is identified at 600 rad/s, distinct from the primary band gap associated with Bragg scattering. This secondary band gap emerges due to alterations in the cut-off frequency relative to the homogeneous system, underscoring the complex interplay between metamaterial configuration and the resultant wave propagation dynamics within the system.

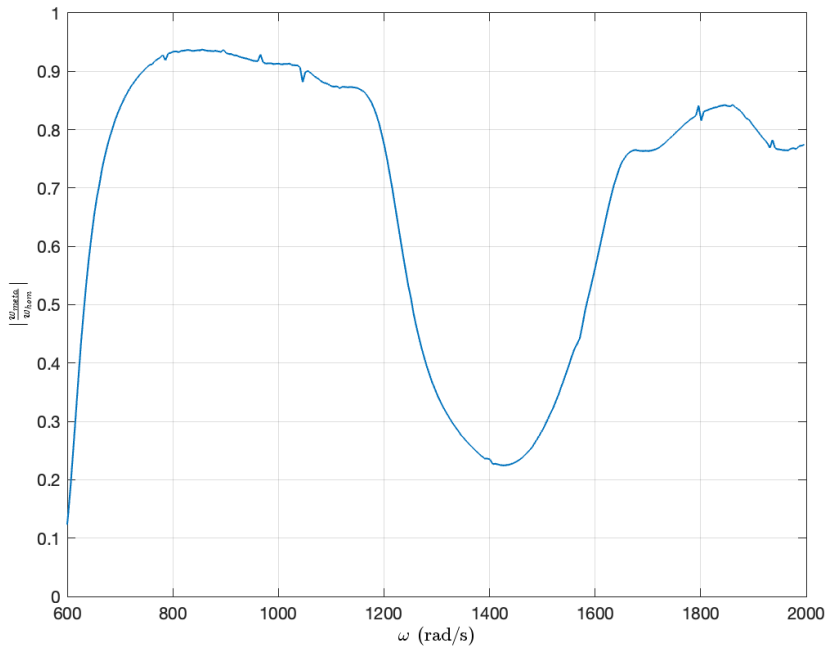


Figure 3.10: Amplitude ratio taken at $x = 26m$

3.3.2. System with free metamaterials

Turning to the analysis of the model with free degrees of freedom, the methodology employed in the fixed case is replicated. This involves applying the wavenumber transform across various frequencies to ascertain the prevailing wavenumbers within each defined region. The outcomes of this approach are encapsulated in Figure 3.11, where the dispersion curves for each region are delineated. The dispersion curve for region 1, illustrated in blue, exhibits strong conformity with that of the homogeneous

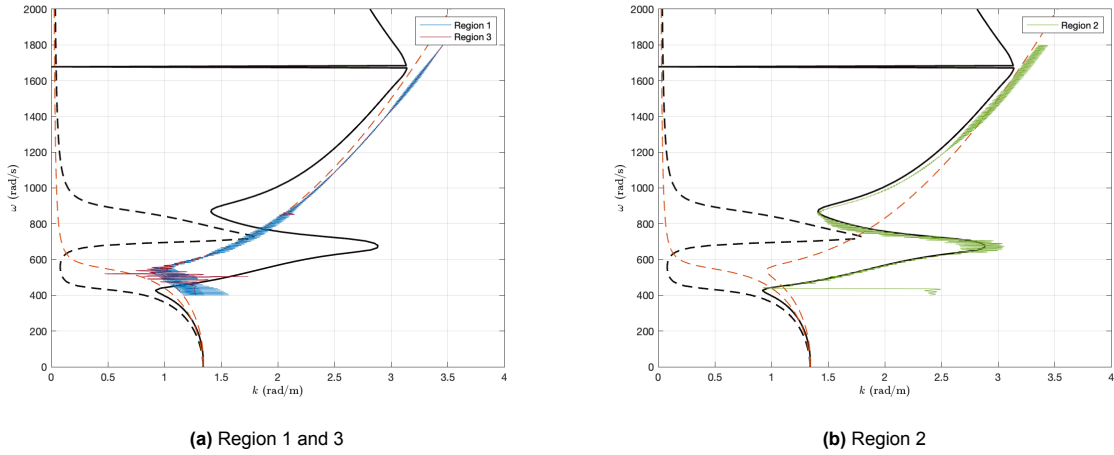


Figure 3.11: Numerically retrieved wavenumbers

system, underscoring the model's accuracy in replicating known wave behaviors in areas without metamaterials. The metamaterial region's dispersion curve, depicted in green, aligns remarkably well with the predictions of Floquet analysis. This alignment is particularly noteworthy given the finite nature of the system, incorporating only 11 resonators, yet achieving a high degree of correlation with the infinite periodic system analysis.

The orange curve, representing the dispersion characteristics of region 3, largely mirrors those of region 1, reinforcing the consistency of wave behavior in segments of the model unaffected by the presence of metamaterials. A notable exception occurs between 650 and 850 rad/s, where there is an absence of identifiable wavenumbers. This phenomenon is attributed to the metamaterials' capacity for strong wave attenuation, effectively halting transmission within this frequency range. The close alignment between the dispersion curves of the finite and infinite periodic systems suggests that the dispersion characteristics derived from Floquet analysis can serve as a reliable approximation for finite systems. This insight highlights the utility of Floquet analysis in predicting the wave behavior of systems incorporating a finite number of resonators, offering a valuable tool for the design and analysis of metamaterial-based wave control strategies.

Analysis of the dispersion curve reveals the formation of two distinct band gaps within the system: one attributable to the local resonance of metamaterials around 700 rad/s and another resulting from Bragg scattering at 1600 rad/s. The Bragg scattering band gap aligns precisely with predictions from Floquet analysis conducted on the infinite model. However, this band gap is characterized by its narrow width due to the proximity of its upper and lower bounds and exhibits only minimal wave attenuation, as depicted in Figure 3.12, which limits its practical utility. Conversely, the band gap induced by local resonance presents a more promising avenue for wave attenuation. Remarkably, with merely 11 resonators incorporated into the model, it is possible to achieve complete attenuation of incoming waves at the targeted frequency, as shown in Figure 3.12. This outcome notably surpasses the performance observed in the fixed model scenario, highlighting the efficacy of leveraging local resonance mechanisms.

The advantages of employing local resonance for band gap generation are manifold, especially when compared to the limitations associated with Bragg scattering band gaps. Notably, local resonance allows for more straightforward targeting of lower frequencies, such as those excited from trains. Given that lower frequencies correspond to longer wavelengths, creating an effective band gap through Bragg scattering would necessitate extensive spatial configurations. In contrast, local resonance band gaps can be finely adjusted to specific frequencies, offering a more versatile and efficient solution for wave control applications. Moreover, the attenuation capability of the band gap generated through local resonance mechanisms appears significantly more robust than that of its Bragg scattering counterpart. This distinction underscores the potential of local resonance-based designs in the development of metamaterials for effective wave attenuation, particularly in contexts where control over lower frequency ranges is paramount.

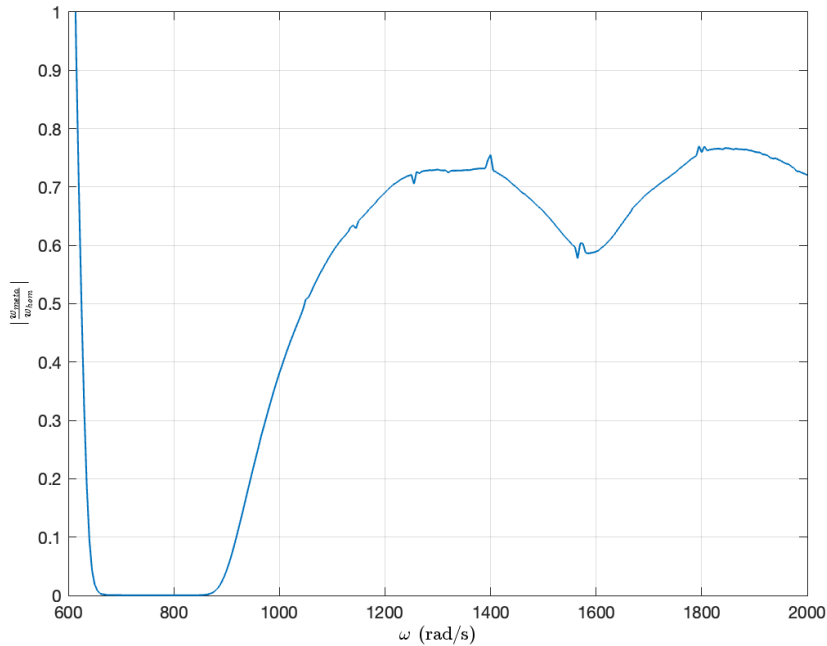


Figure 3.12: Amplitude ratio taken at $x = 26m$

3.4. Behaviour of the inverse and classic metawedge

The analysis thus far was centered on the uniform metawedge, characterized by resonators with identical natural frequencies. The concept of the classic and inverse metawedge, as introduced by Colombi et al. [8], presents a nuanced behavior contingent upon their configuration, which until now remained unexplored due to the analytical limitations associated with the necessity for periodicity in Floquet analysis. The development of a numerical model capable of elucidating the dispersion characteristics of metamaterials has now made it feasible to examine the distinct behaviors of the classic and inverse metawedge.

In the classic metawedge configuration, incident waves are observed to decelerate upon entry, halting at the resonator whose fundamental frequency aligns with the wave's frequency, thereby initiating a band gap effect that reflects the wave's energy akin to a rigid barrier. This phenomenon, termed "rainbow trapping" [8] signifies a unique wave manipulation capability. Conversely, the inverse metawedge configuration demonstrates a transformative interaction with incident Rayleigh waves, converting them into shear waves that are subsequently redirected into the substrate's interior, a process known as "mode-conversion." This mode-conversion presents a stark contrast to the reflective behavior observed in the classic wedge configuration and highlights a fundamentally different approach to energy redirection and dissipation.

While Colombi et al.'s work illuminates the potential of these configurations in directing wave propagation, it leaves the underlying mechanisms of mode-conversion unexplored. Nevertheless, the promise shown by their numerical simulations in manipulating wave directions offers intriguing possibilities for energy dissipation strategies. The forthcoming chapters aim to study the mitigation mechanisms employed by both the classic and inverse metawedge configurations and evaluate their effectiveness. The initial phase of this investigation will employ the one-dimensional numerical model proposed earlier. It is important to note that while this model facilitates a foundational understanding of these configurations, its one-dimensional nature precludes the ability to simulate the mode-conversion phenomena. Despite this limitation, this exploratory step is anticipated to yield significant insights into the operational principles of the classic and inverse metawedge, laying the groundwork for more complex analyses in future chapters.

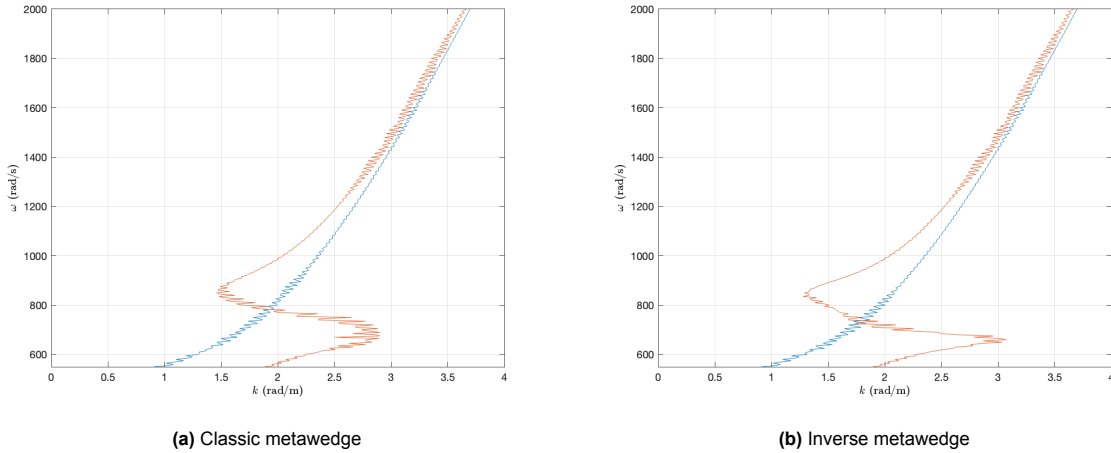


Figure 3.13: Numerically retrieved wavenumbers for the classic and inverse metawedge

In Figure 3.13, the dispersive characteristics for both the classic and inverse metawedge configurations are presented, based on numerical analysis. It is important to note that this cannot be considered a true dispersion curve because the wavenumber is derived from an accumulation of all unit cells, each with distinct properties. As such, the wavenumber obtained does not represent the dispersive properties of any single cell but instead reflects an average over all cells. The dispersive characteristics observed here are notably akin to those identified in the uniform metawedge scenario, including the emergence of a Fano-like shape within the curve. However, an examination of the curve alone does not immediately reveal any distinct behavioral deviations from the uniform case. Thus, the investigation extends to analyzing amplitude ratios succeeding the metawedge to discern the presence and characteristics of band gaps, as shown in Figure 3.14. The examination of amplitude ratios subsequent to the metawedge offers definitive insights into the band gaps produced by these configurations. It is inferred that the classic and inverse metawedge configurations contribute to an expansion of the band gap, attributed to the excitation of a broader range of resonators. While not explicitly depicted in the provided figure, an extrapolation based on complementary results suggests that as the band gap broadens, its attenuation efficacy diminishes. This observation is rationalized by the dispersion of energy across a wider array of resonators, each targeting specific frequencies less singularly. A second observation is that these results appear nearly identical, even when compared to the uniform metawedge depicted in Figure 3.12. This suggests that, from the perspective of the receiver, all configurations provide similar levels of mitigation.

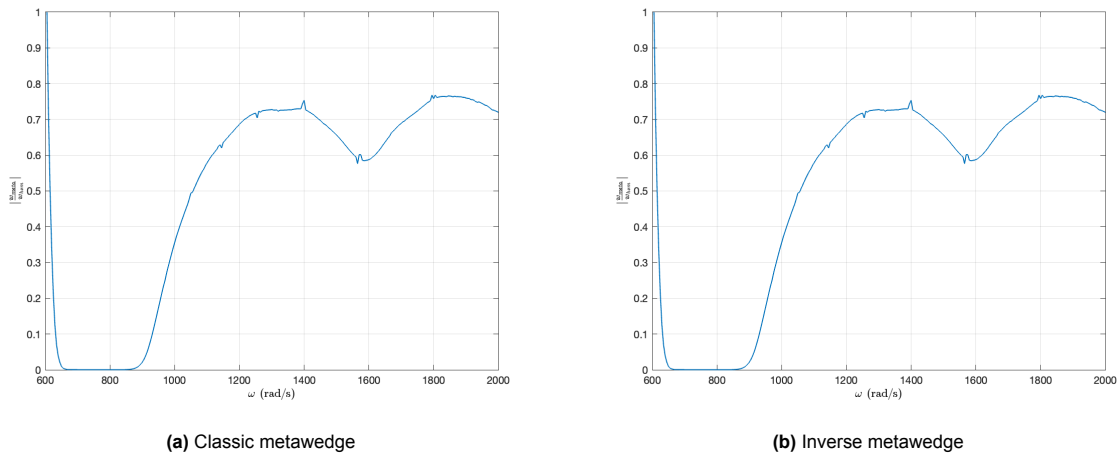


Figure 3.14: Amplitude ratio taken at $x = 26m$

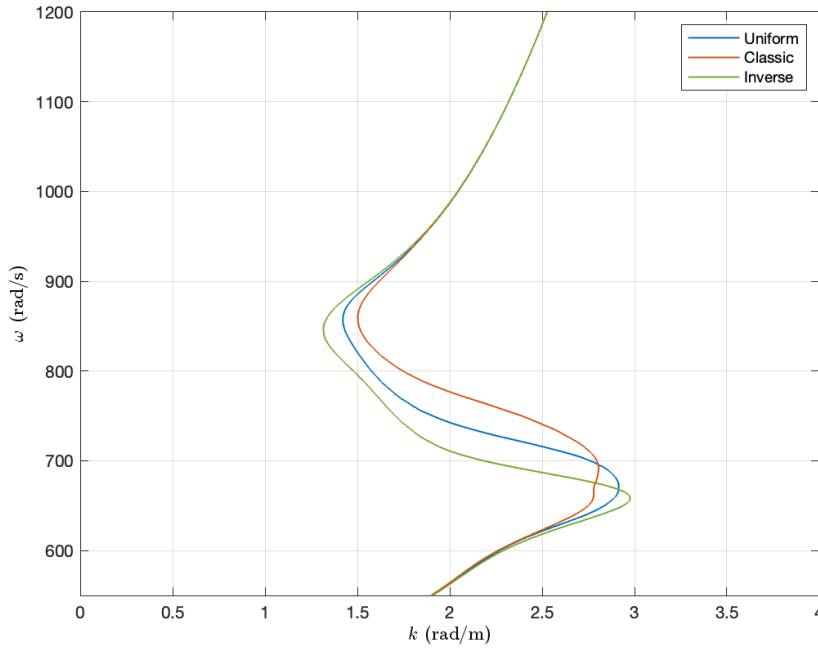


Figure 3.15: Numerically retrieved wavenumbers for the uniform, classic and inverse metawedge

To enhance understanding of the beam's behavior and to validate assertions made by Colombi et al. [8], an analysis of the phase velocity of waves is conducted. Phase velocity, defined as $v_{ph} = \frac{\omega}{k}$, provides insight into the wave propagation speed within the medium. However, using the dispersion characteristics of Figure 3.13 can yield inaccurate results due to inherent noise. To circumvent this issue, the curve is approximated using a smoothing spline, enabling a more reliable calculation. The outcomes of this process, applicable to various configurations, are depicted in Figure 3.15. Subsequent to the approximation, the phase velocity of the uniform metawedge is presented in Figure 3.16. The figure illustrates that specific frequencies experience a reduction in phase velocity while others are accelerated. However, within the uniform configuration, it is not possible to definitively associate these observations with rainbow-trapping or mode-conversion due to the constraints posed by the one-dimensional model. Additionally, it is observed that modifications to the phase velocity occur primarily around the band gap. Beyond this region, the phase velocity generally aligns with that observed in the homogeneous case. When comparing the phase velocity across the classic, and inverse metawedge configurations, a consistent pattern emerges, particularly around the resonance band gap frequencies. In all configurations, the phase velocity is reduced for frequencies below the band gap and increased for frequencies above the band gap.

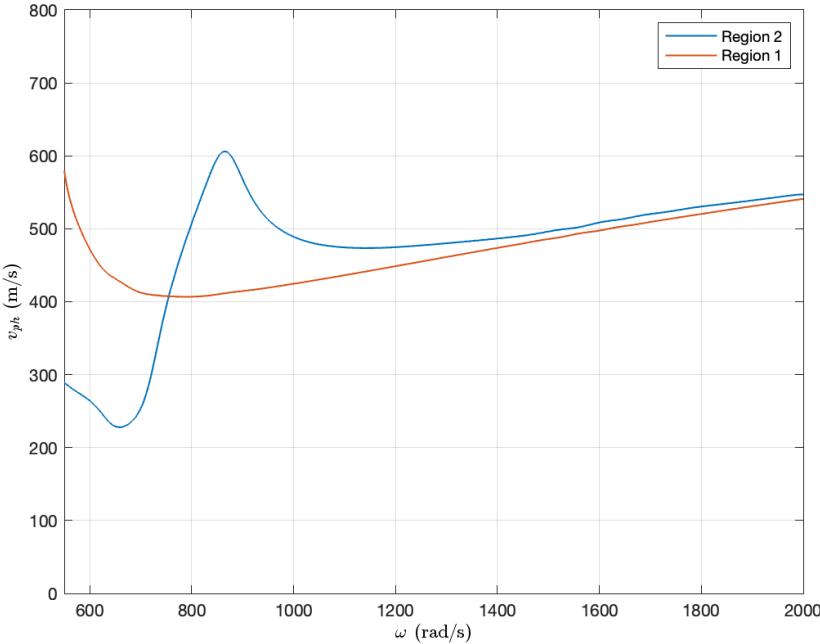
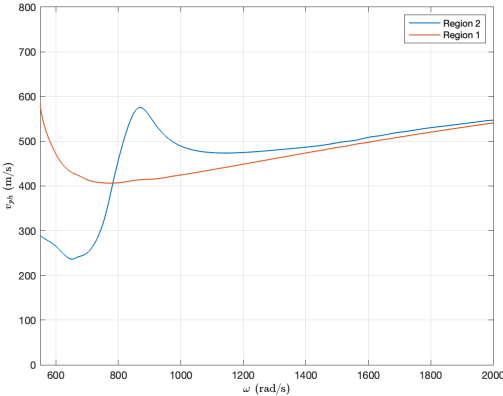
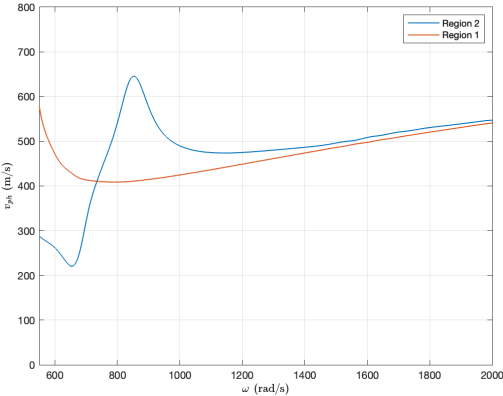


Figure 3.16: Phase velocity of the uniform metawedge, in orange the region before the metawedge, in blue for the metamaterial region



(a) Classic metawedge



(b) Inverse metawedge

Figure 3.17: Phase velocity for the classic and inverse metawedge, in orange the region before the metawedge, in blue for the metamaterial region

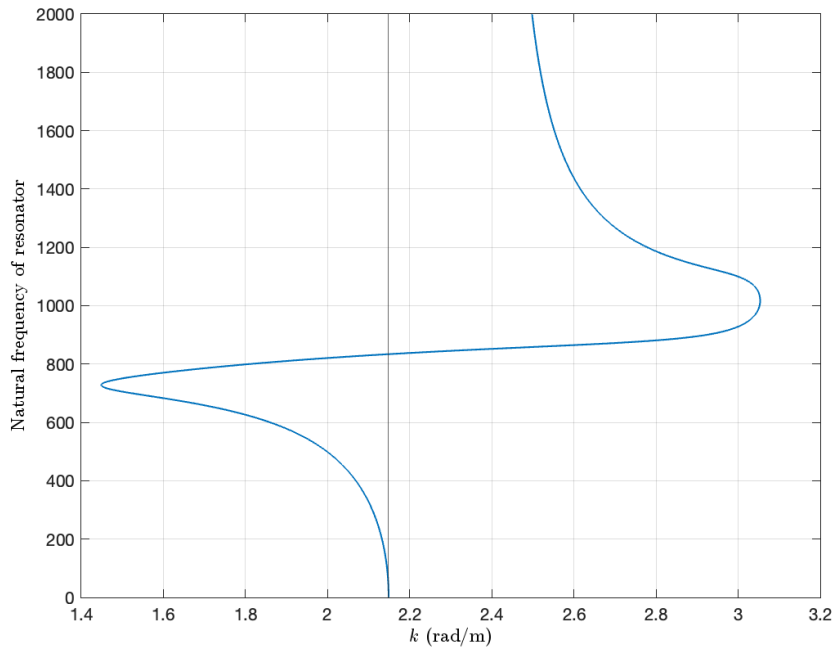


Figure 3.18: Numerically retrieved wavenumbers as a function of resonator frequency, for a harmonic excitation of 900 rad/s

Metamaterial solutions are constructed from unit cells, each possessing unique natural frequencies and dispersive characteristics. In a uniform metawedge configuration, these properties are consistent across all unit cells, whereas in classic and inverse configurations, each unit cell varies in its attributes. Previously, dispersive properties were derived using a wavenumber transform across the entire metamaterial region, yielding a single wavenumber representative of the collective region. However, this approach does not account for the distinct dispersive characteristics attributable to individual unit cells. Given the disproportionate relationship between the wavelengths and the unit cells' length, applying a wavenumber transform to individual cells produces imprecise outcomes. To circumvent this limitation and accurately analyze the classic and inverse metawedge configurations, an alternative methodology is employed. The analysis adopts the Floquet approach to extract wavenumbers for each unit cell, treating them as if part of an infinite system. This strategy is based on the observation that the infinite system serves as an apt approximation for the finite system's behavior. Consequently, a curve is constructed, mapping wavenumbers not against the excitation frequency but rather to the resonators' resonance frequencies within each unit cell. This analysis is conducted for a fixed excitation frequency of 900 rad/s, with results illustrated in Figure 3.18.

Interpreting this Figure necessitates understanding the wave's interaction with the metawedge. For the inverse metawedge, the wave initially aligns with the wavenumber associated with the homogeneous case (indicated by the grey vertical line in the figure) and progresses through resonators with incrementally varying natural frequencies. This gradual change compels the wave to adapt, following the curve upwards and experiencing a reduction in wavenumber, thereby extending its wavelength. This adaptation continues until the wave encounters the band gap at the resonator frequency matching the excitation frequency, here 900 rad/s, with the band gap conceptually spanning from 800 to 1000 rad/s. Conversely, in the classic metawedge scenario, the wave first interacts with the resonator possessing the highest natural frequency. As it traverses the metawedge, the wave's wavenumber increases, leading to a decrease in wavelength. This nuanced understanding of wave behavior in relation to the classic and inverse metawedge configurations elucidates the intricate dynamics governing wave propagation through metamaterials, highlighting the distinct mechanisms of wave manipulation inherent to each design.

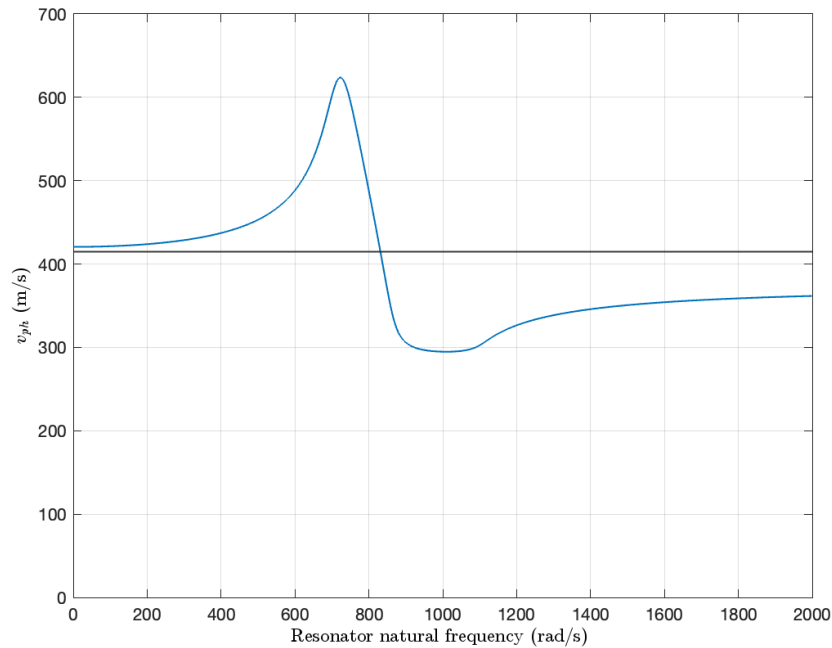


Figure 3.19: Phase velocity as function of resonator frequency at a excitation frequency of 900 rad/s, in grey the phase velocity in the case without resonators

Using the finding from Figure 3.18 the phase velocity can be calculated for a single excitation frequency of 900 rad/s, with the findings presented in Figure 3.19. This figure, constructed similarly to Figure 3.18 but with a focus on phase velocity, offers insights into how wave speed varies across different resonator frequencies within the metawedge. In scenarios where a wave encounters the metawedge beginning at the lowest natural frequency, a clear acceleration is observed as it progresses towards the band gap. Similarly, when the wave initiation point is at the highest natural frequency resonator of the metawedge, a deceleration is noted up to the point of reaching the resonator aligned with the wave frequency. These findings align with expectations, where the classic metawedge configuration shows a slowing down of waves, while the inverse metawedge accelerates them. Despite being a one-dimensional model which cannot simulate wave-mode conversion, an increase in phase velocity is still observed. This suggests that the model can capture the behavior of both configurations to some extent. From the perspective of the receiver similar levels of attenuation are noted in both configurations.

3.5. Summary

This chapter has meticulously explored the dynamic properties of metamaterial configurations, employing both numerical and analytical models to understand their wave propagation characteristics. A pivotal finding from this investigation is the excellent agreement between the numerical model's predictions and the analytical results. This concordance underscores the robustness of the numerical model in simulating the complex behaviors of metamaterials and validates its utility as a reliable tool for metamaterial research.

Further analysis focusing on the dispersive characteristics and phase velocities within different configurations and have illuminated the significant impact of metamaterials on wave behavior. The study revealed that the classic metawedges induces a decrease in wavelength, while in the case of the inverse metawedge an increase in wavelength was observed. Additionally, the investigation into the dispersive properties of individual unit cells within the metawedge configurations has provided deeper insights into the operational mechanisms of these structures. By reconstructing the wavenumbers associated with each unit cell's natural frequency and analyzing the resultant phase velocities, it was observed that waves decelerate while traversing the classic metawedge and accelerate through the inverse metawedge.

An excellent agreement between literature was observed concerning the phase velocities of the meta-wedge. However the current one-dimensional model's inability to simulate wave mode conversion limits the exploration of this phenomenon, which is pivotal in distinguishing between the two configurations. This limitation points to the necessity for multidimensional modeling in future studies to fully capture the complex wave interactions facilitated by metamaterials. In conclusion, the chapter's findings significantly contribute to the understanding of metamaterials' influence on wave propagation. The demonstrated agreement between numerical and analytical models validates the former as an effective instrument for metamaterial analysis. While revealing the ability to manipulate the phase velocity of waves by metamaterials, the study also identifies the need for enhanced modeling techniques to uncover the full extent of metamaterial capabilities, particularly for the mode conversion mechanism. The insights gained lay a foundation for further research aimed at exploiting metamaterial properties for innovative wave control and manipulation applications.

4

Numerical study of metamaterials on a homogeneous half-space

This chapter introduces a two-and-a-half dimensional (2.5D) model. This model is composed of a 2D half-space onto which single degree of freedom resonators are mounted on the surface. Functionally, this setup approximates a three-dimensional (3D) model subjected to a line load, leading to the anticipation of wave propagation directed exclusively perpendicular towards the mitigation measure. Consequently, this model aligns more closely with practical applications intended for the assessment of mitigation strategies. Using insights acquired from preceding chapters, a mitigation approach employing single degree of freedom resonators will be constructed. The objectives of this chapter include the design of a mitigation measure and the understanding of its underlying mechanisms.

4.1. Adopted numerical model

The utilization of a three-dimensional model significantly enhances the capacity to simulate soil behavior accurately, offering a representation that more closely mirrors real-world conditions. This advancement is crucial for evaluating the effectiveness of metawedge configurations against train-induced excitation's. The specific model employed in this research is named FEMIX developed by Barbosa et al [21], the software is characterized as a 2.5D plane-strain model. This model simulates three-dimensional wave propagation under the assumption of a uniform cross-section in one direction—aligned with the railway track for the purposes of this study. A schematic representation of this model, highlighting the positioning of mitigation measures within a homogeneously modeled soil half-space, is depicted in Figure 4.1. The train track's presence is omitted based on the assumption of its negligible impact on the analytical outcomes.

The analytical model integrates boundary-element (BEM) and finite-element (FEM) methods, employing the thin-layer method (TLM) for the formulation of the fundamental solutions. This dual approach allows for the modeling of soil dynamics using boundary elements while representing mitigation measures through finite elements. To effectively simulate infinite soil half-spaces, perfectly matched layers (PMLs) are coupled to the boundary elements, ensuring a comprehensive simulation of wave propagation through soil. The system's response is computed within the space-wavenumber-frequency domain, with wavenumbers k_y oriented in the y-direction. Deriving solutions in the space-frequency domain necessitates the application of an inverse Fourier transform over all wavenumbers, effectively summing the outputs of various two-dimensional models to represent a three-dimensional wave propagation scenario. This approach is feasible due to the uniformity of the model's cross-section and properties along the y-direction. A benefit of such a method is the option to exclude wavenumbers from consideration, thereby simplifying the complexity from a three-dimensional to a two-dimensional wave propagation model. This simplification conceptualizes the problem as akin to a two-dimensional half-space subjected to a line load perpendicular to the plane of analysis. The preliminary utilization of a two-dimensional model offers significant computational advantages, notably reducing the time required

for simulations when compared to fully three-dimensional models.

Employing a two-dimensional model in the initial stages of analysis facilitates a rapid assessment of the chosen mitigation measure's properties, allowing for prompt adjustments as necessary. This model proves particularly useful in elucidating the dispersive properties of metamaterials and pinpointing the locations of bandgaps. Subsequently, the analysis can progress to a 3D model to evaluate the mitigation measure's efficacy against wave incidences from various angles, extending beyond those perpendicular to the mitigation measure. This staged approach ensures both efficiency and thoroughness in the exploration of metamaterial performance and wave interaction dynamics. In this modeling approach, soil is depicted using boundary element (BE) techniques, necessitating discretization exclusively at the boundaries. However, the implementation of the thin-layer method (TLM) for resolving the system's response mandates a detailed specification of elements within each layer. This distinction divides the soil model into upper and lower half-spaces, even within a homogeneous soil context, the upper half-space is modeled via the TLM. The method divides the soil's vertical extent into quadratic thin layers, each with a thickness of 0.10 m [3]. The mitigation measures are modelled using finite elements, specifically 2.5D quadrilateral elements with linear isotropic material properties. The finite element domain is discretized to ensure a minimum of 10 elements per shear wavelength, a criterion established to maintain accuracy across simulations, as noted by Coulier et al. [12]. This ensures uniformity in discretization across both the x- and z-directions, standardizing all elements to a square configuration. Given the model's formulation as a superposition of various wavenumbers k_y , a discrete representation of these wavenumbers becomes crucial. This discretization employs a dimensionless wavenumber approach, $\bar{k}_y = k_y c_s / \omega$, facilitating accurate results, particularly in far-field scenarios. As per the findings of Francois et al. [16], a maximum dimensionless wavenumber of $\bar{k}_y = 3$ suffices for accurately modeling far-field displacements. The discretization of \bar{k}_y is conducted over 300 samples ranging from $\bar{k}_y = 0$ to $\bar{k}_y = 3$, ensuring thorough and accurate analytical results.

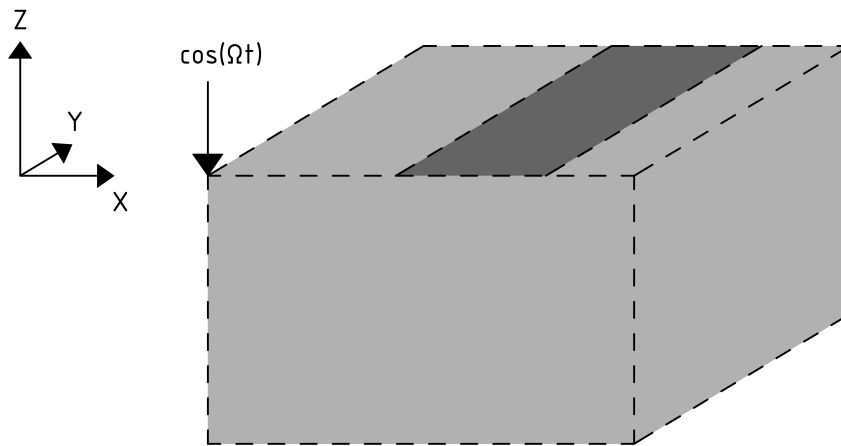


Figure 4.1: Convention of coordinate system as used in FEMIX, in which the y-direction is assumed homogeneous in geometry and properties, In dark grey the location of mitigation measures

This chapter delves into the physics underpinning the metawedge and evaluates its operational effectiveness. A similar approach is used to Chapter 2 and 3 where the metamaterials are implemented as single degree of freedom resonators. Three configurations will be investigated the uniform, classic and inverse metawedge, as shown in Figure 2.4. In the classic metawedge configuration, an incident wave encounters the metawedge at the side where unit cells possess the highest natural frequencies. As the

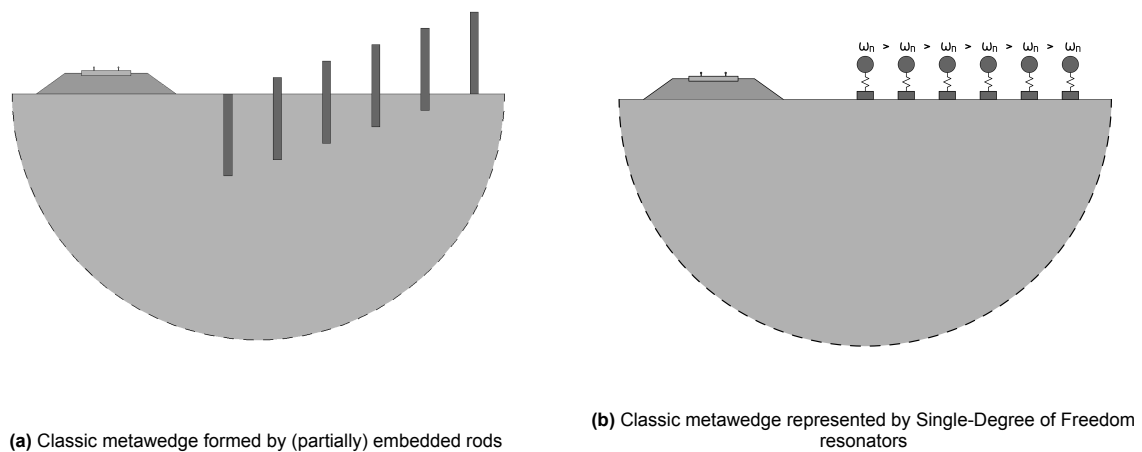


Figure 4.2: Adopted metawedge model

wave propagates through the metawedge, it traverses unit cells with progressively decreasing natural frequencies. Conversely, the inverse metawedge introduces the wave to the resonator with the lowest natural frequency first, proceeding through unit cells with incrementally increasing natural frequencies. Should the unit cells be envisioned as a half-space with partially embedded rods—a concept explored by Bracci et al [1].—the classic wedge would begin with a rod fully embedded in the soil, transitioning to rods that are increasingly exposed above the surface. This gradient creates the physical “wedge” appearance, as illustrated in Figure 4.2 (a). In the context of this study, the metawedge is conceptualized using Single-Degree of Freedom (SDOF) resonators, with the sequence of natural frequencies across the unit cells defining the metawedge’s categorization. This arrangement for the classic metawedge is depicted in Figure 4.2 (b).

In the implementation within FEMIX, the soil is simulated utilizing boundary elements (BEM), and the resonators are modeled through finite elements (FEM). The resonators’ mass is depicted by dual square elements, standardized in size across all resonators, allowing mass adjustment via material parameter alterations. This approach allows the control of natural frequency of the unit cell through the material properties, which is a favorable strategy to ensure fast calculations using FEMIX. To ensure these elements function as rigid point masses, a substantially high Young’s modulus is applied, minimizing element deformation. The springs are modelled using spring elements, characterized by their spring stiffness (k) and damping coefficient (c). These elements are designed to operate exclusively in the z -direction, aligning the resonators’ movement with this constraint. Consequently, the resonators’ motion is predominantly governed by the vertical components of Rayleigh waves. Each resonator rests atop a foundation, mirroring the mass elements in size, but engineered with parameters ensuring minimal mass and elevated Young’s modulus. This configuration negates any potential impact of the foundation on the analytical outcomes, while simultaneously circumventing singularities that could arise from forces applied to small surface areas. Positioning the foundation on top of the soil, rather than embedding it, offers practical advantages including the elimination of the need for excavation or extensive ground work, facilitating easier implementation of the metawedge. Additionally, from a computational standpoint, this approach maintains the integrity of the boundary elements, thereby enhancing computational efficiency. This configuration of the model is illustrated in Figure 4.3.

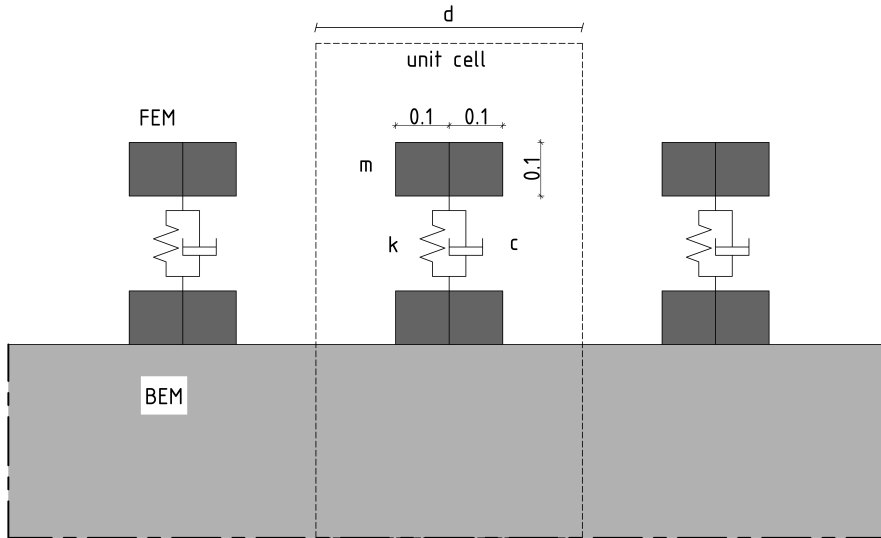


Figure 4.3: Convention of coordinate system as used in FEMIX, in which the y-direction is assumed homogeneous in geometry and properties, In dark grey the location of mitigation measures

4.1.1. Verification of numerical model

Given the manual discretization required when generating an input file for FEMIX, there is a potential for errors to arise. To mitigate this risk and ensure the accuracy of the script implementation, a benchmarking process against an established literature case is conducted. While the specific meta-material model proposed for investigation in a 2.5D framework has not been previously examined, the benchmarking will focus on a different, yet relevant, mitigation measure for comparative purposes. The selection of a stiff trench embedded in homogeneous soil as the benchmark model is driven by the prevalence of trenches as common mitigation measures and their documented effectiveness. This comparison aims to establish a reference point for evaluating the performance of the proposed meta-material model against established mitigation strategies. The benchmark study chosen for this purpose is that of Hoorickx et al.[28], which assesses the impact of a stiff wall barrier within a 2.5D modeling context.

The findings from Hoorickx et al. are illustrated in Figure 4.4 and 4.5, providing a comprehensive overview of the barrier's influence on wave propagation. Figure 4.4 displays the real part of the vertical displacement for both the homogeneous soil scenario and the one modified by the inclusion of a stiff trench, capturing a momentary glimpse of the steady-state solution. Subsequently, Figure 4.5(a) presents the insertion loss, quantifying the mitigation's efficacy by contrasting the homogeneous case against the mitigated scenario. The methodology for calculating insertion loss is delineated in the work of Coulier et al.[13], offering a structured approach to assessing the comparative reduction in vibration transmission attributable to the mitigation measure.

$$IL_i(x, z, \omega) = 20 \log_{10} \frac{|U_i^{\text{ref}}(x, z, \omega)|}{|U_i(x, z, \omega)|}, \quad i \in \{x, y, z\} \quad (4.1)$$

Figure 4.5(b) illustrates the insertion loss as a function of both frequency and wavenumber, facilitating a nuanced analysis of the mitigation measure's effectiveness across different wave propagation scenarios. This representation enables the establishment of a correlation between the wavenumber k_y and the incidence angle θ , as detailed in the study by Van Hoorickx et al [28]. Through this approach, the concept of longitudinal slowness is introduced and defined by the equation:

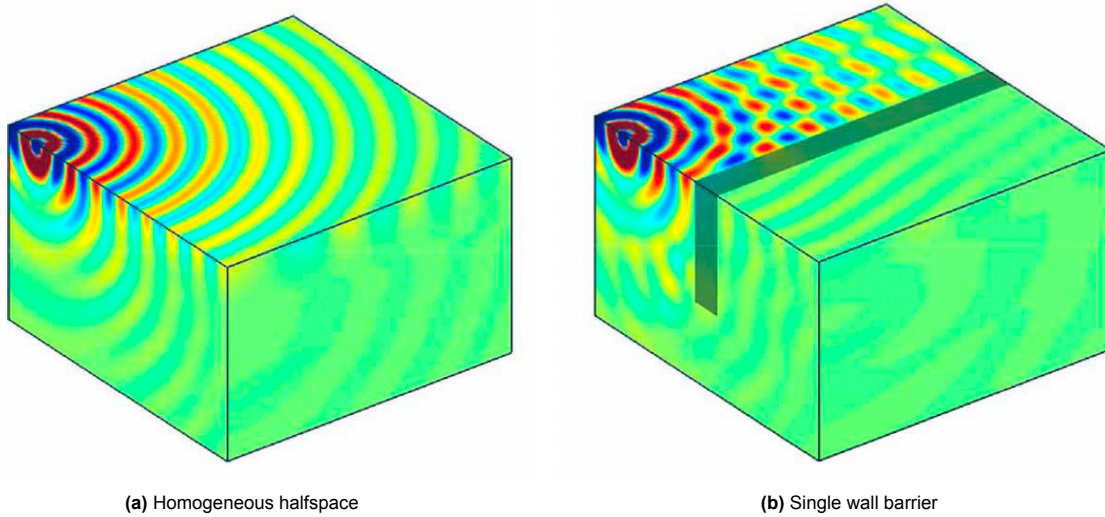


Figure 4.4: Real part of the vertical displacement at 60 Hz, reference: [28]

$$K_y = \frac{k_y}{\omega} \quad (4.2)$$

Here, longitudinal slowness (K_y) serves as a critical parameter for inferring the incidence angle of wave propagation relative to the mitigation measure. The incidence angle itself is determined through the calculation:

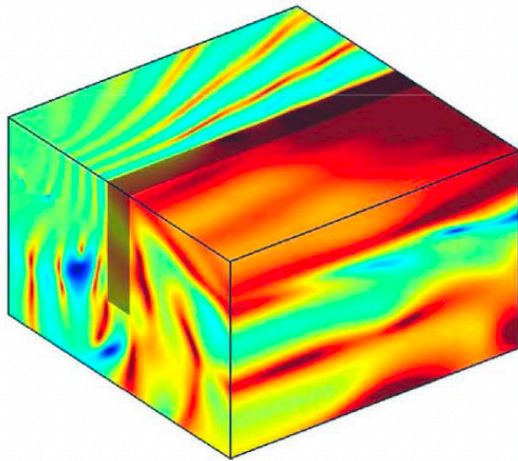
$$\theta = \sin^{-1} \left(\frac{K_y}{K_R} \right) \quad (4.3)$$

where K_R represents the Rayleigh wave slowness. This methodology provides a systematic means of linking specific wavenumbers with their corresponding incidence angles, offering insight into the spatial distribution and interaction of waves with the stiff trench. Such an analysis is instrumental in comprehensively understanding the dynamics at play and assessing the stiff trench's efficacy as a mitigation strategy against surface waves, drawing parallels to the anticipated performance of the metawedge. The outcomes generated through the application of FEMIX by the author are presented in Figure 4.6 and 4.7. Upon comparing these results with those documented by Van Hoorickx et al. [28], it is evident that there is an excellent agreement between the two sets of findings.

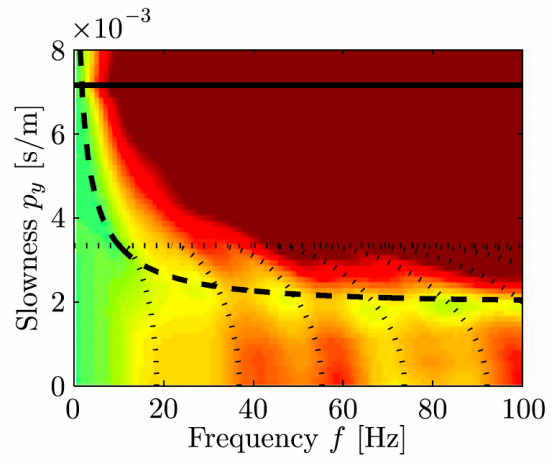
4.2. Identification of band gaps

The investigation starts with an analysis of the coupled system comprising of resonators and soil. Drawing from insights acquired in Chapters 2 and 3, it is established that band gaps arise through mechanisms such as local resonance and Bragg scattering. Consequently, band gaps are anticipated around the natural frequency of the unit cell, distinct from the resonators' natural frequency due to the coupling effect with the soil, rendering its precise location initially indeterminate. Predicting the band gap induced by Bragg's scattering is relatively straightforward, attributed to its dependency on the resonators' spacing, in this study set at 1m. With the soil modeled as homogeneous, the Rayleigh wave's dispersion curve is linear, implying a uniform group and phase velocity for all frequencies. In this model, this velocity is approximately at $c_R \approx 183$ m/s. This allows for the calculation of the specific frequency at which the wavelength equals twice the spacing between the resonators, facilitating half a wavelength's fit between them, calculated as $f = \frac{c}{2d}$, yielding $f = 91.5$ Hz.

The band gap's precise location is determined numerically by comparing the system's response with and without mitigation measures through the insertion loss parameter. This parameter translates the band gap's impact into decibels (dB), a measure commonly utilized in literature for quantifying vibration

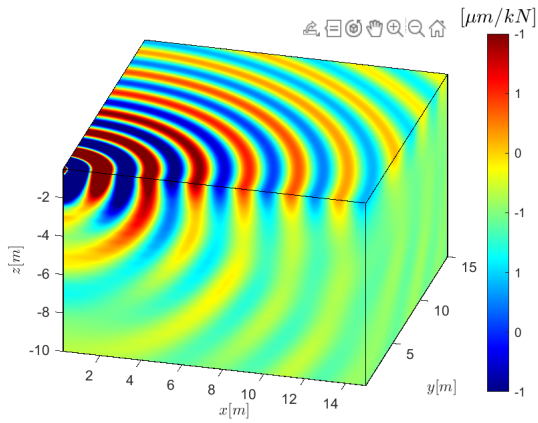


(a) Vertical insertion loss

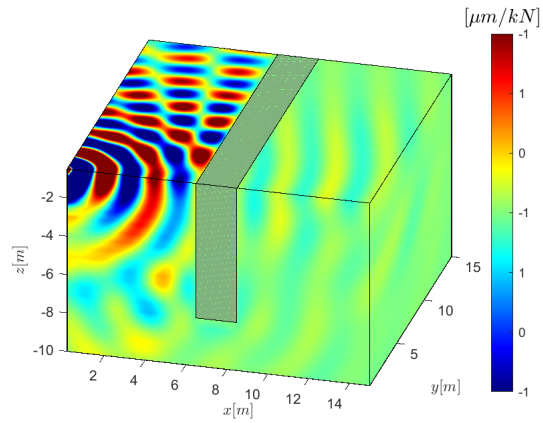


(b) Insertion loss as function of frequency and longitudinal slowness

Figure 4.5: Insertion loss of the vertical displacement, reference: [28]

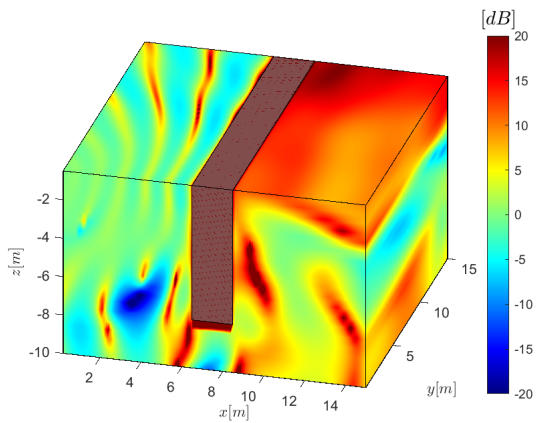


(a) Homogeneous halfspace

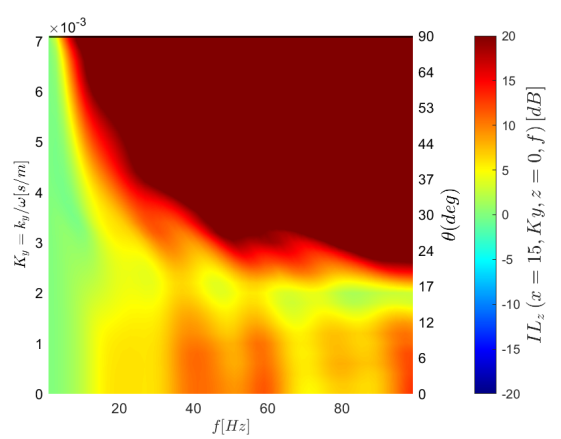


(b) Single wall barrier

Figure 4.6: Real part of the vertical displacement at 60 Hz



(a) Vertical insertion loss



(b) Insertion loss as function of frequency and longitudinal slowness

Figure 4.7: Insertion loss of the vertical displacement

reduction. While the logarithmic scale of dB may not directly correlate with human vibration perception, its widespread use in academic studies warrants its application here. The system responses are measured at a specific point ($x = 90.1, y = 0, z = 0$), initiating the analysis with the uniform metawedge configuration. The soil parameters used in this study are outlined in Table 4.1.

Table 4.1: Soil parameters

Parameter	Symbol	Value	Unit
Mass density	ρ	2000	kg/m
Shear modulus	G	80	MPa
Shear wave speed	c_s	200	m/s
Compressional wave speed	c_p	346.4	m/s
Rayleigh wave speed	c_R	183.9	m/s
Poisson ration	ν	0.25	–
Damping ratio	ζ	1e-2	–

This investigation will concentrate on two specific excitation frequencies corresponding to different types of trains: one representative of passenger trains and the other of freight trains. The excitation frequencies generated by trains are significantly influenced by the soil type. In sandy soils typical of the Netherlands, freight trains are known to excite frequencies within the 10 to 15 Hz range, whereas passenger trains, particularly intercity trains, tend to excite frequencies in the 20-30 Hz range. Given the broader context of this study, the emphasis will be placed on the lower frequencies excited by freight trains, as the vibrations they induce are often deemed the most disruptive. For comparative purposes, results pertaining to the 25 Hz case, representative of passenger train frequencies, are briefly presented. Results for other frequencies exhibit similar patterns to those discussed in this chapter. The specifications for the uniform, classic, and inverse metawedge configurations are detailed in Table 4.2, 4.3, and 4.4, respectively. Throughout this study, the mass of the resonators is maintained consistently, while variations in their natural frequencies are achieved by adjusting the spring stiffness (k). The natural frequency of the resonators is calculated for an uncoupled system with $\omega_n = \sqrt{k/m}$. The selected mass for the resonators is 300 kg, approximately equivalent to a steel sphere with a diameter of 20 cm. Further examination of the impact of various parameters, including mass, will be undertaken in subsequent sections of the study.

Table 4.2: Model parameters of the uniform metawedge

Parameter	Symbol	Value	Unit
Start of metawedge	x_1	50	m
Number of resonators	–	20	–
Natural frequency first resonator	ω_1	13.5	Hz
Natural frequency last resonator	ω_{20}	13.5	–
Metamaterial Mass	m	300	kg
Metamaterial damping ratio	ζ	2.5e-2	–
Metamaterial spacing	d	1	m

Table 4.3: Model parameters of the classic metawedge

Parameter	Symbol	Value	Unit
Start of metawedge	x_1	50	m
Number of resonators	–	20	–
Natural frequency first resonator	ω_1	15	Hz
Natural frequency last resonator	ω_{20}	10	–
Metamaterial Mass	m	300	kg
Metamaterial damping ratio	ζ	2.5e-2	–
Metamaterial spacing	d	1	m

Table 4.4: Model parameters of the inverse metawedge

Parameter	Symbol	Value	Unit
Start of metawedge	x_1	50	m
Number of resonators	—	20	—
Natural frequency first resonator	ω_1	10	Hz
Natural frequency last resonator	ω_{20}	15	—
Metamaterial Mass	m	300	kg
Metamaterial damping ratio	ζ	2.5e-2	—
Metamaterial spacing	d	1	m

The analysis related to the identification of band gaps within metawedge configurations yields insightful results, as depicted in Figure 4.8. Panel (a) illustrates the outcomes for a uniform metawedge defined by parameters in Table 4.2, while panel (b) showcases a uniform metawedge with a resonator mass of 100 kg and a natural frequency set at 25.5 Hz, keeping all other parameters consistent with those listed in Table 4.2. Across both figures, four distinct band gaps are observed.

The first band gap is attributed to local resonance, evidenced by its centralization around the resonators' natural frequency. Consequently, this band gap experiences a shift in panel (b) compared to panel (a). The second band gap, positioned at 91.5 Hz, aligns with the previously calculated frequency and is attributed to Bragg scattering. However, this band gap is less effective than the one created by local resonance. This observation echoes findings from Chapter 3, noting a diminished efficacy of the Bragg band gap¹ upon transitioning to local resonance metamaterials. A third band gap emerges at 120 Hz, and its origin is less straightforward, as it does not directly correlate with the natural frequency of the resonators or the spacing between them. This band gap is attributed to the coupled system of resonators and soil, which possesses an infinite number of resonance modes. It is important to note, however, that this secondary resonance mode is much less effective than the primary resonance mode. The fourth band gap is identified at 183 Hz, correlating with an integer multiple of the 91.5 Hz band gap, indicating a scenario where an entire wavelength is accommodated between resonators. Despite its higher insertion loss, leveraging this band gap for practical applications, especially within the targeted 10-15 Hz frequency range, poses challenges. Designing for such a band gap would necessitate resonator spacing of approximately 14 meters, impractical given spatial constraints near railway tracks. Consequently, this study will prioritize the band gap generated by local resonance. This band gap's tunability to desired frequency ranges offers a flexible design approach, advantageous for addressing train-induced vibrations which may vary significantly with soil conditions.

Upon closely examining the local resonance band gap in Figure 4.9, it is observed that the peak coincides with 13.5 Hz, aligning with the resonator's natural frequency when conceptualized as an uncoupled single-degree of freedom system. However, for band gaps aimed at higher frequencies, a slight downward shift from the resonator's natural frequency is noted, highlighting the effects of a coupled system. Additionally, the band gap's relatively narrow width is highlighted, primarily because all resonators are synchronized to focus on a singular frequency. Given the broad frequency spectrum of train-induced vibrations, a narrow band gap may not adequately address the diverse range of frequencies involved. To overcome this limitation and potentially expand the band gap's width, two approaches are considered. The first involves augmenting the damping ratio, a topic explored in subsequent sections of this study. The second approach entails distributing the natural frequencies of the resonators across a wider spectrum, akin to the strategy employed in both classic and inverse metawedge designs, where the natural frequencies span from 10-15 Hz. The outcomes of implementing these strategies are detailed in Figure 4.10.

¹The choice to model the foundation with almost no mass, aiming to isolate the effects of local resonance, might affect the perceived strength of this band gap. In practical applications, the foundation will possess significant mass, which is expected to enhance the band gap's effectiveness.

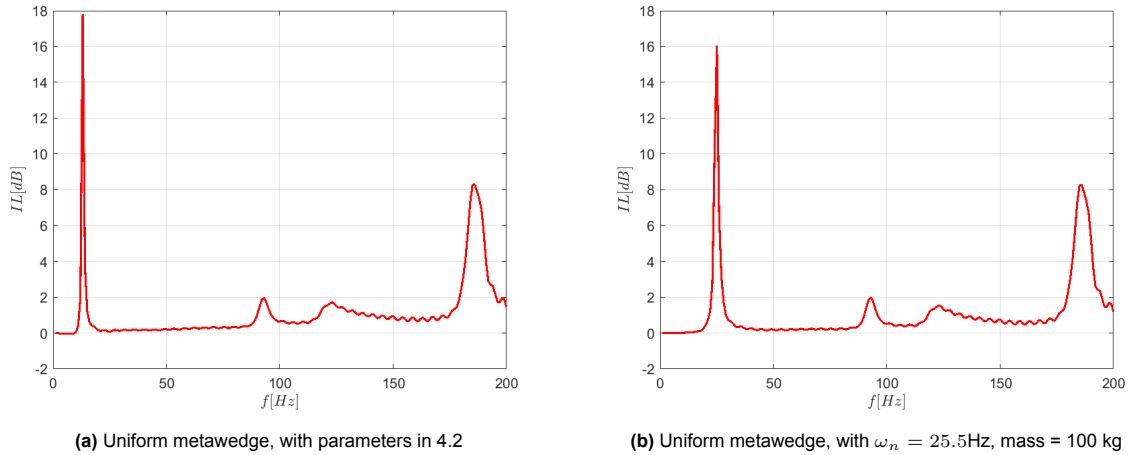


Figure 4.8: Vertical insertion loss, for two different configurations of the uniform metawedge

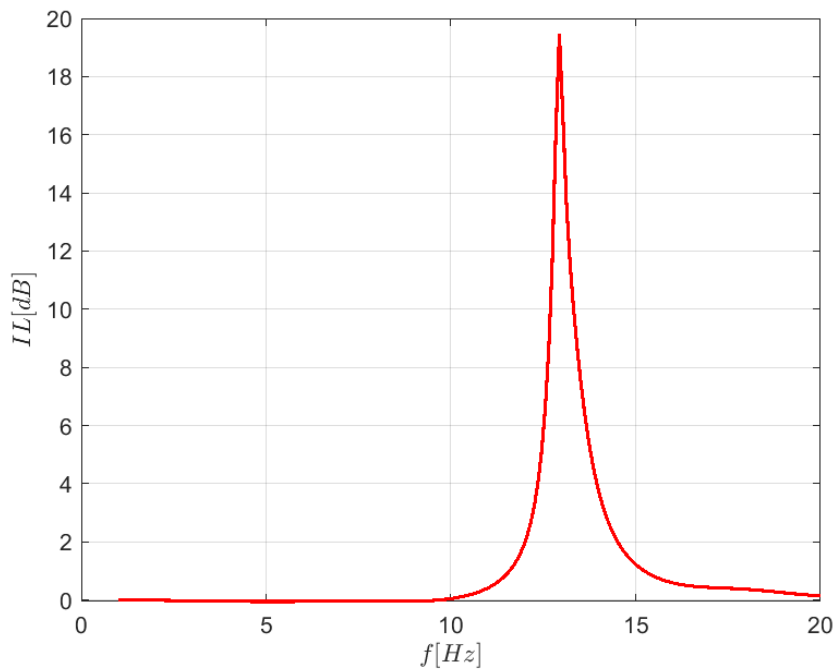


Figure 4.9: Band gap due to local resonance for the uniform metawedge

Upon comparing the results with the band gap produced by the uniform metawedge, a significant broadening of the band gap is observed, reflecting the range that mirrors the resonance frequencies of the resonators. This expansion, while advantageous in terms of frequency coverage, does compromise the band gap's overall efficiency. Nevertheless, achieving a band gap within the range of 1.5 to 4 dB remains considerably effective, offering substantial attenuation of train-induced vibrations. The prospect of enhancing the band gap's efficiency through the inclusion of a higher mass resonator is explored further in subsequent analyses. For the purposes of this preliminary investigation, the resonator mass is maintained at 300 kg, deemed both practical and sufficiently efficacious for the intended application. Interestingly, the analysis reveals negligible differences between the band gaps generated by the classic and inverse metawedge configurations. This outcome is intriguing, given the fundamentally distinct wave manipulation behaviors characteristic of each configuration. However, this finding presents an advantageous flexibility, enabling engineers to select the most appropriate metawedge configuration

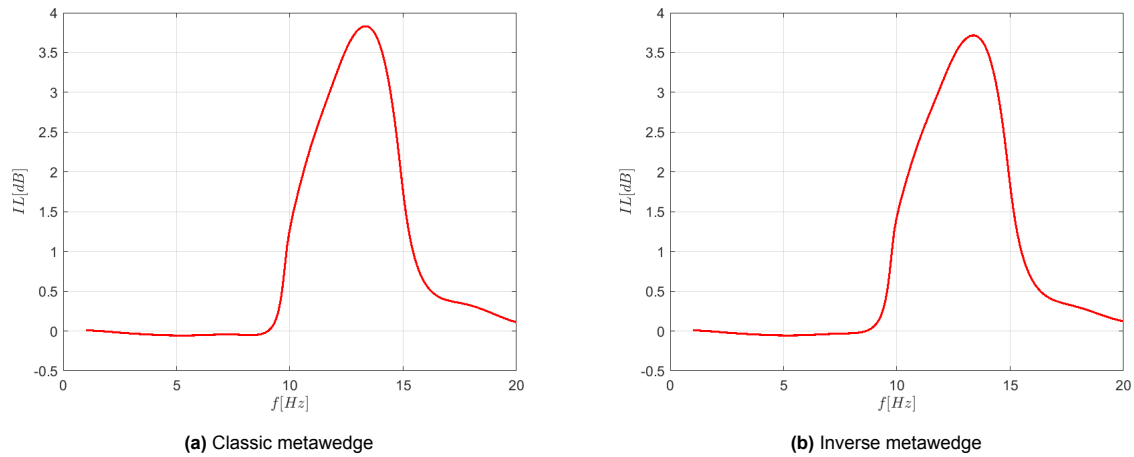


Figure 4.10: Vertical insertion loss for different metawedge configurations

for specific project requirements without compromising on the efficacy of vibration attenuation.

The distinct wave manipulation behaviors exhibited by the classic and inverse metawedge configurations are notably different, as highlighted in the study by Colombi et al. [8]. The phenomenon observed in the classic metawedge, termed "elastic rainbow trapping", involves the deceleration of waves within the metawedge until a point is reached where it becomes "trapped" inside the metawedge, resulting in the waves being redirected back towards the source [8]. Conversely, the inverse metawedge effect, known as "wave-mode conversion," is characterized by the hybridization of Rayleigh waves with the shear wave line, leading to the conversion of Rayleigh waves into shear waves that then propagate into the soil. While these descriptions effectively capture the outcomes associated with each metawedge type, they do not delve into the mechanisms enabling such wave manipulation. This study aims to explore and elucidate the underlying principles governing these effects, striving to provide a comprehensive understanding of how metawedge configurations can be optimized to achieve specific wave manipulation outcomes.

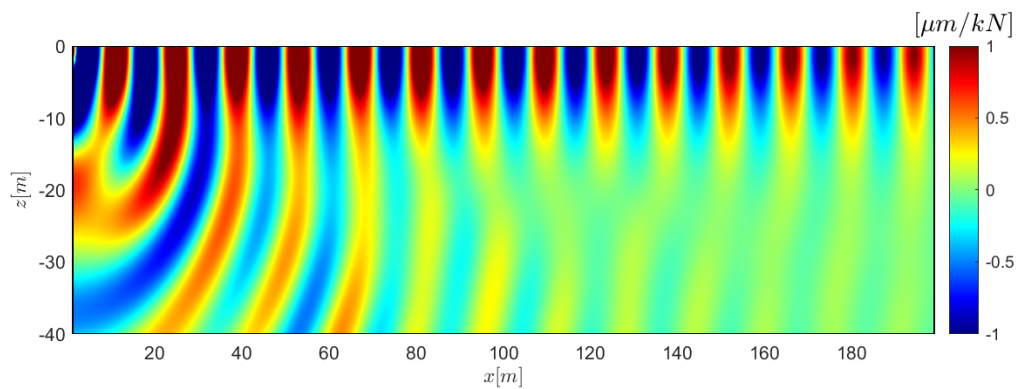


Figure 4.11: Real part of vertical displacement for the homogeneous case at $F = 13$ Hz

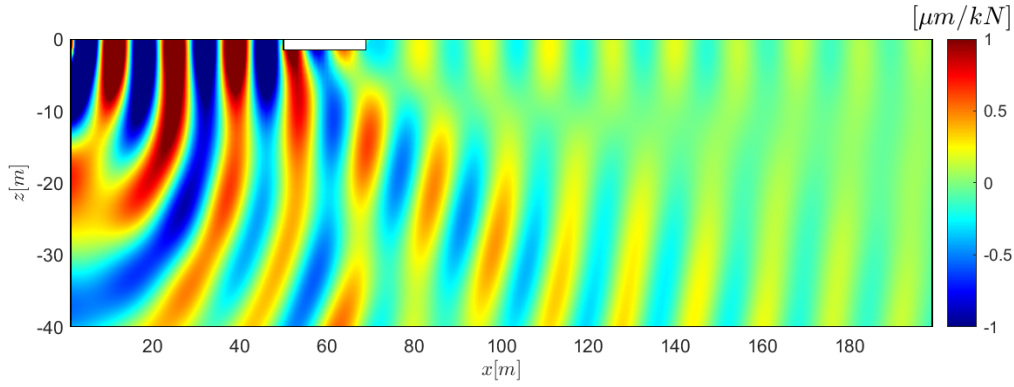


Figure 4.12: Real part of vertical displacement for the uniform metawedge at $F = 13$ Hz

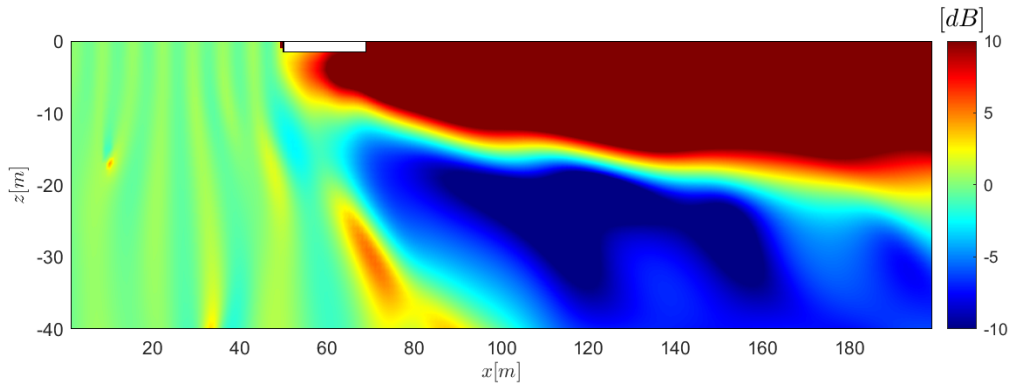


Figure 4.13: Vertical insertion loss for the uniform metawedge at $F = 13$ Hz

Figure 4.11 illustrates the response of a homogeneous half-space subjected to a unit excitation at 13 Hz. Subsequent figures, 4.12, 4.16, and 4.19, display the soil's response incorporating uniform, classic, and inverse metawedge configurations, respectively. These responses reveal the wave-mode conversion effect, notably converting a significant portion of energy into shear waves, aligning with expectations given the observed insertion loss of nearly 20 decibels in this band gap. The effectiveness of this energy conversion is further evidenced through the insertion loss parameter depicted in Figure 4.13, indicating substantial attenuation of Rayleigh waves at the surface. The energy redirection into shear waves that penetrate the substrate underscores the metawedge's capability in manipulating wave propagation. However, it is crucial to note the potential for stiff layers beneath the metawedge to partially reflect waves back to the surface. This phenomenon represents a consideration in the design process of metawedge applications, necessitating thorough assessment for real-world projects.

Moreover, a notable degree of wave reflection directed back towards the source is observed, although its intensity is not markedly pronounced. Within the resonators, dampers facilitate a portion of the energy dissipation, categorizing the principal mechanisms of energy dissipation into three distinct types: mode conversion, reflection, and absorption. In order to conduct a comprehensive comparative analysis among various metawedge configurations, the following methodologies are suggested. The impact of mode conversion is assessable through the visual examination of two-dimensional insertion loss plots, exemplified by Figure 4.13. Reflection quantification can similarly be pursued through analysis of insertion loss plots, although these measurements may be less definitive due to inherent transient effects associated with the presence of the metawedge. Absorption evaluation is determined by calculating the average power absorbed by the dash pots over a single cycle. The instantaneous power $P(t)$ can be described by the damping ratio and the relative velocity of the mass \dot{x}_r as:

$$P(t) = c\dot{x}_r^2 = c(-\Omega x_0 \sin(\Omega t + \phi) + \Omega y_0 \sin(\Omega t + \theta))^2 \quad (4.4)$$

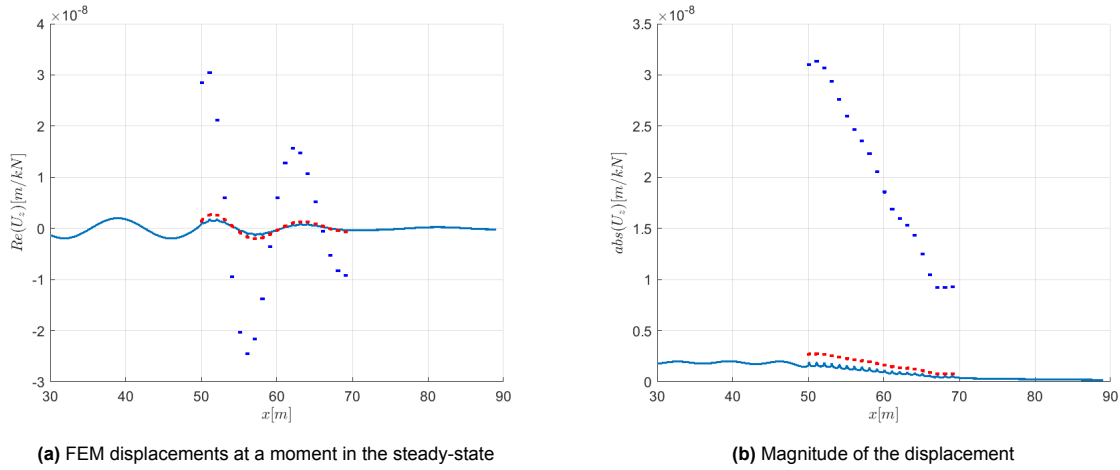


Figure 4.14: Vertical displacement of the resonators for the uniform metawedge, in blue the rigid masses, in red the foundation

In which $x(t)$ is the displacement of the mass relative to an inertial reference frame and $y(t)$ is the displacement of the foundation, which can be described as:

$$x(t) = x_0 \cos(\Omega t + \phi) \quad (4.5)$$

$$y(t) = y_0 \cos(\Omega t + \theta) \quad (4.6)$$

The average power absorbed by the damper over one cycle can then be calculated as:

$$\bar{P} = \frac{c\Omega^2}{2} (x_0^2 + y_0^2 - 2x_0y_0\cos(\phi - \theta)) \quad (4.7)$$

Employing these approaches provides a comprehensive framework for analyzing the interplay between mode conversion, reflection, and absorption in dissipating energy, offering valuable insights into optimizing metawedge design for effective vibration mitigation.

In the case of the uniform metawedge, Figure 4.14 illustrates the resonators' displacement. This figure shows that the resonators' movements are in phase with the ground displacement. The displacement magnitude indicates that the initial resonator contributes most significantly to the system's response, with each subsequent resonator having a diminishing impact. The amplitude of the resonators is observed to be approximately 16 times greater than that of the soil, underscoring the efficiency of the initial resonator in the energy dissipation process and suggesting a point of diminishing returns with the addition of more resonators. Using Equation 4.7, the average power over one period is calculated. This measure is most useful when compared with the average power of other configurations, which will be presented subsequently for a comprehensive analysis.

Shifting focus to the performance of the classic and inverse metawedge, as depicted in Figures 4.16 and 4.19, a direct comparison with the uniform metawedge is challenging due to variations in band gap strengths. A more apt comparison lies between the classic and inverse configurations, revealing markedly different behaviors. The wave-mode conversion in the inverse metawedge is notably pronounced, while in the classic variant, it is less evident but observable. Given the identical band gaps in both classic and inverse metawedges, as shown in Figure 4.10, the distinct behaviors suggest differing mechanisms of energy redirection.

Investigating resonator displacements in Figures 4.18 and 4.21 reveals that in the classic configuration, resonators move in phase up to the point where the resonator's natural frequency aligns with the signal's frequency, subsequently moving out of phase. This phase shift facilitates energy dissipation. This behavior implies that resonators move in phase when the force frequency is below their natural frequency and out of phase when it exceeds it, as would be expected. The displacement magnitude

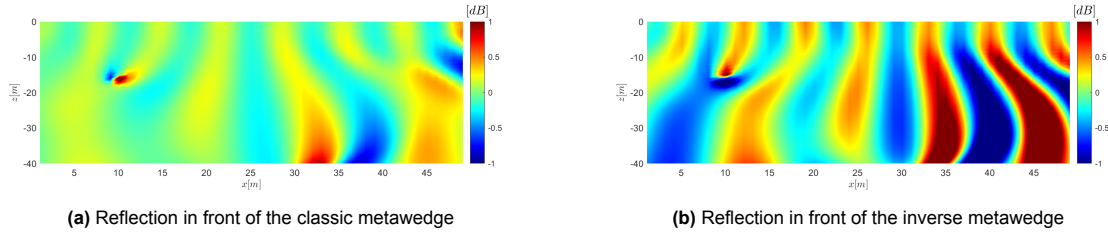


Figure 4.15: Reflection in front of the metawedge

analysis indicates that for the classic metawedge, resonator displacements are approximately 18 times greater than the soil's, whereas for the inverse metawedge, this ratio is about 11 times. To accurately quantify the absorption, the average power absorbed by the dash pots over one period is calculated using Equation 4.7. This value is most informatively presented as a ratio comparing the different configurations. The results show that the classic metawedge dissipates about 2.2 times more energy than the inverse metawedge. When compared to the uniform metawedge, the classic and inverse configurations absorb approximately 0.3 and 0.7 times as much energy, respectively, indicating that the uniform metawedge is more effective in energy dissipation through damping. This aligns with expectations, as the uniform metawedge generally shows superior performance at a single excitation frequency. However, these results clearly demonstrate that the classic metawedge dissipates more energy than the inverse configuration.

Reflections observed in both the inverse and classic metawedge configurations are detailed in Figure 4.15, offering insights into their differing behaviors. The inverse metawedge demonstrates a higher degree of reflection than the classic case. This higher reflection level aligns with its greater wave-mode conversion capabilities. Despite this, reflections occur in both configurations due to transient effects inherent in the system. The key distinction between the two lies in their primary methods of energy management: the classic metawedge primarily directs energy towards resonators for absorption, whereas the inverse metawedge facilitates more wave-mode conversion, redirecting energy differently.

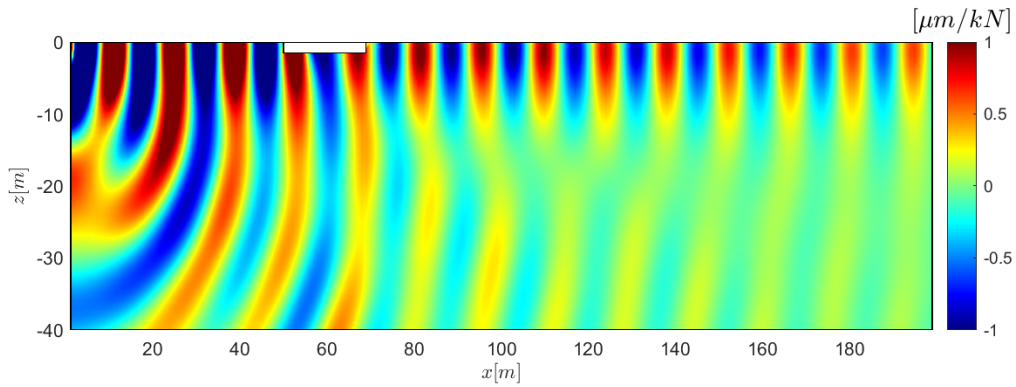


Figure 4.16: Real part of vertical displacement for the classic metawedge at $F = 13$ Hz

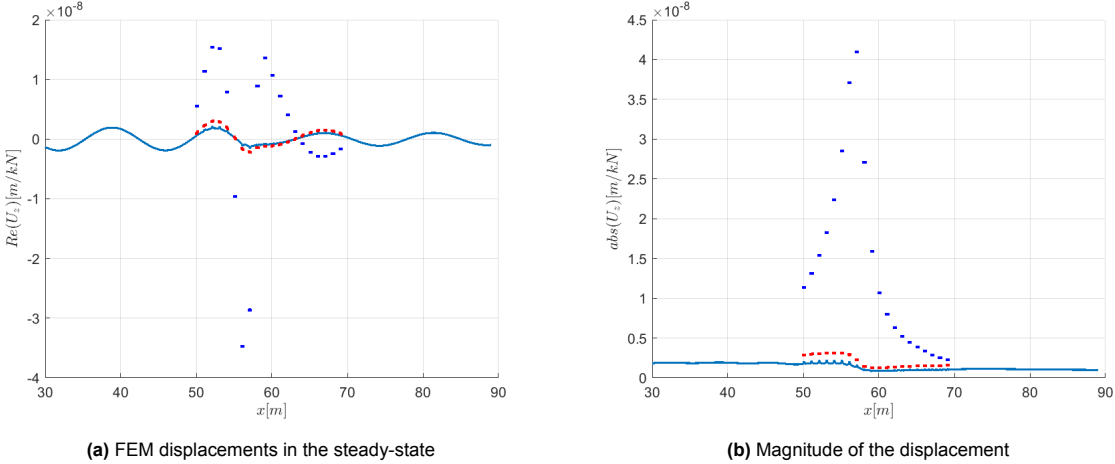


Figure 4.18: Vertical displacement of the resonators for the classic metawedge, in blue the rigid masses, in red the foundation

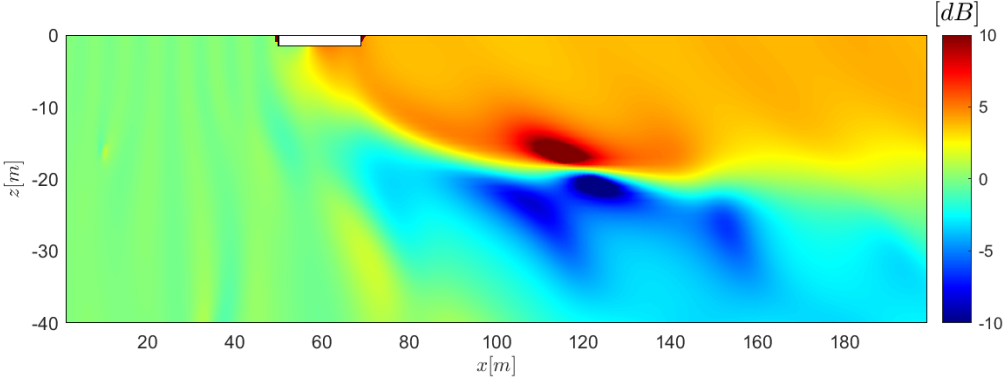


Figure 4.17: Vertical insertion loss for the classic metawedge at $F = 13$ Hz

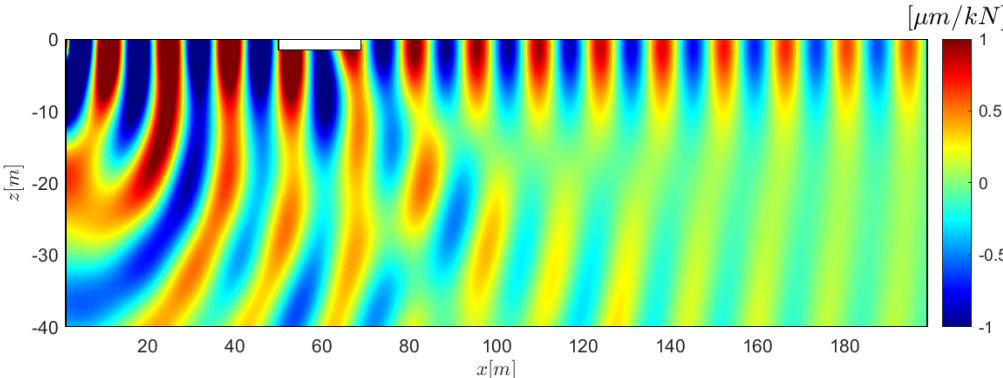


Figure 4.19: Real part of vertical displacement for the inverse metawedge at $F = 13$ Hz

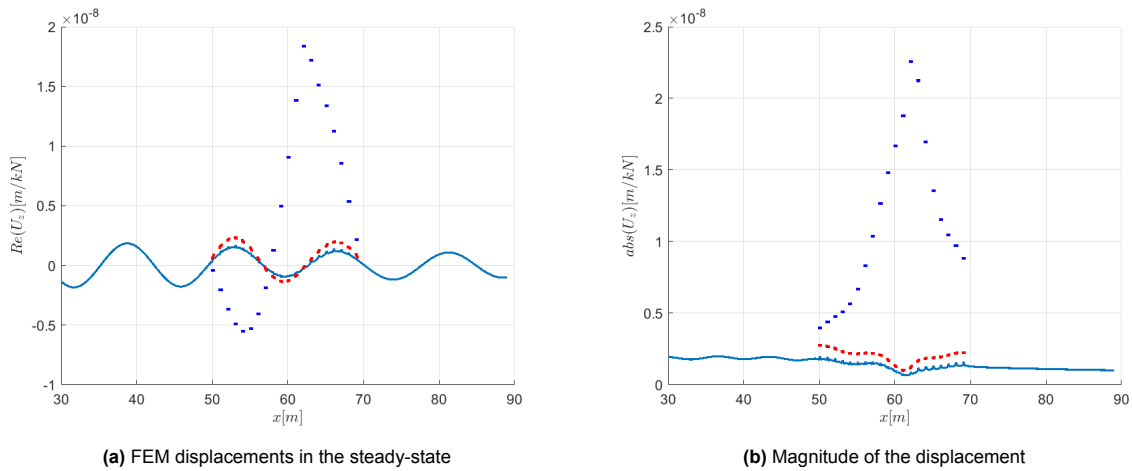


Figure 4.21: Vertical displacement of the resonators for the inverse metawedge, in blue the rigid masses, in red the foundation

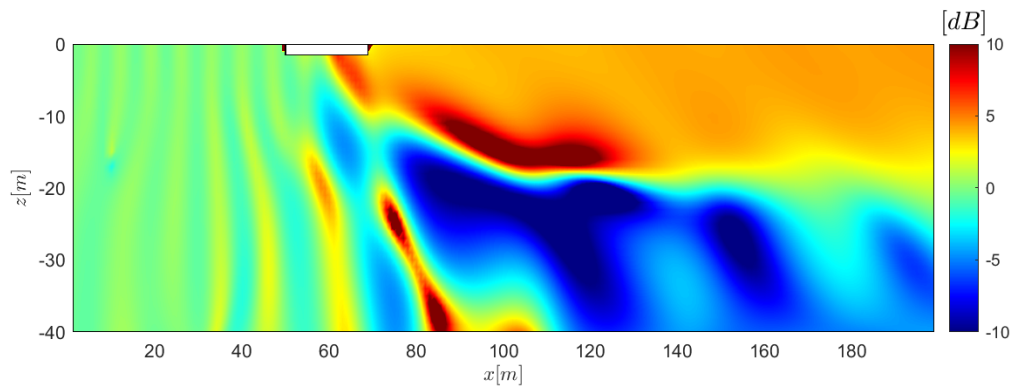


Figure 4.20: Vertical insertion loss for the inverse metawedge at $F = 13$ Hz

4.3. Wave characteristics analysis

The previous section highlighted how the configuration of the metawedge significantly influences the observed outcomes, underscoring the need for a more detailed analysis to understand the underlying mechanisms. There is clear evidence of wave manipulation occurring within the metawedge structure, and further investigation is required to elucidate these phenomena. Figures 4.22, 4.23, and 4.24 showcase the displacement of the soil just beneath the metawedge. The displacements under the metawedge are depicted in blue, while the displacements in scenarios devoid of metamaterials, serving as references, are shown in orange. Notably, small perturbations are visible at the locations of the resonators within the metawedge response. These are likely due to the application of point loads over small areas and are considered numerical artifacts that do not significantly impact the overall solution.

The results distinctly demonstrate that wave manipulation is taking place within the metawedge, as evidenced by variations in wavelength. However, these observations alone do not provide a conclusive understanding of the phenomena at play. To comprehensively characterize wave propagation within the metawedge, it is essential to determine the dispersive properties of the system. This is accomplished through a methodology akin to that used in Chapter 3.3, involving a wavenumber transform conducted over the region containing the metamaterials.

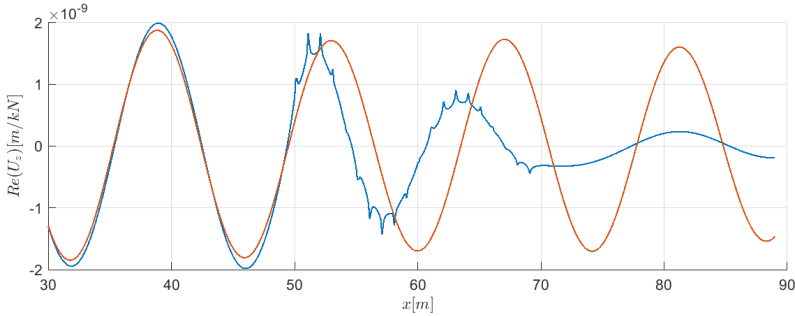


Figure 4.22: Vertical displacement of the soil under the uniform metawedge in blue, in orange the displacement in the homogeneous case

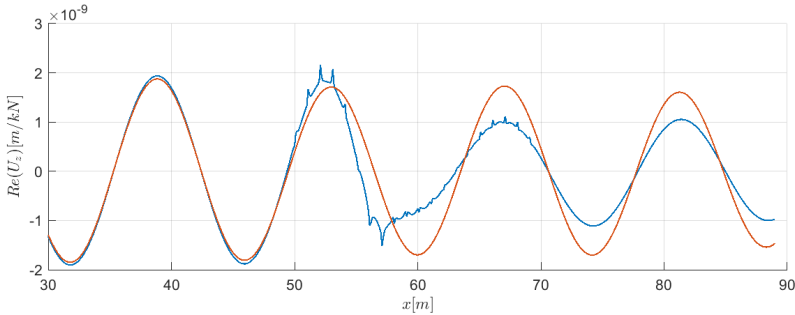


Figure 4.23: Vertical displacement of the soil under the classic metawedge in blue, in orange the displacement in the homogeneous case

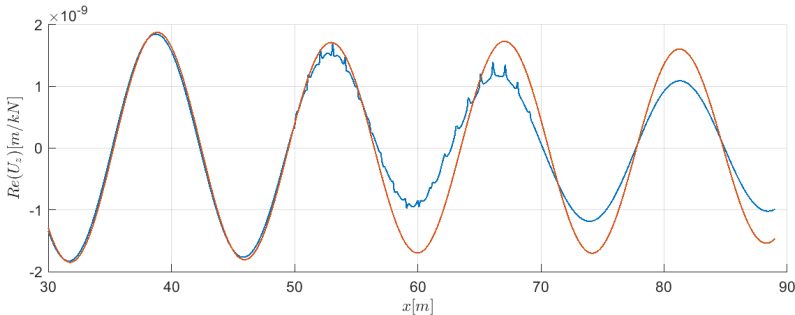


Figure 4.24: Vertical displacement of the soil under the inverse metawedge in blue, in orange the displacement in the homogeneous case

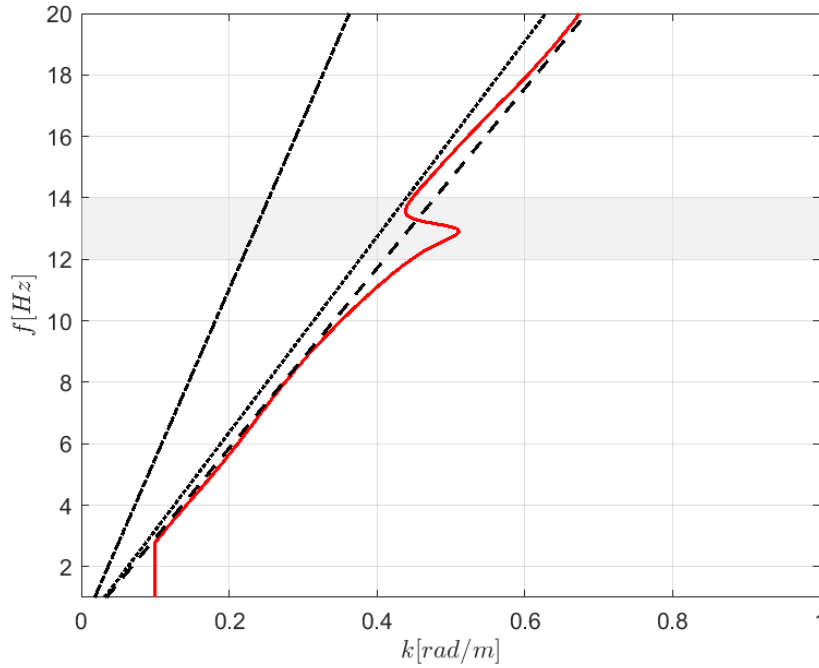


Figure 4.25: Dispersion curve for the uniform metawedge

The dispersion curve retrieved from the analysis is depicted in Figure 4.25, where the pressure wave is represented by a dash-dotted line, the shear wave by a dotted line, and the Rayleigh wave by a dashed line. The frequency range of the band gap is illustrated in grey. A key observation is the striking similarity of these results to those obtained in Chapter 2, underscoring the consistency between the analytically derived results and those currently examined. Analysis of the dispersion curve reveals that outside the band gap, the curve aligns closely with that of the Rayleigh wave, suggesting that the influence of the metamaterials is negligible in these regions. This alignment indicates that the propagation characteristics of Rayleigh waves remain largely unchanged outside the band gap. However, within the band gap frequencies, notable deviations occur: below the band gap, an increase in wavenumber suggests a reduction in wavelength, and conversely, above the band gap, a decrease in wavenumber indicates an increase in wavelength. Theoretically, it is understood that Rayleigh waves cannot propagate purely on the surface when their wavenumber is smaller than the shear wavenumber, leading to the generation of shear waves. To better understand the phenomena observed, it is essential to analyze the phase velocities of the waves, as detailed in Figure 4.26. This analysis reveals that frequencies below the natural frequencies of the resonators slow down, whereas those above are accelerated. This dynamic is pivotal to understanding the operation of both the classic and inverse metawedge configurations, where a wave initially encounters a resonator with either a lower or higher natural frequency than itself. Notably, for frequencies exceeding the natural frequency of the resonators, the phase velocity approaches the speed of shear waves, further supporting the observation that shear waves are generated when the phase velocity matches that of the shear wave speed. Further intriguing observations emerge when the system is excited at frequencies just outside the central frequency of the band gap (14 Hz above and 12 Hz below). In both scenarios, Rayleigh waves are prominently converted into shear waves, indicating that wave-mode conversion is effective across both smaller and larger wavenumbers. A potential explanation for this phenomenon could be the refraction effects caused by the inclusion of a stiff barrier, such as the foundation used in the model. Nonetheless, when analyses were conducted with only the foundation, wave-mode conversion was not distinctly observed, suggesting other contributing factors.

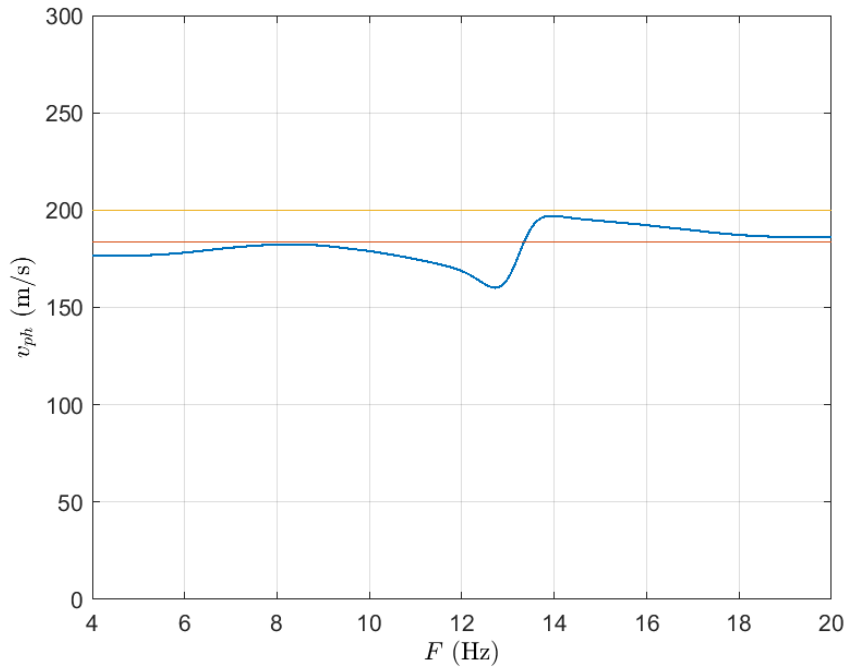


Figure 4.26: Phase velocity for the uniform metawedge in blue, in orange the Rayleigh wave speed, in yellow the shear wave speed

Extending the method of using a wavenumber transform over the entire metamaterial region to the classic and inverse metawedge configurations is impractical, as previously discussed in Chapter 3.4. In the uniform metawedge, where all unit cells share identical properties, a single wavenumber is sufficient to describe the entire structure. However, in the classic and inverse configurations, where each unit cell has unique properties, this approach is ineffective. To effectively analyze these configurations, it is essential to explore the dispersive properties of individual unit cells. This can be achieved by conducting a wavenumber transform on a uniform metawedge, adjusted to mimic the properties of a single unit cell. This analysis is carried out at a higher excitation frequency of 23 Hz to enhance accuracy due to shorter wavelengths, which improves the wavenumber transform given the limited spatial extent of the metawedge. By varying the natural frequency of the uniform metawedge, distinct wavenumbers for each natural frequency are collected, simulating how a wave at 23 Hz traverses the metawedge and adapts to the changing properties of each unit cell.

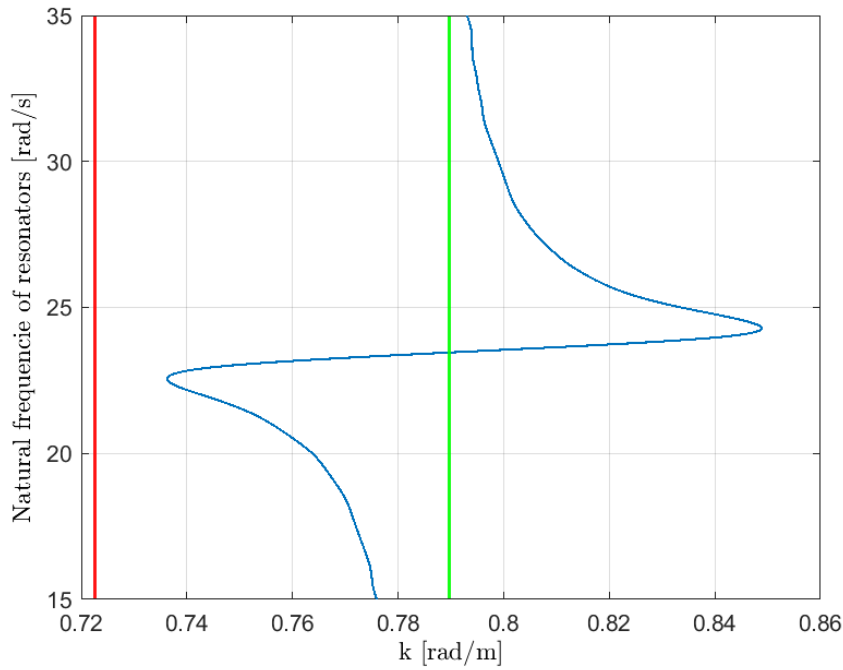


Figure 4.27: Wavenumber as function of resonator frequency, in green the Rayleigh wavenumber for 23 Hz, in red the shear wavenumber for 23 Hz

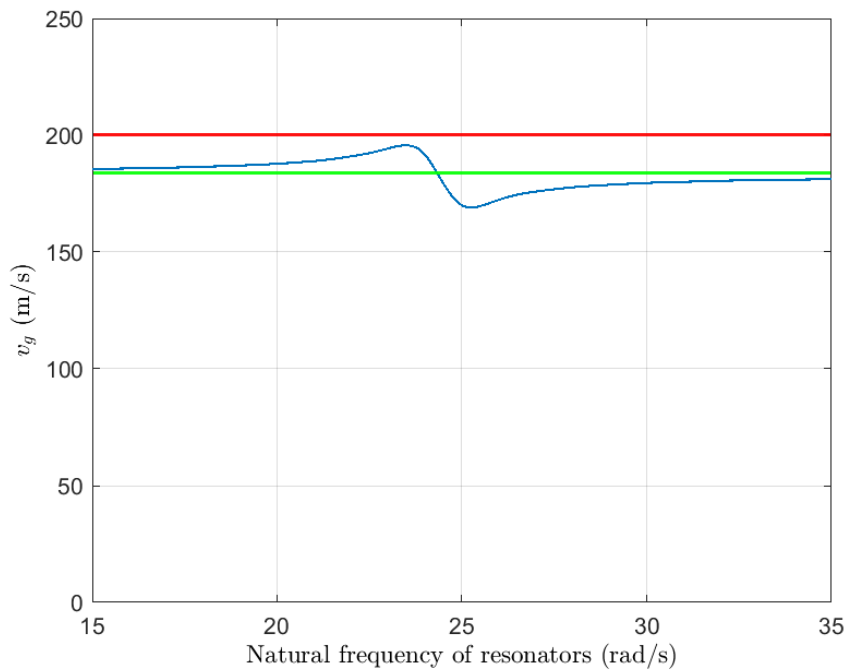


Figure 4.28: Phase velocity as function of resonator frequency, in green the Rayleigh wave speed, in red the shear wave speed

In Figures 4.27 and 4.28, the study presents the calculated wavenumbers and phase velocities for both the classic and inverse metawedge configurations. To understand these results, it is important to consider the specific setup of each metawedge. In the classic metawedge, waves start from a higher natural frequency of 35 Hz and move towards a lower frequency of 15 Hz. This means that as

the wave travels through the classic metawedge, its wavenumber increases, thereby decreasing its wavelength until it encounters the band gap. On the other hand, in the inverse metawedge, the wave starts at the lower frequency of 15 Hz and travels towards a higher frequency of 35 Hz, which causes the wavenumber to decrease and the wavelength to increase, suggesting a potential transition to shear wave propagation as the wavenumber nears that of shear waves.

The phase velocity analysis shows that in the classic metawedge, wave speeds decrease as they progress through the metawedge, reaching their slowest at the band gap. In contrast, the inverse metawedge exhibits an increase in phase velocity, nearing the speed of shear waves, which facilitates the conversion of Rayleigh waves into shear waves. This differential behavior highlights the distinct wave manipulation capabilities of each metawedge configuration, with the classic metawedge effectively trapping waves and the inverse metawedge facilitating wave-mode conversion. These findings align well with established literature, providing a comprehensive understanding of the underlying mitigation mechanisms within the classic and inverse metawedge configurations.

4.4. Parametric study

To optimize the effectiveness of the metawedge, this study focuses on identifying the optimal parameters that enhance its performance. The uniform metawedge configuration is utilized, allowing for the control of variables while systematically varying a single parameter at a time. This approach facilitates precise evaluations of how each change impacts the overall system efficiency. The primary goal is to ensure that each resonator within the metawedge dissipates as much energy as possible from the system. This parametric study will focus on the influence of the mass of the resonators, maintaining a constant natural frequency by adjusting the spring stiffness. The damping ratio, identified as a critical parameter for energy dissipation through Equation 4.7, will also be explored for its impact on the system's performance. Additionally, the study will assess how varying the number of resonators influences the overall effectiveness of the metawedge. By adjusting these parameters and examining their effects, the study aims to identify the most effective metawedge configuration that maximizes energy dissipation, enhancing the system's efficiency for practical vibration mitigation applications.

The study begins by examining the influence of the mass of the resonators on the performance of the metawedge, ensuring that the natural frequency remains constant to maintain the location of the band gap. This setup allows for a focused analysis of mass without altering other critical parameters, which are maintained as specified in Table 4.2. The results of this examination are illustrated in Figure 4.29. From these findings, there is a noticeable increase in insertion loss, peaking at around 300 kg. Initially, increasing the mass of the resonators boosts the energy dissipated by the system, enhancing the effectiveness of the metawedge in attenuating vibrations. However, beyond a certain threshold, the efficiency of the system begins to wane. This decline in performance can be traced to the dynamics described in the energy dissipation equation (Equation 4.4), where the velocity is squared. As the mass of the resonators increases, the relative displacement u of the mass tends to decrease, and so will the velocity. Since this term is squared, a decrease in velocity has a magnified effect on the energy dissipation, overshadowing the benefits of increased mass. Therefore, while adding mass initially appears beneficial, there is a critical point beyond which further increases result in reduced efficiency. This phenomenon highlights the need for careful calibration of the resonator mass to optimize the metawedge's performance, ensuring that the mass is sufficient to maximize energy dissipation without surpassing the threshold where the system's effectiveness begins to decrease.

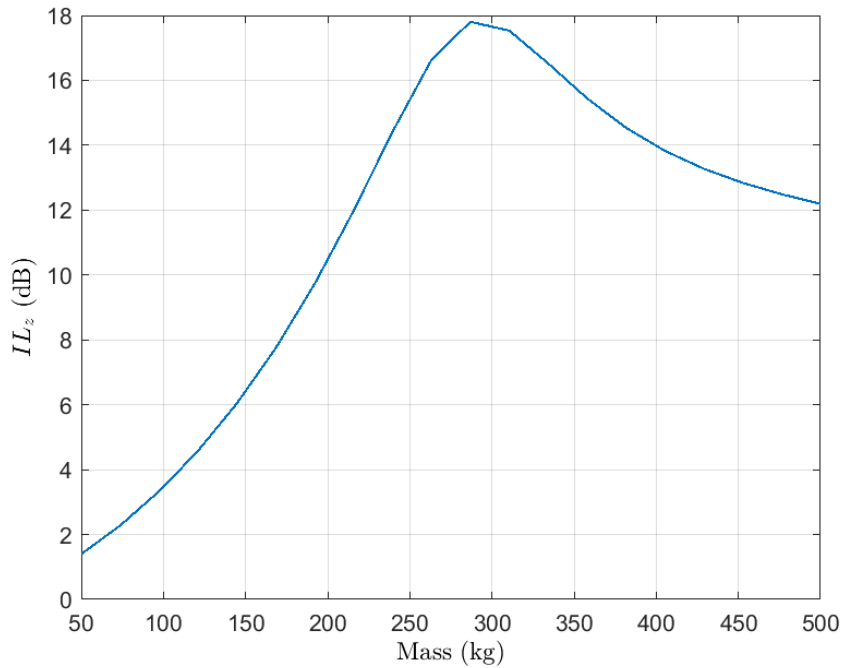


Figure 4.29: Influence of the mass, expressed as the insertion loss at $x = 90.1$, $y = 0$, $z = 0$, $F = 13$ Hz

Exploring the influence of damping on the metawedge's performance is crucial, as indicated by the energy dissipation characterised by Equation 4.4, which shows that damping is linearly proportional to the energy dissipated. This relationship suggests that increasing damping should directly enhance energy dissipation. However, the dynamics of this relationship are more nuanced due to the impact of damping on the velocity of the mass, which is squared in Equation 4.4. As the damping ratio increases, the velocity of the mass typically decreases. Since the velocity term is squared in the energy dissipation equation, a reduction in velocity has a disproportionately large impact on energy dissipation, potentially offsetting the benefits of increased damping. This dynamic is evident in the results presented in Figure 4.30, which demonstrate that the system may actually be more effective at lower damping levels. At these levels, the mass's velocity remains relatively high, leading to greater energy dissipation. However, it is important to note that while lower damping ratios enhance the system's effectiveness by maintaining higher velocities, they also have a drawback: they tend to narrow the band gap. A narrower band gap can limit the frequency range over which the metawedge effectively reduces vibrations. Thus, achieving an optimal balance in the damping ratio is essential. It must be sufficient to allow substantial energy dissipation while also maintaining a band gap broad enough to be effective across the necessary range of frequencies.

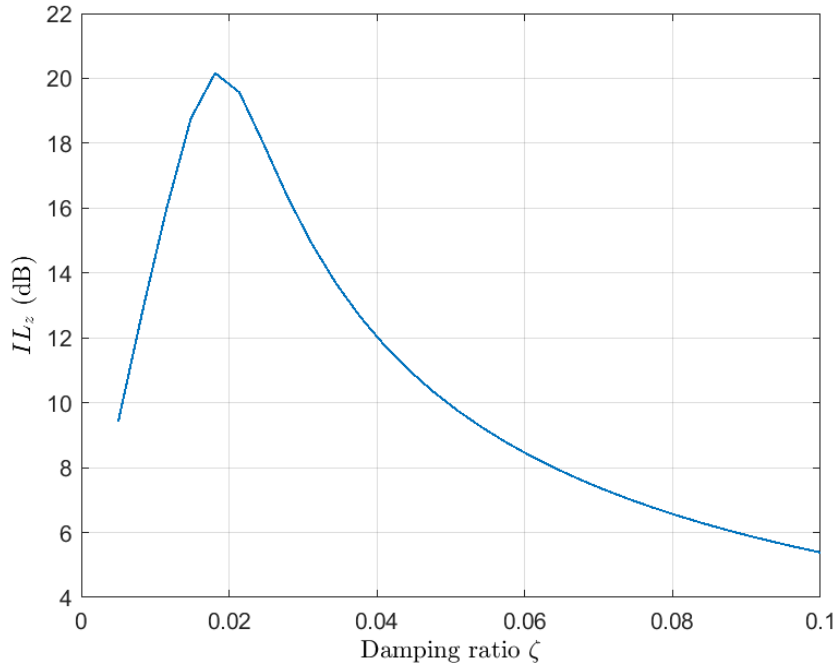


Figure 4.30: Influence of the damping ratio, expressed as the insertion loss at $x = 90.1, y = 0, z = 0, F = 13$ Hz

Lastly, the study investigates the optimal number of resonators required to achieve adequate attenuation levels. This assessment evaluates the insertion loss associated with varying quantities of resonators, maintaining all other parameters constant as outlined in Table 4.2. The analysis reveals a linear relationship in the effectiveness of each additional resonator, particularly when presented in a logarithmic scale as shown in Figure 4.31a. Consequently, the results are also depicted as the amplitude ratio between the normal and mitigated displacement in Figure 4.31b. This illustration indicates that each additional resonator contributes to an increasing amount of attenuation. Given that the study focuses on a uniform metawedge, the predominant mechanism of energy dissipation is wave-mode conversion, suggesting that multiple resonators are necessary to effectively speed up the waves. Therefore, a longer metawedge configuration proves more capable of influencing wave characteristics, enhancing its effectiveness in wave-mode conversion. The findings in 4.31a suggests that there is no diminishing return on adding resonators within the scope of this study, making it straightforward to predict the total attenuation effect, in terms of insertion loss, based on the number of resonators used. This insight is crucial for designing metawedge systems that need to meet specific attenuation criteria, as it allows for precise scaling based on the number of resonators without concern for efficiency loss as more units are added. This scalability is particularly advantageous in applications where variable levels of vibration reduction are required.

4.5. Influence of incidence angle

In this study, the methodology from Chapter 4 is expanded upon by transitioning from a two-dimensional to a three-dimensional model. This shift requires the analysis of responses across the space-frequency-wavenumber domain for multiple wavenumbers, which are then converted to the space-frequency domain using an inverse Fourier transform. Given the model's formulation as a superposition of various wavenumbers (k_y), a discrete representation of these wavenumbers becomes crucial. This discretization employs a dimensionless wavenumber approach, $\bar{k}_y = k_y c_s / \omega$, facilitating accurate results, particularly in far-field scenarios. As per the findings of Francois et al. [16], a maximum dimensionless wavenumber of $\bar{k}_y = 3$ suffices for accurately modeling far-field displacements. The discretization of \bar{k}_y is conducted over 300 samples ranging from $\bar{k}_y = 0$ to $\bar{k}_y = 3$, ensuring thorough and accurate analytical results.

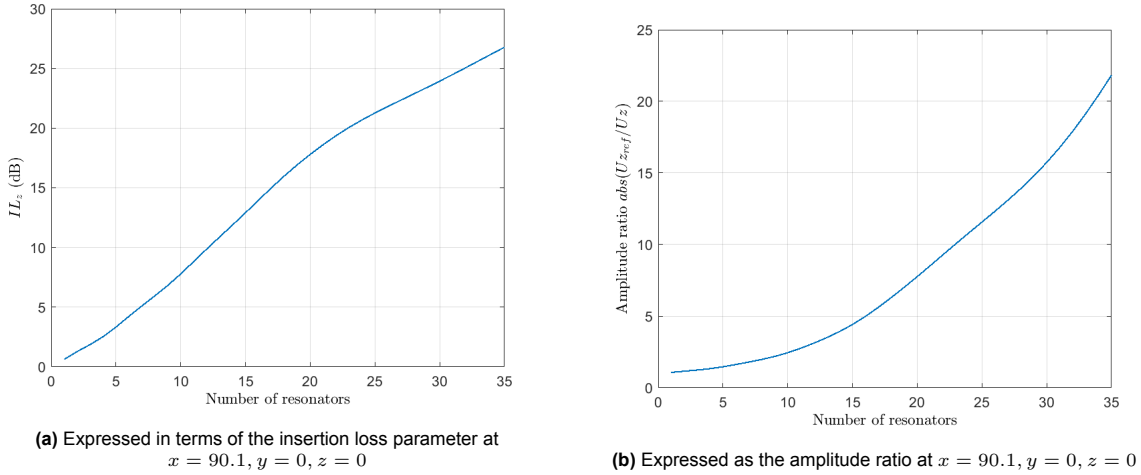


Figure 4.31: Influence of the number of resonators, $F = 13$ Hz

The implementation of this approach is contingent upon uniformity in geometry or properties in the y -direction. However, this uniformity introduces certain limitations due to the model's setup, as depicted in Figure 4.3. The foundation and mass in the model are represented by two elements that are artificially stiffened to counteract the effects of singularities caused by the spring exerting a substantial force over a small area. These elements are made exceedingly stiff by assigning a very high Young's modulus, which results in a considerable bending stiffness (EI) due to their significant width (0.2m) and height (0.1m). While this configuration was suitable in the previous chapter's two-dimensional model, where the model essentially functioned under a 3D scenario excited by a line load with all incident waves approaching perpendicularly, the three-dimensional model introduces new complexities. Now, being excited by a harmonic point load, the model receives waves at various incidence angles. This variation means that the bending stiffness of the beam could potentially influence vibration mitigation, effectively acting like a stiff trench that redirects the wave along the beam. Consequently, for large incident angles, the results may not accurately reflect the real-world performance of the mitigation measure, given that the intended design aimed to represent a lattice of resonators in both the x - and y -directions. Unfortunately, such a model is not feasible with this software. However, for small incident angles, this study can still provide valuable insights.

For the three-dimensional analysis, the same parameters outlined in Tables 4.2, 4.3, and 4.4 will be utilized for the uniform, classic, and inverse metawedge configurations respectively. The real part of the vertical displacement, along with the insertion loss, are depicted in Figures 4.32, 4.33, and 4.34. These results demonstrate that the metawedge performs exceptionally well for small incidence angles. At higher incidence angles, however, the bending mode of the beam is activated. Notably, considerable reflections are observed in the uniform and inverse configurations, which are absent in the classic metawedge, underscoring its capacity to effectively trap waves within the structure. Further analysis of the metawedge's performance under various incidence angles is presented in Figures 4.35, 4.36, and 4.37. These Figures reveal a well-defined formation of the band gap, which proves effective even at low incidence angles in the 0 to 40-degree range—a region where traditional mitigation measures like trenches typically underperform, as evidenced in Figure 4.7b where there is minimal mitigation at low frequencies and incidence angles. Beyond 45 degrees, the bending mode of the beam becomes prominent, an artifact attributed to the modeling technique. Consequently, the results at higher incidence angles may not provide an accurate depiction of the metawedge's capabilities in real-world scenarios.

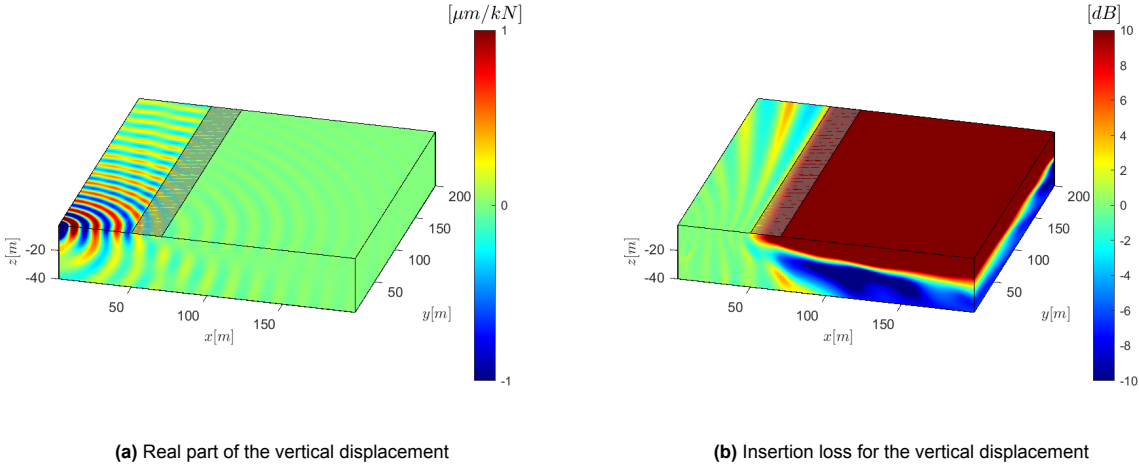


Figure 4.32: Uniform metawedge responses at 13 Hz

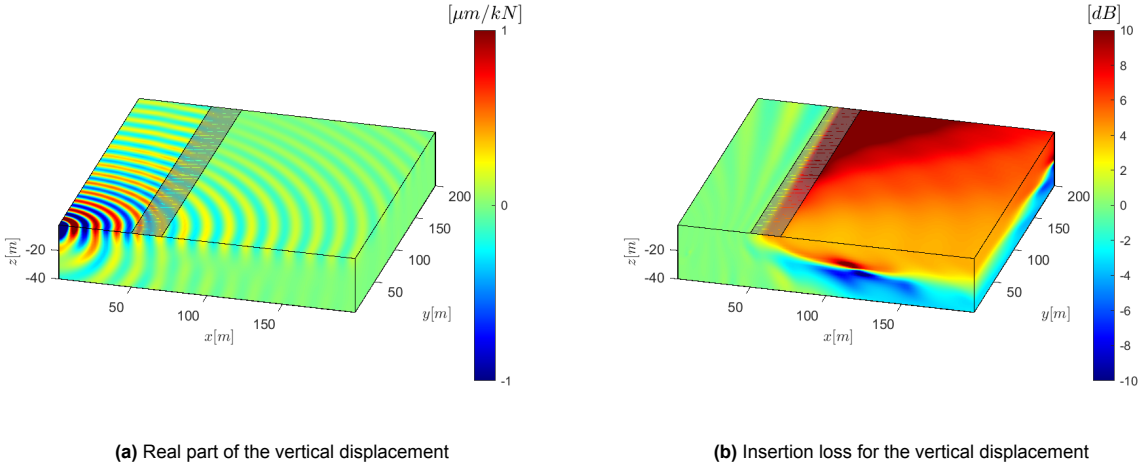


Figure 4.33: Classic metawedge responses at 13 Hz

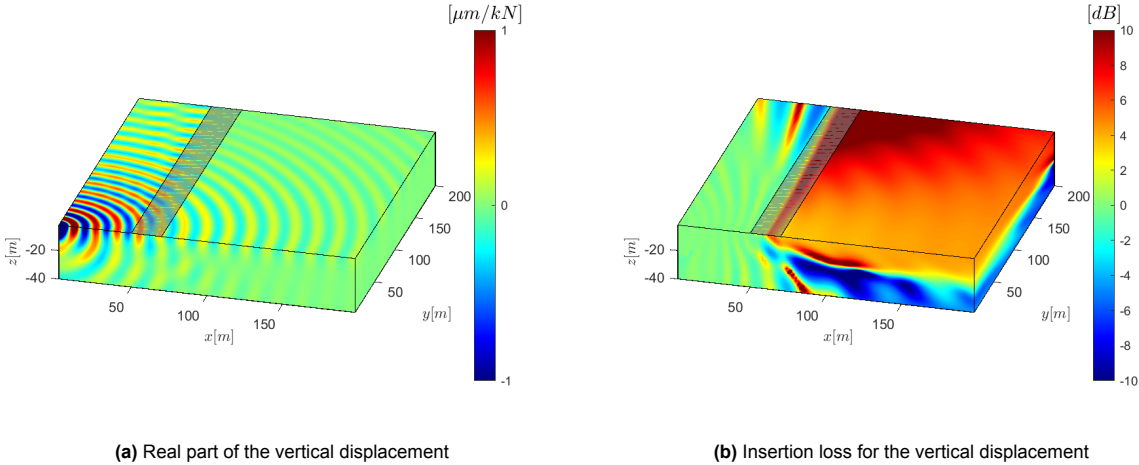


Figure 4.34: Inverse metawedge responses at 13 Hz

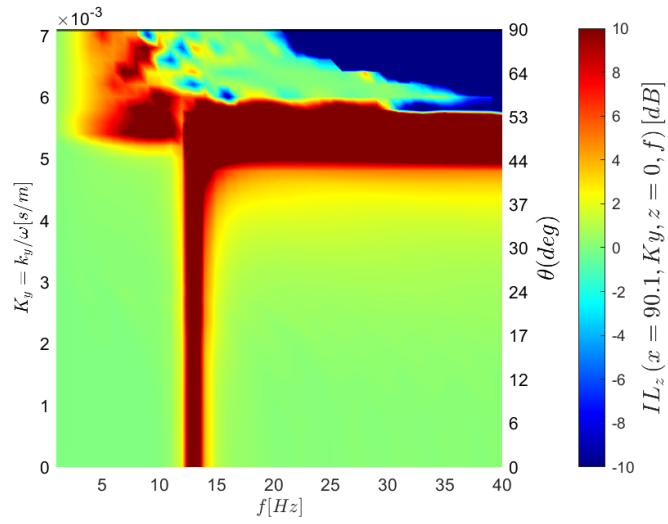


Figure 4.35: Insertion loss for the vertical displacement of the uniform metawedge

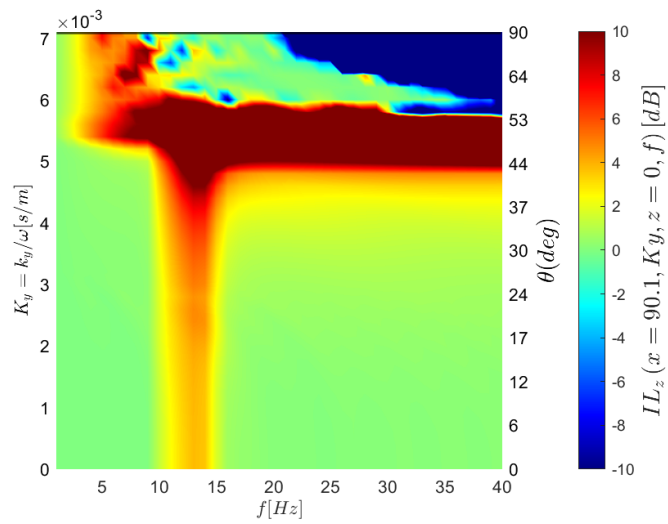


Figure 4.36: Insertion loss for the vertical displacement of the inverse metawedge

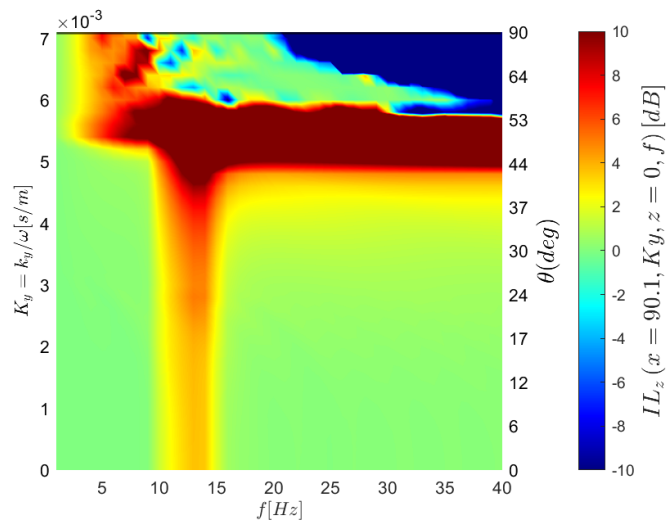


Figure 4.37: Insertion loss for the vertical displacement of the classic metawedge

4.6. Summary

The objective of this chapter is to elucidate the mitigation mechanisms of the metawedge and its various configurations, employing a three-dimensional wave propagation model simplified to two dimensions. This simplification is advantageous in early design stages due to its significantly reduced computational demands. The model incorporates single-degree of freedom resonators positioned on top of the surface, with the soil excited by a stationary harmonic point load. The band gaps for different configurations are identified by calculating the insertion loss behind the mitigation measure. The findings indicate that band gaps are generated through local resonance and Bragg scattering, aligning closely with the analytical model discussed in Chapter 2. This alignment demonstrates an excellent correlation between the simplified analytical model and the numerical approach. The local resonance band gap location can be approximated using the decoupled natural frequency of the resonators, whereas the location of the Bragg band gap is determined by comparing the wavelength of the wave with the spatial distance between the resonators, revealing that a band gap occurs when half a wavelength fits an integer multiple of the spacing. It was observed that the local resonance effect produces a significantly stronger band gap than Bragg scattering. The robustness of the local resonance, coupled with its flexibility in tuning and the relatively compact spatial area required for constructing a metamaterial based on this principle, renders the local resonance-based design considerably more appealing for practical applications.

An investigation into the mitigation mechanics of different metawedge configurations has identified two primary mechanisms: absorption, and wave-mode conversion. Energy absorption is facilitated through dissipation by the resonators. Wave-mode conversion involves the transformation of Rayleigh waves into shear waves, which then propagate deeper into the soil. Each configuration of the metawedge utilizes these mechanisms to varying degrees. The classic metawedge predominantly harnesses energy absorption through its resonators, a process often referred to in literature as "rainbow trapping". In contrast, the inverse metawedge primarily employs wave-mode conversion as its mechanism. Further analysis of these mechanisms reveals distinct behaviors in wave propagation within different configurations. In the classic metawedge, a wave is slowed, and its wavenumber increases, leading to a shorter wavelength that becomes trapped within the wedge. Conversely, in the inverse metawedge, the wave is sped up as its wavenumber decreases, differing from the behavior observed in the classic wedge. When the surface waves' wavenumber becomes closer to that of the shear wavenumber it can no longer only propagate along the surface but instead will start to radiate shear waves into the soil. Showing an excellent agreement with literature.

A parametric study was undertaken to evaluate the influence of mass, damping, and the number of resonators on the performance of metawedge configurations. Results demonstrated that increasing the mass of the resonators boosts the strength of the band gap until reaching a certain threshold. Notably, a reduction in damping ratio was found to enhance the amplitude of the resonators without inducing negative effects. The addition of more resonators enabled precise tuning of the band gap's strength. A crucial finding from the study is that the width of the band gap can be broadened by adjusting the natural frequency of the resonators. These insights confirm that both classic and inverse metawedge configurations are effective vibration mitigation strategies. The inverse metawedge, in particular, shows significant potential by channeling energy deeper into the soil, although it risks reflecting energy back to the surface when encountering a stiff sub layer. In contrast, the classic metawedge effectively traps energy within the wedge, offering advantages such as minimal risk of reflection and reduced energy transmission back to the source, potentially decreasing the degradation of train tracks. Further analysis of the metawedge's performance across various incidence angles revealed its superior efficacy at low angles—a range where traditional mitigation measures typically underperform. The study substantiates the practicality of deploying a metawedge system weighing only 300 kg/m to effectively counter low-frequency vibrations, with even better performance observed at higher frequencies.

5

Conclusions and recommendations

5.1. Conclusion

This thesis studies the fundamental physics that govern the mitigation mechanisms of the metawedge, starting with a simplified one-dimensional wave propagation analysis. The chosen model is the Euler-Bernoulli beam on a visco-elastic foundation, which aptly simulates soil behavior and facilitates the examination of transverse wave displacement. Metamaterials are introduced in two distinct configurations: one involving the integration of discrete, periodic local mass-spring-dashpot systems linked directly to the beam's degrees of freedom, and another where masses are connected through a spring-dashpot system, forming single-degree of freedom resonators arranged periodically along the beam. Given the periodic nature of the system, it is analyzed using the Floquet theorem, which helps elucidate the dispersive properties for both configurations. Analysis of the beam with linked mass-spring-dashpots reveals the creation of a band gap due to the system's periodicity, primarily resulting from Bragg scattering. This type of band gap occurs when the spacing between the metamaterials aligns with an integer multiple of half the wavelength of the excited wave. The lower boundary of this band gap is determined by locating the wavenumber in the Floquet dispersion curve that corresponds to an integer multiple of half the wavelength, while the upper boundary uses the dispersion curve of the homogeneous beam for its calculation. In the configuration utilizing free metamaterials, the beam displays band gaps initiated by two mechanisms: the aforementioned Bragg scattering and a second band gap induced by the local resonance of the metamaterials. This latter band gap's central frequency can be approximated by calculating the natural frequency of the resonators when considered as uncoupled.

The study progressed by examining the metawedge, a distinctive configuration of above-surface resonators comprising of unit cells, each possessing unique natural frequencies and dispersive properties. The specific arrangement of these unit cells defines the type of metawedge: the classic metawedge begins with unit cells at the highest natural frequency, decreasing progressively; inversely, the incident wave in an inverse metawedge encounters the lowest natural frequencies first, increasing as it travels through the structure. Due to the finite number of resonators in the model, Floquet analysis was unsuitable; instead, a finite element model was employed to solve the problem. This approach successfully captured the dispersive properties of the metamaterials, aligning closely with analytical predictions. Subsequent analysis of dispersion characteristics and phase velocities in these configurations showed that the classic metawedge effectively slows down phase velocities, leading to shorter wavelengths that approximate twice the spacing between resonators. In contrast, the inverse metawedge causes an acceleration of phase velocities and lengthening of wavelengths, aligning well with findings in the literature. However, the model's constraints prevented a clear distinction in behavior between the classic and inverse configurations.

Transitioning from a one-dimensional wave propagation model to a three-dimensional model yielded significant insights, particularly confirming the strong agreement between the analytical and numerical models. This validation was evident in the precise prediction and formation of band gaps driven by local resonance and Bragg scattering. Specifically, the study detailed how the classic and in-

verse metawedge configurations manipulate wave propagation: the classic metawedge effectively traps waves within its structure, utilizing "elastic rainbow trapping," while the inverse metawedge converts incoming Rayleigh waves into body waves that penetrate deeper into the soil. Further analysis of the dispersive properties within these configurations revealed significant variations in wave behavior. In the classic metawedge, waves experience a decrease in phase velocity, which is accompanied by an increase in wavenumber, effectively reducing the wavelength to match precisely half the spacing between resonators and thereby trapping the wave. Conversely, the inverse metawedge speeds up the waves, resulting in a decrease in wavenumber that approaches the shear wavenumber. This study highlights that the reduction in wavenumber coupled with an increase in phase velocity is essential for facilitating wave-mode conversion, offering critical insights into the mitigation mechanics of both configurations.

The second part of this analysis focuses on engineering a metamaterial-based solution effective for low frequencies and small incidence angles. The design leverages principles of Bragg scattering and local resonance for vibration attenuation. However, Bragg scattering is less feasible for low frequencies due to its reliance on spatial periodicity, which would necessitate unfeasibly long mitigation measures due to the corresponding long wavelengths. In contrast, the local resonance band gap offers considerable advantages. This band gap can be precisely tuned by adjusting the natural frequencies of the resonators. Moreover, the strength of the band gap can be enhanced by employing resonators with higher mass, lower damping ratios, or increasing the number of resonators. Such flexibility makes local resonance-based designs highly adaptable to various scenarios. The study substantiates the practicality of deploying a metawedge system weighing only 300 kg/m to effectively counter low-frequency vibrations, with even better performance observed at higher frequencies. Three-dimensional analysis of the metawedge configurations demonstrated their efficacy for small incidence angles—a critical area where they surpass traditional mitigation measures like trenches. Both the classic and inverse configurations of the metawedge delivered comparable levels of vibration mitigation. However, they differ in their wave manipulation techniques: the inverse metawedge converts Rayleigh waves into bulk waves that penetrate deeper into the soil, posing a risk of wave reflection if a stiff sub-layer is encountered. Conversely, the classic metawedge excels in trapping waves within the wedge, evidenced by significantly higher dissipation by the dash pots in its resonators compared to those in the inverse configuration. This distinct behavior underscores the classic metawedge's potential for effectively containing vibration energy without the risk of reflective interactions with sub-layers.

5.2. Recommendations for further research

This research confirms the potential for a practical metamaterial-based solution for mitigating low-frequency vibrations. However, the use of a 2.5D model presents limitations, particularly in accurately modeling resonators. This model suffices for a two dimensional design but falls short in assessing the mitigation measure's performance under varied excitation angles, as excited by trains. To address this, integrating a comprehensive 3D model is advisable. Furthermore incorporating such a model would enhance the understanding of the dispersive properties of the unit cell and the dynamics of wave-mode conversion, through an analysis of the unit cell in combination with periodic boundary conditions. Future research could explore alternative designs for the unit cell, building upon the findings of this thesis which has illuminated the mechanics behind rainbow trapping and wave-mode conversion, primarily influenced by the changes in wavenumber of the incident wave. Investigating various configurations of the metawedge, beyond the linear variations considered in this study, could offer deeper insights and potentially more efficient designs for manipulating wave propagation in practical applications.

To further enhance the model and address potential risks identified in this study, introducing multiple soil layers would be a next step. Particularly for the inverse metawedge configuration, it would be insightful to examine how the converted waves are reflected back to the surface under different soil conditions. This addition would not only add complexity but also alter the dispersive properties of the soil. Given that metamaterials have been shown to affect local dispersive properties significantly, it would be intriguing to explore how these changes manifest across layered soil structures, potentially affecting the overall efficacy and behavior of the mitigation strategies. Exploring alternative configurations for metamaterials presents an exciting avenue for future research. Currently, this study utilizes a single degree of freedom (SDOF) system; however, expanding this to multi-degree of freedom (MDOF)

resonators could offer new dimensions of control, potentially enabling the creation of multiple bandgaps. Additionally, incorporating horizontal springs could harness the horizontal motion of Rayleigh waves, further diversifying the band gap mechanisms. Beyond traditional mass-spring-dashpot systems, there is potential in adopting advanced methodologies from fields like photonics where AI is used to design unit cells with specific properties. Introducing non-linearity into the metamaterials could also enhance energy dissipation capabilities, offering robust solutions to vibration mitigation challenges.

Given the promising results of this thesis, the next step could involve experimental validation through full-scale or scaled laboratory tests. A feasible design, proven effective with relatively low mass, suggests that real-world application is achievable. Conducting full-scale tests by placing resonators near a train track to measure vibration levels before and after installation could provide direct evidence of efficacy. Alternatively, a scaled laboratory setup could simulate these conditions, offering a controlled environment for detailed analysis. Such experimental studies could be pivotal in demonstrating the viability and practicality of a metamaterial-based solution, potentially persuading investors and stakeholders of its effectiveness.

References

- [1] Alessandro Bracci, *Assessment of Stiff Trench and Metawedge as Mitigation Measures for Railway Induced Ground Vibration*, 2021.
- [2] L. Andersen and S. R. Nielsen, "Reduction of ground vibration by means of barriers or soil improvement along a railway track," *Soil Dynamics and Earthquake Engineering*, vol. 25, no. 7-10, pp. 701–716, Aug. 2005, ISSN: 0267-7261. DOI: 10.1016/J.SOILDYN.2005.04.007.
- [3] J. Barbosa, P. Alves Costa, and R. Calçada, "Abatement of railway induced vibrations: Numerical comparison of trench solutions," *Engineering Analysis with Boundary Elements*, vol. 55, pp. 122–139, Jun. 2015, ISSN: 0955-7997. DOI: 10.1016/J.ENGANABOUND.2014.11.029.
- [4] "Brillouin L. - Wave Propagation in Periodic Structures - First Edition,"
- [5] S. Brûlé, S. Enoch, and S. Guenneau, "Emergence of seismic metamaterials: Current state and future perspectives," *Physics Letters A*, vol. 384, no. 1, p. 126 034, Jan. 2020, ISSN: 0375-9601. DOI: 10.1016/J.PHYSLETA.2019.126034.
- [6] D. Carneiro, "Vibration mitigation using seismic metamaterials on layered soil," *Proceedings of the 12th International Conference on Structural Dynamics, Eurodyn 2023*,
- [7] A. Colombi, V. Ageeva, R. J. Smith, *et al.*, "Enhanced sensing and conversion of ultrasonic Rayleigh waves by elastic metasurfaces," *Scientific reports*, vol. 7, no. 1, Dec. 2017, ISSN: 2045-2322. DOI: 10.1038/S41598-017-07151-6. [Online]. Available: <https://pubmed.ncbi.nlm.nih.gov/28754967/>.
- [8] A. Colombi, D. Colquitt, P. Roux, S. Guenneau, and R. V. Craster, "A seismic metamaterial: The resonant metawedge," *Scientific Reports*, vol. 6, Jun. 2016, ISSN: 20452322. DOI: 10.1038/SREP27717. [Online]. Available: https://www.researchgate.net/publication/303908690_A_seismic_metamaterial_The_resonant_metawedge.
- [9] A. Colombi, P. Roux, S. Guenneau, P. Gueguen, and R. V. Craster, "Forests as a natural seismic metamaterial: Rayleigh wave bandgaps induced by local resonances," *Scientific Reports*, vol. 6, Jan. 2016, ISSN: 20452322. DOI: 10.1038/SREP19238.
- [10] D. J. Colquitt, A. Colombi, R. V. Craster, P. Roux, and S. R. Guenneau, "Seismic metasurfaces: Sub-wavelength resonators and Rayleigh wave interaction," *Journal of the Mechanics and Physics of Solids*, vol. 99, pp. 379–393, Feb. 2017, ISSN: 0022-5096. DOI: 10.1016/J.JMPS.2016.12.004.
- [11] D. P. Connolly, G. Kouroussis, O. Laghrouche, C. L. Ho, and M. C. Forde, "Benchmarking railway vibrations – Track, vehicle, ground and building effects," *Construction and Building Materials*, vol. 92, pp. 64–81, Sep. 2015, ISSN: 0950-0618. DOI: 10.1016/J.CONBUILDMAT.2014.07.042.
- [12] P. Coulier, A. Dijkmans, S. François, G. Degrande, and G. Lombaert, "A spatial windowing technique to account for finite dimensions in 2.5D dynamic soil–structure interaction problems," *Soil Dynamics and Earthquake Engineering*, vol. 59, pp. 51–67, Apr. 2014, ISSN: 0267-7261. DOI: 10.1016/J.SOILDYN.2014.01.006.
- [13] P. Coulier, S. François, G. Degrande, and G. Lombaert, "Subgrade stiffening next to the track as a wave impeding barrier for railway induced vibrations," *Soil Dynamics and Earthquake Engineering*, vol. 48, pp. 119–131, May 2013, ISSN: 0267-7261. DOI: 10.1016/J.SOILDYN.2012.12.009.
- [14] A. B. Faragou, A. V. Metrikine, and K. N. Van Dalen, "Settlement at transition zones in railway tracks-is modelling the soil as a 2-D continuum important?" *Proceedings of the 12th International Conference on Structural Dynamics, Eurodyn 2023*,
- [15] A. B. Fărăgău, J. M. de Oliveira Barbosa, A. V. Metrikine, and K. N. van Dalen, "Dynamic amplification in a periodic structure with a transition zone subject to a moving load: Three different phenomena," *Mathematics and Mechanics of Solids*, vol. 27, no. 9, pp. 1740–1760, Sep. 2022, ISSN: 17413028. DOI: 10.1177/10812865221094318/ASSET/IMAGES/LARGE/10.1177/{_}10812865221094318-FIG18.JPEG. [Online]. Available: <https://journals.sagepub.com/doi/full/10.1177/10812865221094318>.

- [16] S. François, M. Schevenels, P. Galvín, G. Lombaert, and G. Degrande, "A 2.5D coupled FE–BE methodology for the dynamic interaction between longitudinally invariant structures and a layered halfspace," *Computer Methods in Applied Mechanics and Engineering*, vol. 199, no. 23–24, pp. 1536–1548, Apr. 2010, ISSN: 0045-7825. DOI: 10.1016/J.CMA.2010.01.001.
- [17] C. van Hoorickx, "Design of vibration reduction measures for railway traffic by means of topology optimization," Tech. Rep., 2017.
- [18] H. H. Hung, Y. B. Yang, and D. W. Chang, "Wave Barriers for Reduction of Train-Induced Vibrations in Soils," *Journal of Geotechnical and Geoenvironmental Engineering*, vol. 130, no. 12, pp. 1283–1291, Dec. 2004, ISSN: 1090-0241. DOI: 10.1061/(ASCE)1090-0241(2004)130:12(1283).
- [19] International Union of Railways, "UIC state-of-the-art report on Railway noise in Europe," Tech. Rep., 2021.
- [20] Z. Kabirian, "Design and optimization of seismic metamaterials to mitigate ground vibration," *Proceedings of the 12th International Conference on Structural Dynamics, Eurodyn 2023*,
- [21] J. D. Manuel Oliveira Barbosa, "ANALYSIS AND MITIGATION OF VIBRATIONS INDUCED BY THE PASSAGE OF HIGH-SPEED TRAINS IN NEARBY BUILDINGS,"
- [22] A. E. Miroshnichenko, S. Flach, and Y. S. Kivshar, "Fano resonances in nanoscale structures," *Reviews of Modern Physics*, vol. 82, no. 3, pp. 2257–2298, Aug. 2010, ISSN: 00346861. DOI: 10.1103/REVMODPHYS.82.2257.
- [23] S. Ouakka, O. Verlinden, and G. Kouroussis, "Railway ground vibration and mitigation measures: benchmarking of best practices," *Railway Engineering Science*, vol. 30, no. 1, pp. 1–22, Mar. 2022, ISSN: 26624753. DOI: 10.1007/S40534-021-00264-9/FIGURES/4. [Online]. Available: <https://link.springer.com/article/10.1007/s40534-021-00264-9>.
- [24] A. Palermo, S. Krödel, A. Marzani, and C. Daraio, "Engineered metabarrier as shield from seismic surface waves," *Scientific Reports*, vol. 6, Dec. 2016, ISSN: 20452322. DOI: 10.1038/SREP39356.
- [25] M. G. Smith, I. Croy, M. Ögren, and K. Persson Waye, "On the Influence of Freight Trains on Humans: A Laboratory Investigation of the Impact of Nocturnal Low Frequency Vibration and Noise on Sleep and Heart Rate," *PLOS ONE*, vol. 8, no. 2, e55829, Feb. 2013, ISSN: 1932-6203. DOI: 10.1371/JOURNAL.PONE.0055829. [Online]. Available: <https://journals.plos.org/plosone/article?id=10.1371/journal.pone.0055829>.
- [26] D. J. Thompson, J. Jiang, M. G. Toward, *et al.*, "Mitigation of railway-induced vibration by using subgrade stiffening," *Soil Dynamics and Earthquake Engineering*, vol. 79, pp. 89–103, Dec. 2015, ISSN: 0267-7261. DOI: 10.1016/J.SOILDYN.2015.09.005.
- [27] D. Thompson, "Railway Noise and Vibration: Mechanisms, Modelling and Means of Control," *Railway Noise and Vibration: Mechanisms, Modelling and Means of Control*, pp. 1–518, Jan. 2009. DOI: 10.1016/B978-0-08-045147-3.X0023-0. [Online]. Available: <http://www.sciencedirect.com/5070/book/9780080451473/railway-noise-and-vibration>.
- [28] C. Van Hoorickx, M. Schevenels, and G. Lombaert, "Double wall barriers as mitigation measures for ground vibration transmission," *Procedia Engineering*, vol. 199, pp. 2735–2740, Jan. 2017, ISSN: 1877-7058. DOI: 10.1016/J.PROENG.2017.09.301.
- [29] H. Xia, N. Zhang, and Y. M. Cao, "Experimental study of train-induced vibrations of environments and buildings," *Journal of Sound and Vibration*, vol. 280, no. 3-5, pp. 1017–1029, Feb. 2005, ISSN: 0022-460X. DOI: 10.1016/J.JSV.2004.01.006.